AFOSR-TR-97

0552

REPORT DOCUMENTATION PAGE

1. AGENCY USE ONLY (Leave blank)	2. REPORT DATE	3. REPORT TYPE AND DATES COVERED
	29-September 1997	Final Tech. Rpt:1 Aug 94 to 31 July 1997

4. TITLE AND SUBTITLE
(U) Mechanisms Controlling Soot Formation in Diffusion Flames

5. FUNDING NUMBERS
PE - 61102F
PR - 2308
SA - BS
C - F49620-94-C-0059

6. AUTHOR(S)
Meredith B. Colket, III; Robert J. Hall; Mitchell D. Smooke

7. PERFORMING ORGANIZATION NAME(S) AND ADDRESS(ES)
United Technologies Research Center
411 Silver Lane
East Hartford, CT 06108

8. PERFORMING ORGANIZATION REPORT NUMBER

9. SPONSORING / MONITORING AGENCY NAME(S) AND ADDRESS(ES)
AFOSR/NA
110 Duncan Avenue, Suite B115
Bolling AFB DC 20332-0001

10. SPONSORING / MONITORING AGENCY REPORT NUMBER

19971103 058

11. SUPPLEMENTARY NOTES

12a. DISTRIBUTION / AVAILABILITY STATEMENT
Approved for public release; distribution is unlimited

12b. DISTRIBUTION CODE

13. ABSTRACT (Maximum 200 words)

Arclength continuation methods were incorporated into a code for predicting the structure of sooting, opposed-jet flames. The code includes complex chemistry, detailed particle dynamics, particle chemistry and radiation. The code was used to predict soot production over a wide variation in strain rates for both ethylene/air and methane/air diffusion flames. Predicted values (both peak and spatial distributions) agree well with experimental measurements in ethylene flames. Particle size distributions are also predicted using the aerosol equations from MAEROS, but no data is available for comparison. Also, the soot dynamical equations were imbedded into a separate code to describe soot production in a coflow, laminar, diffusion flame which includes treatment of detailed, gas phase chemistry. Predictions were compared to measurements made in a methane, coflow flame. Reasonable agreement between the predictions and measurements was obtained, although a factor of three underprediction of the soot volume fractions is likely due to uncertainties in inlet conditions and an inability to match closely bulk flame parameters such as temperature. Predicted peak soot production occurred around 1720K and particle oxidation was dominated by superequilibrium concentrations of hydroxyl radicals. Several PAH-forming sequences were examined and compared to the traditional acetylene-addition sequence. A sequence involving benzyl-propargyl combination was found to compete with the traditional mechanism and it should be included in future analyses. The algorithms for treating sectional soot dynamics and growth/oxidation rates were modified to include effects at high pressure. Continuum effects and limitations to gaseous diffusion were included in the opposed jet code. Predicted variations in soot production due to pressure changes from 4 to 10 atmospheres were made for an ethylene-air, opposed jet flame.

14. SUBJECT TERMS	15. NUMBER OF PAGES
Opposed jet flames, coflow flames, laminar diffusion flames, formation of polyaromatics, toluene, benzyl and propargyl radicals, soot formation modeling, high pressure effects on particle dynamics, soot oxidation, hydroxyl radicals, particle size	94
	16. PRICE CODE

17. SECURITY CLASSIFICATION OF REPORT	18. SECURITY CLASSIFICATION OF THIS PAGE	19. SECURITY CLASSIFICATION OF ABSTRACT	20. LIMITATION OF ABSTRACT
Unclassified	Unclassified	Unclassified	UL

MECHANISMS CONTROLLING SOOT FORMATION IN DIFFUSION FLAMES

Final Technical Report
August 1, 1994 to July 31, 1997

AFOSR Contract F49620-94-C-0059

Principal Investigators:
Meredith B. Colket and Robert J. Hall

United Technologies Research Center
Silver Lane, E. Hartford, CT 06108

Prepared with assistance from
M. D. Smooke
Yale University

UTRC Report No. UTRC97-5.906.0001-1

J. M. Tishkoff
Program Manager
September 29, 1997

MECHANISMS CONTROLLING SOOT FORMATION IN DIFFUSION FLAMES

Final Technical Report

Table of Contents

MECHANISMS CONTROLLING SOOT FORMATION IN DIFFUSION FLAMES

Final Technical Report
August 1, 1994 to July 31, 1997

AFOSR Contract F49620-94-C-0059

I. Objectives

The overall objectives of this work are to (1) refine and update a pyrolytic model which describes PAH formation; (2) modify and validate an opposed jet diffusion flame code which includes soot formation and radiation and then extend model predictions over a range of flame parameters, and (3) incorporate the soot formation and radiation models into a code for a coflow laminar, diffusion flame. These efforts, particularly the latter two, are being completed with assistance from Prof. M. Smooke of Yale University. Experiments and modeling on alkylated aromatics will help to minimize discrepancies between known PAH formation rates and those required to explain particle inception rates in flames. Validation (and modification as necessary) of the existing opposed jet flame code with data from ethylene flames will increase its reliability in predicting sooting conditions with other hydrocarbon fuels and inlet conditions. In addition, this effort should demonstrate the code's utility prior to installing soot formation and radiation routines into codes describing other flame geometries for which extensive data bases exist.

II. Status of Effort

The objectives outlined in the above paragraph have been met during the course of this three year program. Much of the work is now documented in publications or recently submitted manuscripts; including (1) Predictions of Soot Dynamics in Opposed Jet Diffusion Flames [1], (2) Application of Continuation Methods to Soot Formation in Counterflow Diffusion Flames [2], (see Appendix A), (3) Computational and Experimental Study of Soot Formation in a Coflow, Laminar Diffusion Flame [3], (see Appendix B) and by several presentations at technical meetings, (for the most recent presentations see the section on meeting interactions).

Most of the research described in [1] was a result of work completed in an earlier contract and hence will not be treated here. The results from [2], [3] and a recent abstract [4] are the main accomplishments of this contract. A brief summary of conclusions from these studies are provided in Sections III. A. and B., while the details are presented in the Appendixes of this report. In addition, description of some very recent work on PAH/inception modeling and the development of algorithms for the treatment of sectional

soot dynamics at high pressure, not yet documented elsewhere, is provided in Sections III. C. and D.

III. Accomplishments/New Findings

III. A. Continuation Model for Sooting, Opposed Jet Flame

Detailed flame models that include complex chemistry coupled with soot formation, growth, oxidation, and particle dynamics equations with radiation effects have been developed for both laminar premixed, burner-stabilized flames and opposed jet flames. These models have been based upon AFOSR sponsored work described previously [1,5]. The opposed jet flame model has been extended by incorporating an arclength continuation method into the code such that flame solutions can be readily obtained over a wide range of strain rates. This recently documented procedure [2] dramatically decreases the effort required to obtain solutions over a range of conditions. Solutions were obtained from low strain to extinction for both ethylene and methane flames. Peak soot volume fractions were found to decrease gradually (logarithmic scale) from low to high strain by about two orders of magnitude for the ethylene flames. The decay was principally attributed to the decrease in residence time in the high strain flames, although decreasing benzene concentrations and flame temperatures contribute to the decrease. The concentration of acetylene, the principal species contributing to surface growth, did not vary by more than a factor of two. Predicted soot volume fractions agreed well with experimental measurements of peak values and the spatial dependence of soot volume fractions for the ethylene flames. There is yet no data available to compare the predictions of particulate size and how the distribution varies with location in the opposed jet flame.

III. B. Soot Formation in a Coflow, Laminar, Diffusion Flame

In a second study [3], the soot dynamical equations have been coupled with the equations describing an axisymmetric, coflow, laminar diffusion flame. Predictions have been made for a methane jet flame and have been compared to recent experimental measurements. Effects of thermal radiation and particle scrubbing of the gas phase species (for inception, growth, and oxidation) are included. General features of the flame are reasonably well described, although peak soot volume fractions are underpredicted by about a factor of three. We believe this underprediction is principally due to the inability to predict accurately the bulk flame properties, such as low predictions of centerline temperatures and a slight overprediction of the flame height. Possible sources of these uncertainties include radiative heat transfer to the unreacted fuel, burner lip effects, and perhaps insufficient, low temperature, fuel rich chemical kinetics for the methane fuel. (As described in Section III.C., there may also be uncertainties in the calculated inception rates.) Predicted distributions of particle sizes indicate the existence of relatively small particles along the centerline of the burner and small concentrations of large particles which escape the flame front, unoxidized. Oxidation of particulates is dominated by hydroxyl radicals which attain concentrations about ten times above equilibrium near the flame front. Gas cooling effects, due to radiative losses, are shown to have a very significant effect (factor of three decrease) on predicted soot volume fractions, for this lightly sooting, methane flame.

The solution file for this coflow, methane flame has been recently interrogated [4] (see Appendix C) to extract information about the soot formation process in the flame. Peak surface growth rates were found to be on the rich side of the flame front at temperatures of 1720-1760K, which is in the vicinity of the peak of the traditional bell-shaped curve for soot formation. Local equivalence ratios under these conditions are about 1.8, tending towards less rich conditions higher in the flame.

III. C. PAH Formation and Modeling

Previously, we have argued that existing detailed inception models imbedded in soot formation codes generally underpredict the formation rates of PAH molecules in flame. Hence it is likely that predicted inception rates, based upon traditional routes for PAH production, are low. While there are some arguments to the contrary [6], we have yet to adopt the higher reaction rates assumed in the alternate analysis. Instead, we believe that there are mechanisms contributing to PAH production in addition to the alternate acetylene addition steps (and occasional benzene/phenyl addition) and cyclization processes. Based on the recent work on the toluene pyrolysis mechanism, with and without additives [7,8], we have just considered relative inception rates based on the reaction set shown in Table I.

Table I. Alternate Mechanism for PAH Production via Toluene/Benzyl

							log (A_{for})	$E_{forward}$	log (A_{rev})	$E_{reverse}$
C_6H_5	+	CH_3	⇔	C_7H_8			12.92	-800	16.0	97000
C_6H_6	+	CH_3	⇔	C_7H_8	+	H	12.3	17000	13.08	5100
C_7H_8	+	H	⇔	C_7H_7	+	H_2	14.1	8400	13.5	23700
C_7H_8	+	CH_3	⇔	C_7H_7	+	CH_4	12.2	11100	13.08	27000
		C_7H_8	⇔	C_7H_7	+	H	15.45	88900	14.24	-200
C_7H_7	+	C_3H_3	⇒	$C_{10}H_8$	+	2H	11.7	5000		
C_7H_7	+	C_7H_7	⇔	$C_{14}H_{14}$			12.7	-500	14.93	60000
$C_{14}H_{14}$	+	H	⇒	$C_{14}H_{10}$	+	$2H_2$	13.7	5000		
					+	H				

* A - cc, moles, sec units; E - calories/mole

Forward and reverse rate constants in this table are taken from the previous analysis on toluene pyrolysis [7,9] but with an updated rate constant [8] for the propargyl-benzyl recombination reaction that forms naphthalene ($C_{10}H_8$).

An analysis based on the steady-state assumptions for toluene, bibenzyl and the benzyl radical was performed to estimate a rate of production of naphthalene from this reaction sequence. The rates of production of naphthalene via this mechanism were compared to the rates of production of $C_{10}H_7$ via the more traditional acetylene addition mechanism. Using the local solutions of species concentrations and temperature from the coflow,

methane flame, the rates from this 'new' mechanism were found to be at least comparable to those for the traditional route in the flame front and generally nearly an order of magnitude higher near the centerline of the flame. These results qualitatively support the experimental result obtained by [10] that addition of small concentrations of toluene in the fuel increases the production of naphthalene in the coflow, methane flames.

In addition, we have examined the potential for recombination/rearrangement of cyclopentadienyl radicals as a source of naphthalene in these flames. The kinetic calculations indicate that this route should dominate the naphthalene production; however, we do not yet endorse this route as the experimental evidence for this process is less clear and it is likely that we have significantly overestimated this net rate due to the lack of including scrubbing effects and the skeletal mechanism utilized for C_5-chemistry.

Nevertheless, these results strongly support the necessity of including alternate PAH formation routes in the modeling of inception processes. Such sequences have not yet been included in our flame modeling but are anticipated to be installed shortly. The role of these alternate mechanisms must be considered more completely in subsequent modeling of soot formation in flames.

III. D. Treatment of Sectional Soot Dynamics at High Pressure

The sectional soot growth program has been modified to be valid for high-pressure calculations. The first versions had been written for the low-pressure, free-molecule regime in which mean free path is larger than characteristic particle sizes (pressures up to approximately 1-2 atmospheres). Coalescence rates in the free-molecule regime are equal to sticking probabilities times hard-sphere collision frequencies, surface growth and oxidation growth coefficients have a simple, semi-analytic form, and thermophoretic velocity is independent of particle size [1]. As pressure increases, this assumption of mean free path larger than particle sizes becomes invalid, first for the largest particles, and the so-called continuum regime is entered. The intermediate situation between the strict free-molecule and continuum cases is called the transition regime. Corrections to the rates of coalescence, surface growth and oxidation, and thermophoresis are then required.

The sectional coalescence coefficients were modified for continuum effects using algorithms already contained in the MAEROS program [11] from which the soot program originated. The contributions of Brownian motion to the coalescence rates in the transition and continuum regime are treated in the manner of Fuchs [12]. Gravitational and turbulence contributions were not included. As continuum effects become important, the thermophoretic velocities of the largest particles start to decrease, so that in general a variation of velocity with size class must be considered. At very high pressure, thermophoretic velocity again becomes independent of size class. The transition and continuum corrections were again calculated using algorithms embedded in the MAEROS program, which were in turn based on the treatment of Waldmann and Schmitt [13].

Continuum effects corrections for surface growth and oxidation are more complicated. The net rate of growth or oxidation at a particle surface has contributions both from diffusion of gaseous reactants to the surface, and the intrinsic chemical process at the surface. Measured rates are true surface reaction rates only if they are small relative to the rate for diffusion of reactants to the surface. In the free-molecule limit, the reactant flux at the surface is given by gas kinetic impingement rates, and reactant concentrations at the surface are substantially equal to the asymptotic values far from the surface. As the pressure increases to the continuum limit, diffusion theory is used to calculate the reactant flux [14]. The transition regime diffusional reactant flux is calculated using an approximate interpolation formula proposed by Fuchs and Sutugin [14,15]. With the diffusional flux at the particle surface established, the assumption of steady state at the surface leads to resistance rule expressions for the net rate of carbon atom addition due to growth, and carbon atom removal due to oxidation by oxygen and OH. This expression has the proper limiting forms. In the limit that the diffusional flux is much larger than the intrinsic surface processes, the total per particle growth/oxidation rates will always be proportional to particle surface area, or the mass of the particle raised to the two-thirds power. When the intrinsic rates dominate in the free-molecule regime, the proportionality to surface area will again apply. When the intrinsic rates dominate in the continuum limit, the total per particle rate will be proportional to particle diameter, or to the square root of particle surface area. In the high-pressure soot program, the generalized rate expression is employed in the numerical integration over the assumed, intra-sectional mass distribution function which is used to calculate the sectional coefficients [1,11]. This is done individually for the acetylene addition growth process, oxidation by oxygen, and oxidation by OH. One assumption of the present program is that for simplicity the algorithm has been set up assuming intrinsic rates first order in the applicable reactant (acetylene, oxygen, OH). Particle diffusional transport makes such a small contribution in most simulations that for simplicity the particle diffusional coefficients have been set equal to zero in the high pressure program. The program calculates all coefficients at a given pressure for a range of temperatures, and then uses interpolation to extract coefficients at intermediate temperatures.

Figure 1 shows an example calculation for a plug flow, ethylene-air opposed jet at a strain rate of 80 sec^{-1}. The sensitivity to pressure is highest at the lowest pressures, becoming less sensitive at higher pressures as the importance of particle scrubbing of gaseous growth species becomes important. The ability to account for continuum effects on the particle growth and transport coefficients may now be on a sounder basis in this code than is the ability to model pressure effects on the gas phase chemistry.

Figure 1. Predicted Sensitivity of Soot Volume Fraction to Pressure in Ethylene-Air Opposed Jet Flame

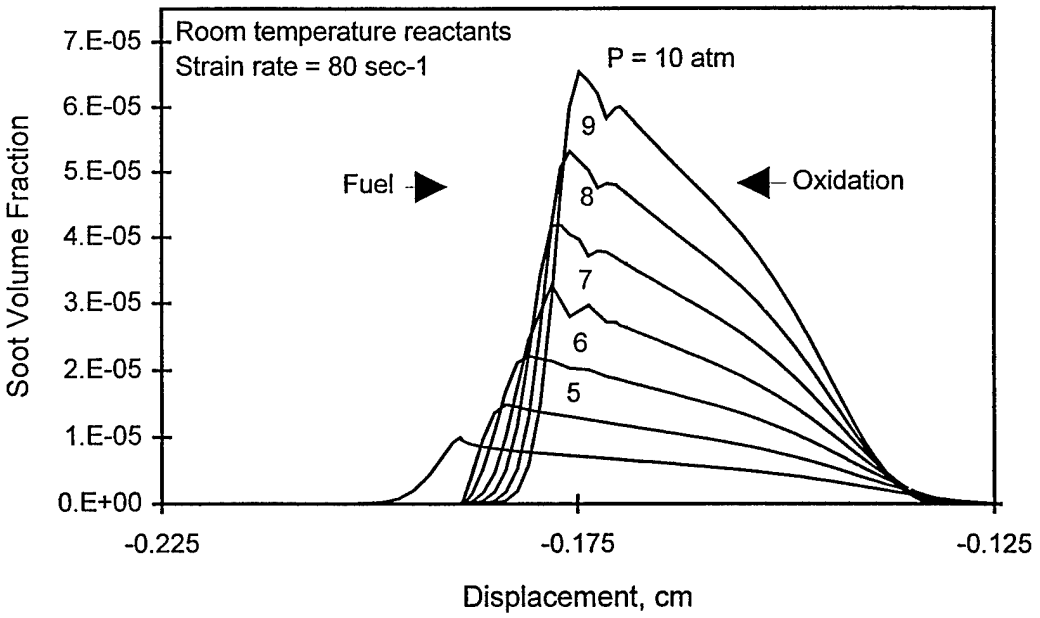

III. E. References

1. R.J. Hall, M.D. Smooke, and M.B. Colket, in Physical and Chemical Aspects of Combustion: A Tribute to Irvin Glassman, Ed. by R.F. Sawyer and F.L. Dryer, Combustion Science and Technology Book Series, Chapter 8, Gordon and Breach, (1997).
2. M. D. Smooke, R. J. Hall, and M. B. Colket, "Application of Continuation Methods to Soot Formation in Diffusion Flames," Submitted for publication to Combustion Theory and Modeling. (1996). (See Appendix A.)
3. M. D. Smooke, C. S. McEnally, L. D. Pfefferle, R. J. Hall, and M. B. Colket, "Computational and Experimental Study of Soot Formation in a Coflow, Laminar Diffusion Flame," Submitted for publication to Combustion and Flame. (1997) (see Appendix B.)
4. M. D. Smooke, R. J. Hall, and M. B. Colket, "Interpretations from a Computational Study of Soot Formation in a Coflow, Laminar Diffusion Flame" to be presented at the 1997 Fall Technical Meeting of the Eastern States Section of the Combustion Institute in Hartford Connecticut. (see Appendix C.)
5. M. Colket and R. Hall, Proceedings of the International Workshop on Mechanism and Models of Soot Formation (H. Bockhorn, Ed.), Springer-Verlag, Heidelberg, (1994).
6. P. Markatou, H. Wang, and M. Frenklach, Combustion and Flame **93**, pp. 467-482 (1993) and references contained therein.
7. M. Colket and D. Seery, Twenty-Fifth Symposium (International) on Combustion, The Combustion Institute, Pittsburgh, p. 883 (1995).
8. M. Colket, "Rapid Naphthalene Production from Allene and Toluene," presentation to the Eastern States Section of the Combustion Institute, Oct. 16-18, 1995.

9. M. Colket, R. Hall, and M. Smooke, "Mechanistic Models of Soot Formation," UTRC Report UTRC94-28, Final Technical Report for AFOSR Contract F49620-91-C-0056, (1994).
10. C. McEnally and L. Pfefferle, "Experimental Assessment of Naphthalene Formation Mechanisms in Non-Premixed Flames", submitted to Combustion Science and Technology, 1997.
11. F. Gelbard and J.H. Seinfeld, J. Coll. Int. Sci., **78**, p. 485 (1980); F. Gelbard, MAEROS Users Manual, NUREG/CR-1391, (SANDD80-0822), (1982).
12. N.A. Fuchs, Mechanics of Aerosols, Pergamon, pp. 291-294 (1964).
13. L. Waldmann and K.H. Schmitt, in Aerosol Science, ed. By C.N. Davies, Chapter 6, Academic Press, (1966).
14. S.K. Friedlander, Smoke, Dust and Haze, Wiley & Sons, pp. 246-247 (1977).
15. N.A. Fuchs and A.G. Sutugin, in Topics in Current Aerosol Research, ed. by G.M. Hidy and J.R. Brock, Pergamon, (1971).

IV. Personnel Supported

Key personnel contributing to this project are:
Dr. Meredith B. Colket, III of United Technologies Research Center
Mr. Robert J. Hall of United Technologies Research Center
Prof. Mitchell D. Smooke of Yale University

V. Publications

R. J. Hall, M. D. Smooke, and M. B. Colket, "Predictions of Soot Dynamics in Opposed Jet Diffusion Flames", in Physical and Chemical Aspects of Combustion, A Tribute to Irvin Glassman, ed. by F. L. Dryer and R. F. Sawyer, Combustion Science and Technology Book Series, Vol. 4, Gordon and Breach Science Publishers, (1997).

M. D. Smooke, R. J. Hall, and M. B. Colket, "Application of Continuation Methods to Soot Formation in Diffusion Flames," Manuscript submitted for publication to Combustion Theory and Modeling. (1996). (See Appendix A.)

M. D. Smooke, C. S. McEnally, L. D. Pfefferle, R. J. Hall, and M. B. Colket, "Computational and Experimental Study of Soot Formation in a Coflow, Laminar Diffusion Flame," Manuscript submitted for publication to Combustion and Flame. (1997) (see Appendix B.)

VI. Interactions/Transitions

VI. A. Meetings

On December 9-11, 1996, M. Colket and M. D. Smooke attended the Fall Technical Meeting of the Eastern States Section of the Combustion Institute at Hilton Head, South Carolina. Papers entitled "Computational and Experimental Study of a Sooting, Coflow, Laminar Diffusion Flame" and "Application of Continuation Methods to Soot Formation in Diffusion Flames" were presented.

On January 6-10, 1997, M. Colket attended the 35th Aerospace Sciences Meeting at Reno, NV.

On March 5-7, 1997, M. Colket attended the "Advanced Gas Turbine System Research" Combustion Technology Workshop in Atlanta, Georgia.

On May 27-28, 1997, M. Colket attended the 19th Annual Combustion Research Conference of the US. DOE, Basic Energy Sciences in Chantilly, Virginia.

On October 27-29, 1997, "Interpretations from a Computational Study of Soot Formation in a Coflow, Laminar Diffusion Flame" will be presented at the 1997 Fall Technical Meeting of the Eastern States Section of the Combustion Institute in Hartford Connecticut.

VI. B. Advisory Functions

None

VI. C. Transitions

In the fall of 1996, M. Colket and R. Hall transferred software (validated under this program) that describes soot formation, growth, and oxidation and particle (aerosol) dynamics to M. Colket (of United Technologies Research Center in support of Pratt and Whitney's modeling efforts) for imbedding into a network PSR code.

VII. Record of Inventions

There were no inventions during this reporting period. (DD Form 882, Interim Patent Report submitted under separate cover, September 26, 1997)

VIII. Honors/Awards

M. Colket received a 1996 UTRC Outstanding Achievement Award as a member of a team effort that provided outstanding customer support to Pratt and Whitney in the development of a robust, ultra-low NOx, FT8 combustor.

Appendix A
Application of Continuation Methods to Soot Formation in Counterflow Diffusion Flames

APPLICATION OF CONTINUATION METHODS TO SOOT FORMATION IN COUNTERFLOW DIFFUSION FLAMES

M. D. Smooke[1], R. J. Hall[2], and M. B. Colket[2]

[1] *Department of Mechanical Engineering, Yale University, New Haven, CT 06520-8284, USA.*

[2] *United Technologies Research Center, East Hartford, CT 06108, USA.*

Abstract

An arclength continuation method has been incorporated into a coupled gas/particle opposed jet soot prediction code and used to examine the soot production in methane-air and ethylene-air diffusion flames. The model includes a detailed transport, finite rate chemistry gas phase system coupled with aerosol dynamical equations in the sectional representation. The problem formulation includes detailed submodels for the inception, growth, oxidation, and dynamics of soot particulates. The continuation feature produces a dramatic reduction in the effort required to carry out extensive studies of the sensitivity of soot growth to flame parameters such as the strain rate. Computations for both atmospheric pressure methane-air and ethylene-air counterflow diffusion flames are presented. Effects of radiation and variation in important soot growth species are examined. Full coupling of radiation and scrubbing within the flame and soot equations is demonstrated to be dramatically important, especially at low strain rates. Residence time at elevated temperature was found to be a dominant parameter controlling soot production.

APPLICATION OF CONTINUATION METHODS TO SOOT FORMATION IN COUNTERFLOW DIFFUSION FLAMES

Introduction

Numerical models for analyzing the structure of opposed jet diffusion flames (See Figure 1) with detailed chemistry have been refined over the past ten years [1-5]. Current modeling capabilities for opposed-jet, non-sooting flames are now excellent, with most uncertainties centered on inlet conditions and on the chemical kinetic sets used to model the data. Comparisons between experimental and computational results have been made with the goal of helping to interpret flame structure, extinction limits and soot formation phenomena. In particular, there have been studies on soot inception limits in air [6-7], effects of oxygen in the fuel [8], effects due to strain rate variations [9], and on the relative importance of temperature and fuel dilution on soot formation processes [10]. Typically, only skeletal models integrating the soot formation processes with opposed-jet flame computations have been available to assist in the interpretation of the experimental data. Recently, a comprehensive particle kinetics model was constructed [11] which provided qualitative predictions comparable to existing data for soot formation in an opposed-jet, methane-air diffusion flame [12]. Particle sectional equations with submodels for particle inception, growth, coagulation, and oxidation [13] were coupled to the gas phase conservation equations for an opposed-jet diffusion flame. Complex chemistry and detailed transport along with particulate and gas radiation were included. The model has the capability to provide detailed spatially-dependent information on volume fractions, particle number density, size and size distribution. Codes of this type can be used to validate, over required ranges of temperatures, pressures and fuel types, various proposed (semi-empirical) mechanisms for modeling soot formation and to help determine simplifying assumptions which can be made in fluid-dynamically more complex models. The model developed in [11] has been exercised recently in an attempt to compare several soot formation mechanisms proposed and to re-evaluate some of the temperature and dilution effects described in the literature [14].

Solutions of strained, nonpremixed laminar flames have been used in the modeling of turbulent reacting flows in the laminar flamelet regime [15]. Such applications require solutions over a large range of strain rates, which generate the functional relationships between soot volume fraction and mixture fraction/scalar dissipation. Manual generation of these solutions is highly labor intensive. To resolve this problem, the model derived in [11] has been modified to include continuation. By incorporating arclength continuation concepts [16,17], one can now perform accurate, highly resolved, detailed parameter studies in which the strain rate, pressure, inlet temperatures, dilution factor and (for premixed cases) the equivalence ratio are varied. The model and solution algorithm are described in this manuscript. Predictions for soot volume fractions as a function of strain rate have

been made and reported herein for both ethylene-air and methane-air diffusion flames at atmospheric pressure with the reactants at room temperature. Effects of radiation are examined and soot particle dynamics are analyzed.

Soot Modeling

The soot kinetics continuation analysis is based on a single solution opposed jet particle growth program that employs the sectional representation for spheroid growth [11]. The picture of soot kinetics is that of coalescing, solid carbon spheroids undergoing surface growth in the free molecule limit. The particle mass range of interest is divided into sections [18], and a dynamical equation written for each section including coalescence, surface growth, and oxidation. For the first bin, an inception source term is included. The incorporation of these dynamical equations into a transport/conservation equation for each section includes both thermophoresis and an effective bin diffusion rate. In the gas species conservation equations, provision is made for complex chemistry; additional source terms are included to account for scrubbing or generation of gaseous species arising from the particle growth and oxidation processes. The gas and soot are additionally coupled through non-adiabatic radiative loss from both the gas and the soot in the optically thin approximation. For one atmosphere calculations, the sectional coefficients for transport, coalescence, and surface processes are calculated in the free molecule limit [18], with surface growth and oxidation proportional to particle surface area. In the free molecule limit, the particle mass and medium dependencies of the sectional coefficients are factored in such a way that they only have to be evaluated once. Oxidation of soot by O_2 and OH is treated as described in [11]. The inception model employed here is based on an estimate of the formation rate of two-and three-ringed aromatic species, and is a function of local acetylene, benzene, phenyl, and molecular hydrogen concentrations. Assuming steady-state values of intermediates and that $H_2 >> C_2H_2$, the rate of production of the polyaromatic species can be estimated to be [11]

$$\frac{d[\dot{C_{10}H_7}]}{dt} = 10^{11.88} e^{(-4378/T)} \frac{[C_2H_2]^2}{[H_2]} [\dot{C_6H_5}] \text{ cc/mole/sec}, \tag{1}$$

and

$$\frac{d[C_{14}H_{10}]}{dt} = 10^{12.50} e^{(-6390/T)} \frac{[C_2H_2]}{[H_2]} [C_6H_6][\dot{C_6H_5}] \text{ cc/mole/sec}, \tag{2}$$

where the gas phase concentrations and temperatures are evaluated at local conditions. With the further assumptions that inception is limited by the formation of polyaromatics and oxidation/decomposition of such species can be neglected, the inception rate, S_i, in grams/cc/sec was initially assigned to

$$S_i = 127 \times \frac{d[C_{10}H_7]}{dt} + 178 \times \frac{d[C_{14}H_{10}]}{dt}, \tag{3}$$

where the constants (molecular weights) are provided to convert from molar to mass units. This inception rate is included as a source term in the dynamical equations for the first size class, whose lower mass boundary is set at 127 amu. The upper mass boundary of the highest class is set sufficiently large to ensure that the solution is independent of this maximum mass; for these calculations the maximum value is approximately 10^{12} amu. There is no significant density of particles in the highest classes.

The surface growth rate is nominally that of Harris and Weiner [19], who report, from premixed flame investigations, a rate proportional to acetylene concentration; their rate is normalized in this application to 1650K, with a 31.8 kcal activation energy as suggested by Hura and Glassman [8]. However, there is evidence from ethylene diffusion flames that the effective surface growth rate is somewhat larger than that reported by Harris and Weiner, who used optical techniques and the assumption of isolated soot spheroids (Axelbaum, Flower, and Law [20]; Kennedy, Kollmann, and Chen [21]; Sunderland and Faeth [22]). Puri, Richardson, Santoro, and Dobbins [23] have suggested that the assumption of spherical particle shapes in analysis of light scattering data can lead to error, and that a more appropriate interpretation of the data in terms of an aggregate particle morphology can be made, leading to different total soot surface areas and specific growth rates. As will be seen, it has been found on an empirical basis that it is necessary to enhance the HW growth rate by about a factor of two.

The main soot parameter of interest in this paper is the soot volume fraction, for which convergence is generally obtained with a smaller number of sections than is the case for particle size and number density [11]. The number of sections required for convergence must be examined in each case, although evidence points to the relative magnitudes of surface growth and inception as the important parameter. When the contribution of inception to total volume fraction is significant, although not necessarily dominating, the number of sections required can be very small [11], with larger numbers necessary when the contribution of surface growth to volume fraction becomes very much larger than that from inception. A total of twenty soot classes were used in the calculations reported in this paper. This level insured that predicted soot volume fractions were essentially independent of the number of sections.

The chemical mechanism used for modeling the methane flames is a modified version of GRIMech 2.11 [24] with 1) the pressure-dependent reactions evaluated at atmospheric pressure, 2) the NOx chemistry removed and 3) the addition of the formation and oxidation steps of benzene and related species [11]. It contains 38 species and 192 individual reaction steps. The ethylene species mechanism employed has 45 species and 233 reactions. This

set, derived from GRIMech 1.2, has been developed at UTRC based upon comparisons to experimental data from perfectly stirred and flow reactors as well as ignition delay measurements.

As an example of how the model predictions agree with experimental data, the single solution code has been used to simulate the ethylene opposed jet experiments of Wang *et al.* [25]. Although the experiment is nominally described by plug flow, Wang, et. al. report that the real flow is a mixture of plug and potential solutions, and describe a process by which they adjust boundary conditions to match their experimental velocity profiles in the flame region using a potential flow simulation. The simulations described here employed a different procedure. Plug flow is assumed, but the velocity on the fuel side is adjusted to bring the theoretical velocity profile into agreement with experiments. The oxidizer velocity is assigned the value determined from the stated oxidizer flow rate. Figure 2 shows that this procedure gives excellent agreement with data for the highest and lowest strain rates reported by Wang, et. al.. With such fits, it can be assumed that the particle residence times, important for soot growth simulations, are accurate representations of the experiments. The velocity gradient shown is the difference of the fuel and oxidizer velocities divided by the distance between the fuel and oxidizer jets required to fit the velocity data. Figure 3 shows the comparisons of predicted and measured soot volume fractions for an assumed factor of two enhancement of the HW surface growth rate. Deviations from the experimental results are well within experimental uncertainty.

The surface growth/inception models used here to illustrate the soot continuation analysis agree well with available ethylene opposed jet data. Nevertheless, it is not suggested that it represents a universal solution to the problem of soot formation because comparisons with soot data in other fuels have not been carried out. The possibility of aging of the surface growth rate has not been accounted for here, nor are the results with finite coalescence appropriate for aggregate formation. Fundamental questions relating to inception, temperature dependence of surface growth, and precise dependence of surface growth on gas phase species concentrations remain. The need to consider gaseous PAH as major surface growth species in addition to acetylene has also been suggested by Benish, Lafleur, Taghizadeh and Howard [26]. To some extent, such processes are included in the formulation of our model, since PAHs are implicitly treated as soot particles and hence are included in the coalescence and surface growth equations. Whether soot growth rates derived from premixed and opposed jet studies are self-consistent is still an open issue, as well.

Problem Formulation

Conservation Equations

To model the combined gas phase/soot-laden counterflow diffusion flame (Figure 1),

we utilize the elliptic form of the two-dimensional conservation equations in cylindrical coordinates for the gas phase together with corresponding sectional species equations (assuming no slip between the gas and particle phases). The complexity of the coupled system can be reduced [27] by seeking a similarity solution of the form $u = rU(z)$, $v = v(z)$, $Y_k = Y_k(z)$, $k = 1, 2, \ldots K, K+1, \ldots, K+M$, $T = T(z)$, where r and z denote the independent radial and axial spatial coordinates, respectively; T, the temperature; K, the total number of gas phase species and M, the number of soot (size) sections; Y_k, the mass fraction of the k^{th} gas phase species ($k \leq K$) or the $(k-K)^{th}$ soot size class ($k > K$) and u and v the radial and axial components of the velocity, respectively. If we substitute the expressions for the two velocities into the continuity and the momentum equations, we find that the reduced pressure gradient in the radial direction is constant, i.e., $1/r \cdot \partial P/\partial r = J$, where P denotes the pressure. If we use this result, together with the similarity assumptions, we find that the combined gas and particle two-dimensional set of governing equations can be reduced to a nonlinear two-point boundary value problem in the axial direction. The governing equations for mass, momentum, chemical species, soot size classes and energy can be written in the form

$$\frac{dV}{dz} + 2\rho U = 0, \tag{4}$$

$$\frac{d}{dz}\left(\mu \frac{dU}{dz}\right) - V\frac{dU}{dz} - \rho U^2 - J = 0, \tag{5}$$

$$-\frac{d}{dz}(\rho Y_k V_{kz}) - V\frac{dY_k}{dz} + (\dot{w}_k^g + \dot{w}_k^s)W_k = 0, \quad k = 1, 2, \ldots, K, \tag{6}$$

$$-\frac{d}{dz}(\rho Y_k (v_T + v_{D_k})) - V\frac{dY_k}{dz} + \dot{Q}_k = 0, \quad k = K+1, K+2, \ldots, K+M, \tag{7}$$

$$\frac{d}{dz}\left(\lambda \frac{dT}{dz}\right) - c_p V\frac{dT}{dz} - \sum_{k=1}^{K} \rho Y_k V_{k_z} c_{pk}\frac{dT}{dz} - \sum_{k=1}^{M} \rho Y_k (v_T + v_{D_k}) c_{pk}\frac{dT}{dz}$$
$$- \sum_{k=1}^{K+M} (\dot{w}_k^g + \dot{w}_k^s)W_k h_k + \frac{dq_r}{dz} = 0, \tag{8}$$

and

$$\rho = \frac{P\overline{W}}{R_g T}, \tag{9}$$

where $V = \rho v$, and, in addition to the variables already defined, ρ denotes the mass density; W_k, the molecular weight of the k^{th} species; $\overline{W}$, the mean molecular weight of the mixture; R_g, the universal gas constant; λ, the thermal conductivity of the mixture; c_p, the constant pressure heat capacity of the mixture; c_{pk}, the constant pressure heat capacity of the k^{th} species; $\dot{w}_k^g$, the molar rate of production of the k^{th} species per unit volume due to gas phase chemistry, $\dot{w}_k^s$, the molar rate of production of the k^{th} species per unit volume due to scrubbing/replenishment by the soot growth/oxidation processes; $\dot{Q}_k$ the rate of change

of section k due to aerosol processes; h_k, the specific enthalpy of the k^{th} species; μ the viscosity of the mixture; V_{kz}, the diffusion velocity of the k^{th} species in the z direction; v_T and v_{D_k} the thermal and mass diffusion velocities of the k^{th} soot size class and dq_r/dz the divergence of the net radiative flux for gas bands and soot in the optically thin limit. To complete the specification of the problem, boundary conditions must be imposed on both the fuel and oxidizer jets. (For more details the reader is referred to [11]).

It is worthwhile to note that in the above formulation the strain rate does not appear explicitly in the governing equations. The magnitude of the reduced pressure gradient, J, is related to the "stretch" in the flame due to the imposed flow. As the magnitude of J increases, so does the strain rate. The strain rate can be computed from the axial velocity gradient. However, since this quantity varies throughout the flame, one must decide on a specific location (for example, the maximum value of the axial velocity gradient on the oxidizer or the fuel side have been used) for its evaluation. Alternatively, one could employ the asymptotic formula derived in [28]. In this paper we utilize an "average" strain rate given by

$$a = \frac{|v_f| + |v_{ox}|}{L}, \tag{10}$$

where v_f and v_{ox} are the fuel and oxidizer velocities, respectively, and L is the length of the computational domain. We point out that for ethylene-air diffusion flames, the expression in (10) is essentially equal to one half the value defined in [28]. A major advantage in using (10) is that it can easily be obtained from experimental flow rates and does not require velocity measurements inside the domain.

Method of Solution

Our goal is to be able to study the variation of soot volume fraction as a function of the strain rate. As the strain rate varies from low to high values, the flame nears extinction. During this process the flame can adjust its position in the computational domain. As the extinction point is reached, the Jacobian matrix becomes singular. This precludes the use of conventional solution algorithms. As a result, to be able to move smoothly from low through extinction values of the strain rate, we employ an arclength continuation solution algorithm with Newton-like iterations and global adaptive gridding [17]. The set of equations (4-9) reduces to a system of the form

$$\mathcal{F}(\mathcal{X}, J) = 0, \tag{11}$$

where $\mathcal{X} = (V, U, Y_1, \ldots, Y_{K+M}, T)$ is the solution vector. The solutions $(\mathcal{X}, J)$ in (11) form a one-dimensional manifold which, as a result of the presence of turning points, cannot be parameterized in the form $(\mathcal{X}(J), J)$. The upper part of the manifold denotes the stable solutions and the lower part the unstable ones, assuming there are no Hopf bifurcations.

To generate this solution set, $(\mathcal{X}, J)$ is reparameterized into $(\mathcal{X}(s), J(s))$ where s is a new independent parameter and J becomes an eigenvalue. The system in (11) can now be

written

$$\mathcal{F}(\mathcal{X}(s), J(s)) = 0, \tag{12}$$

and the dependence of s on the augmented solution vector $(\mathcal{X}, J)$ is specified by an extra scalar equation

$$\mathcal{N}(\mathcal{X}(s), J(s), s) = 0, \tag{13}$$

which is chosen such that s approximates the arclength of the solution branch in a given phase space [16-17]. Rather than solving the coupled system in (12) and (13), we replace J by a function $\mathcal{J}$ of z and we let the unknown $\mathcal{Z} = (\mathcal{X}^T, \mathcal{J})^T$ be the solution of a three-point limit value problem

$$\mathcal{H}(\mathcal{Z}, s) = \begin{bmatrix} \mathcal{F}(\mathcal{X}, \mathcal{J}) \\ \dfrac{d\mathcal{J}}{dz} \\ \mathcal{N}(\mathcal{X}(\hat{z}), \mathcal{J}(\hat{z}), s) \end{bmatrix} = 0, \tag{14}$$

where $\hat{z}$ is a given point in $[0, L]$. The main advantage of considering (14) is that, if (12) can be discretized in a block-tridiagonal form, then (14) has the same property. The numerical Jacobian matrix obtained from (14) has a block-tridiagonal structure and one can prove easily that it is nonsingular at simple turning points. Specially developed block tridiagonal linear equation solvers can then be used to invert the corresponding linear systems.

The system in (14) is solved by combining a first-order Euler predictor and a corrector step involving Newton-like iterations and adaptive gridding. To resolve the high activity regions of the dependent solution components, the mesh must be refined in the continuation calculations. Specifically, after solving the governing equations on a previously determined mesh, we determine a new equidistributed mesh

$$\mathcal{Z}^* = \{0 = z_1^* < z_2^* < \ldots < z_{n^*}^* = L\}, \tag{15}$$

by imposing the condition

$$\int_{z_i^*}^{z_{i+1}^*} w \ dz = 1, \quad 1 \leq i \leq n^* - 1, \tag{16}$$

where the weight function w depends upon the gradient and curvature of the dependent solution components and on mesh regularity properties. The governing equations are solved on this new mesh and then another continuation step is taken. It optimizes the number of points and determines the new grid in only one pass. In addition, the method also takes into account every component of the solution in forming a new mesh.

Results and Discussion

In this section we discuss the results of a sequence of numerical calculations in which the dependence of the soot volume fraction as a function of the strain rate is investigated for methane-air and ethylene-air diffusion flames. All the calculations were done at one

atmosphere with the fuel and oxidizer streams having temperatures of 298K. The lengths of the computational domains were 5.00 cm for ethylene and 4.25 cm for methane. A total of 20 soot size classes was used in the computations. Each continuation calculation contained between 125-175 adaptively determined grid points and all of the calculations were performed on an IBM RS/6000 Model 560 computer. Approximately 1000 solutions taking 75 hours of CPU time were needed to generate the upper branch of the C-shape solution curve for ethylene and approximately 350 solutions taking 25 hours of CPU time were needed for methane.

In Figure 4 we display the variation of the peak temperature vs. the strain rate for both sets of flames. Notice the large difference in the extinction strain rates between the two cases. Using the strain rate defined in (10), we determined an extinction strain rate of 338 sec^{-1} for methane and 1150 sec^{-1} for ethylene. When the strain rate is defined as the maximum axial velocity gradient on the oxidizer side, we compute an extinction strain rate for methane of 620 sec^{-1}. With this same strain rate definition, the experimental value reported in [6] is 380 sec^{-1}. Since this computed value is far outside what should be considered acceptable agreement, the strain rate at extinction has also been computed using a mechanism utilized in our prior study (Hall, Smooke, and Colket, 1997). With that mechanism, the strain rate at extinction was calculated to be 390 sec^{-1}. The peak volume fractions as predicted from this earlier mechanism at low strain rates were comparable to those from the modified version of GRIMech.

Calculations neglecting radiation losses were also performed. Radiation effects are relatively small for ethylene flames for strain rates above approximately 100 sec^{-1} (about 13K depression at 40 sec^{-1} and 6K depression at 80 sec^{-1}). For lower strain rates the gas cooling effects of radiation are important and have a significant influence on both methane and ethylene temperature profiles. In particular, we have computed methane flames down to strain rates of 6 sec^{-1}; for these low strain rate flames radiative cooling effects are on the order of 100K. For ethylene flames, calculations were calculated down to 15 sec^{-1}; the corresponding cooling effect is 45K. The rapid reduction in the peak temperature for the both the ethylene and methane flames at low strain may be unphysical due to the neglect of self-absorption inherent in the optically thin model.

The corresponding profiles of maximum soot volume fraction are shown in Figure 5 for the methane-air and ethylene-air flames. The very low values for the methane flame and its rapid decline are consistent with the known difficulty of stabilizing a sooting methane-air flame in the laboratory. The variation of volume fraction in the ethylene flames has been shown to be reasonably consistent with experimental measurements of volume fraction strain rate sensitivity [25].

The importance of fully coupling the radiation and scrubbing processes within the flame and soot equations can be clearly demonstrated under low strain rate conditions.

The 45K increase in temperature when thermal radiation loss was excluded in ethylene at 15 sec^{-1} increases peak volume fraction by 75%. Furthermore, when both scrubbing and radiation effects are not included in the model the temperature increases by another 25K and soot by another factor of two. These effects are even more dramatic in the case of the low strain rate methane flame at 6 sec^{-1} where the 100K increase in flame temperature with radiation excluded leads to a factor of five increase in the peak soot volume fraction! As stated, however, the neglect of self-absorption undoubtedly overestimates the radiation losses and, thus, the predictions in Fig. 5 are likely low.

Figures 6 and 7 show the variation in peak mole fractions of key growth species for the ethylene and methane flames. Of interest are the relatively 'flat' profiles of the acetylene concentration (a factor of three change) and of the benzene concentration (only an order of magnitude decrease). These numbers are contrasted with the very dramatic drop in the soot volume fraction nearly five orders of magnitude decay for the ethylene flame (Figure 5). While hydrogen is also decaying, the change in species concentrations alone cannot account for the dramatic drop in soot volume fraction. The temperature dependence of the inception process is small (10–13 kcal/mole), while that of the growth rate is noticeably greater (31.8 kcal/mole). The change in this latter rate is only about a factor of three for the calculated temperature range (1750-2100K). While each of these processes contributes to the large decay in soot volume fraction, together they cannot account for the five order of magnitude decay. As shown in [11], oxidation plays a relatively minor role in soot production in opposed jet flames; hence, an increase in the oxidation rate probably does not explain the decline either. A remaining explanation is the very significant decrease in residence time. For the strain rate variation of 15 sec^{-1} to 1150 sec^{-1} for the ethylene flame, this represents approximately a factor of 75 decrease in residence time. This parameter is likely the most important factor in the significant decay of soot volume fraction in the ethylene flame; and the decay in the concentration of the first aromatic ring is the second most important parameter.

Acetylene levels in the methane flame (Figure 7) are slightly lower than in the ethylene flame and benzene is about an order of magnitude lower (Figure 6). These differences as well as the lower peak flame temperatures contribute to the much lower soot from the methane flame.

Figure 8 shows a comparison of the soot variation with strain rate for the present model and that of the model of Fairweather et al. [29]. The inception rate and the surface growth rate in the latter model are both proportional to acetylene with activation energies of 42.0 and 24.0 kcal/mole, respectively. This is usually a monodisperse model; in this work, it has been incorporated into the sectional representation. The fact that the relative variation with strain rate is similar for the two models, in spite of the considerable functional differences and the fact that the Fairweather, et al. model is dependent only on the acetylene concentration, strongly supports the previous agrument regarding the

importance of residence time. The fact that peak soot volume fractions predicted from our model fall off slightly more rapidly than those predicted using the Fairweather model is presumably due to a combination of the lower activation energy of the surface growth step in the Fairweather model and the order of magnitude decrease in benzene to which our inception model is sensitive.

Conclusions

Arclength continuation methods have been incorporated into an opposed jet soot prediction code with complex chemistry, detailed particle transport/kinetics, and radiation. The continuation technique greatly reduces the effort required to carry out parametric variations with opposed jet programs. Calculations have been carried out for the strain rate dependence of atmospheric pressure methane-air and ethylene-air counterflow diffusion flames. Comparisons with experimental data, examination of the effects of thermal radiation, and discussion of the main factors governing the strain rate dependence of soot formation in these flames have been presented.

Acknowledgments

This work has been supported in part by the Air Force Office of Scientific Research and the United States Department of Energy, Office of Basic Energy Sciences. The encouragement of Julian Tishkoff is greatly appreciated. Discussions with M. Tanoff are gratefully acknowledged.

References

1. Smooke, M. D., Puri, I. K., and Seshadri, K.: Twenty-First Symposium (International) on Combustion, p. 1783, The Combustion Institute, (1986).

2. Smooke, M. D., Seshadri, K., and Puri, I. K.: Twenty-Second Symposium (International) on Combustion, p. 1555, The Combustion Institute, (1988).

3. Sick, V., Arnold, A., Diessel, E., Dreier, T., Ketterle, W., Lange, B., Wolfrum, J., Thiele, K. U., Behrendt, F. and Warnatz, J.: Twenty-Third Symposium (International) on Combustion, p. 495, The Combustion Institute, (1990).

4. Chelliah, H. K., Law, C. K., Ueda, T., Smooke, M. D., and Williams, F. A.: Twenty-Third Symposium (International) on Combustion, p. 503, The Combustion Institute, (1990).

5. Chelliah, H. K., Bui-Pham, M., Seshadri, K., and Law, C. K.: Twenty-Fourth Symposium (International) on Combustion, p. 851, The Combustion Institute, (1992).

6. Du, D. X., Axelbaum, R. L., and Law, C. K.: Twenty-Second Symposium (International) on Combustion, p. 387, The Combustion Institute, (1988).

7. Du, D. X., Axelbaum, R. L., and Law, C. K.: Twenty-Third Symposium (International) on Combustion, p. 1501, The Combustion Institute, (1990).

8. Hura, H. S. and Glassman, I.: Twenty-Second Symposium (International) on Combustion, p. 371, The Combustion Institute, (1988).

9. Vandsburger, U., Kennedy, I. M., and Glassman, I.: Twentieth Symposium (International) on Combustion, p. 1105, The Combustion Institute, (1984).

10. Axelbaum, R. L., Law, C. K., and Flower, W. L.: Twenty-Second Symposium (International) on Combustion, p. 379, The Combustion Institute, (1988).

11. Hall, R. J., Smooke, M. D., and Colket, M. B.: in Physical and Chemical Aspects of Combustion: A Tribute to Irvin Glassman, ed. by R. F. Sawyer and F. L. Dryer, Combustion and Science Technology Book Series, Gordon and Breach, to be published 1996.

12. Zhang, C., Atreya, A., and Lee, K.: Twenty-Fourth Symposium (International) on Combustion, p. 1049, The Combustion Institute, (1992).

13. Colket, M. B. and Hall, R. J.: in Soot Formation in Combustion, Mechanisms and Models, H. Bockhorn, Ed., Springer Series in Chemical Physics 59, Springer-Verlag, (1994).

14. Colket, M.B., and Hall, R.J., "Mechanisms Controlling Soot Formation in Diffusion

Flames" Annual Report for AFOSR Contract F49620-94-C-0059, August, 1995.

15. Peters, N., Prog. Energy Comb. Sci. **10**, p. 319, (1984).

16. Keller, H. B.: Numerical Solution of Bifurcation and Nonlinear Eigenvalue Problems, in Applications of Bifurcation Theory, P. Rabinowitz, Ed., Academic Press, New York, (1977).

17. Giovangigli, V. and Smooke, M. D.: Applied Numerical Mathematics, **5**, p. 305, (1989).

18. Gelbard, F., and Seinfeld, J. H., J. Coll. Int. Sci., **78**, p. 485, (1980).

19. Harris, S. J., and Weiner, A.M., Combustion Science and Technology, **31**, p. 155, (1983).

20. Axelbaum, R.L., Flower, W.L., and Law, C.K., Combustion Science and Technology, **61**, p. 51, (1988).

21. Kennedy, I.M., Kollmann, W., and Chen, J.Y., Combustion and Flame, **81**, p. 73, (1990).

22. Sunderland, P. B. and Faeth, G. M., Combustion and Flame, **105**, p. 132, (1996).

23. Puri, R., Richardson, T. F., Santoro, R. J. and Dobbins, R.A., Combustion and Flame, **92**, p. 320 (1993).

24. Bowman, C. T., Hanson, R. K., Davidson, D. F., Gardiner Jr., W. C., Lissianski, V., Smith, G. P., Golden, D. M., Frenklach, M., Wang, H., and Goldenberg, M.,: GRI-Mech version 2.11, http://www.gri.org, (1995).

25. Wang, H., Du, D. X., Sung, C. J. and Law, C. K., Twenty-Sixth Symposium (International) on Combustion, The Combustion Institute (1996).

26. Benish, T. G., Lafleur, A. L., Taghizadeh, K., Howard, J. B., Twenty-Sixth Symposium (International) on Combustion, The Combustion Institute (1996).

27. Smooke, M. D., Crump, J., Seshadri, K. and Giovangigli, V., Twenty-Third Symposium (International) on Combustion, p. 463, The Combustion Institute, (1991).

28. Kim, J.S., Libby, P.A., and Williams, F.A., Combustion Science and Technology, **87**, p. 1, (1992)

29. Fairweather, M., Jones, W.P., and Lindstedt, W.P., Combustion and Flame, **89**, p. 45, (1992).

Figure Captions

1. Coordinate system for counterflow flame analysis.

2. Comparison of computed and experimental velocity profiles. Data for opposed jet flames #1 and #4 of Wang *et al.* [25].

3. Comparison of computed and experimental soot volume fraction profiles. Data for opposed jet flames #1 and #4 of Wang *et al.* [25].

4. Peak temperature variation as a function of strain rate for ethylene and methane-air counterflow diffusion flames.

5. Peak volume fraction variation as a function of strain rate for ethylene and methane-air counterflow diffusion flames.

6. Variation of acetylene and benzene mole fractions with strain rate for ethylene-air counterflow diffusion flames.

7. Variation of acetylene and benzene mole fractions with strain rate for methane-air counterflow diffusion flames.

8. Comparison of peak soot volume fraction versus strain rate for present model and the model of Fairweather et al. [29].

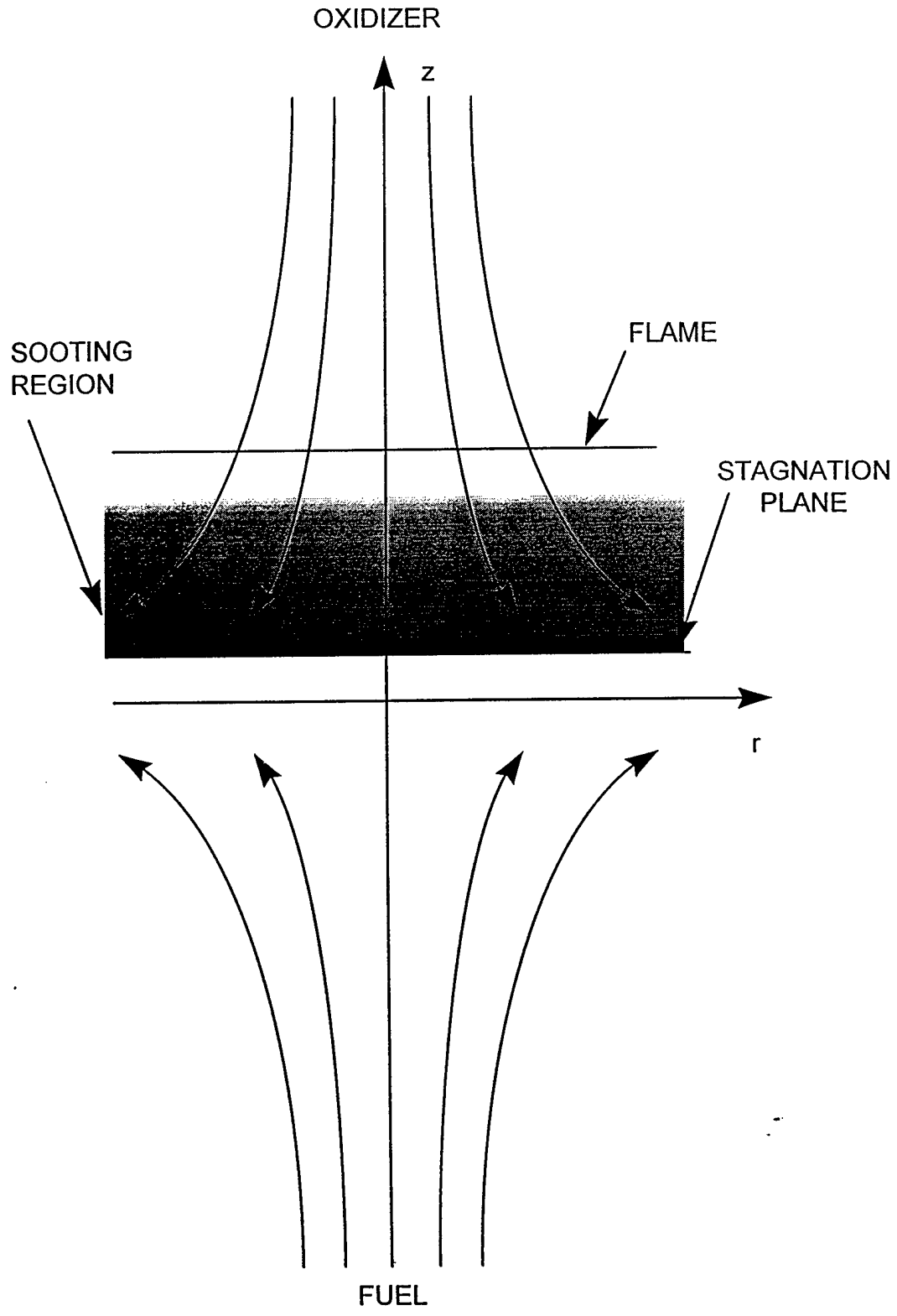

Figure 1

CRT18r.1

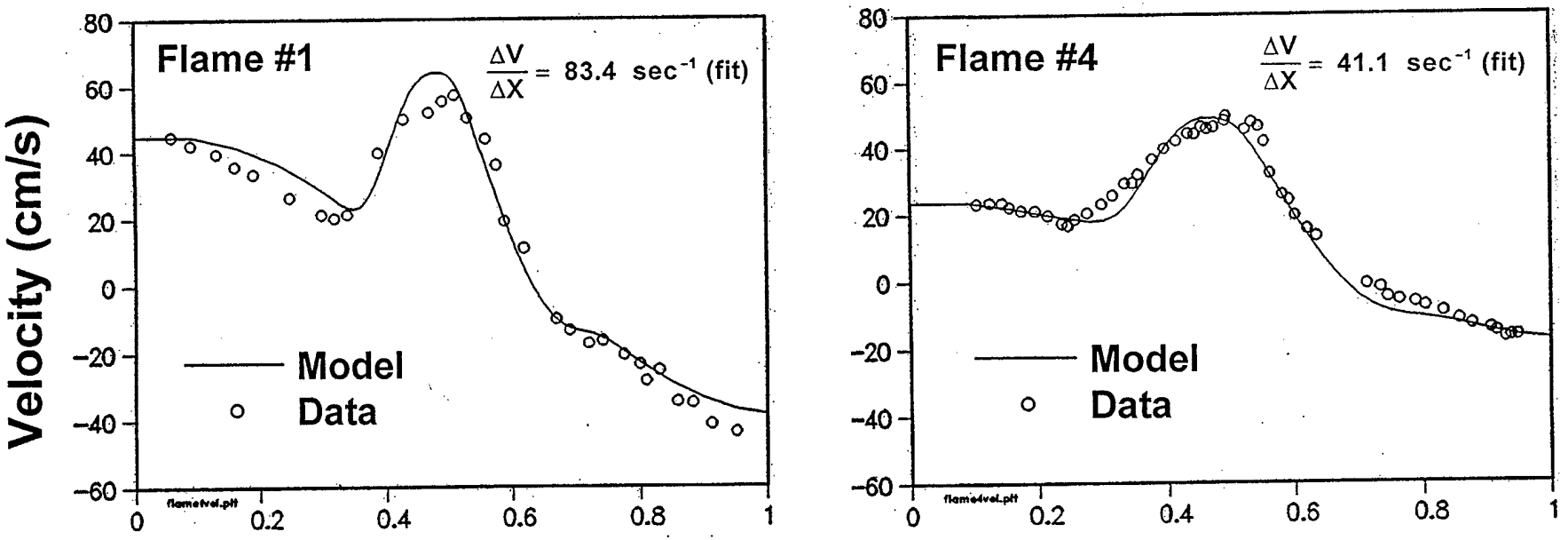

Figure 2

RJH13097.PPT

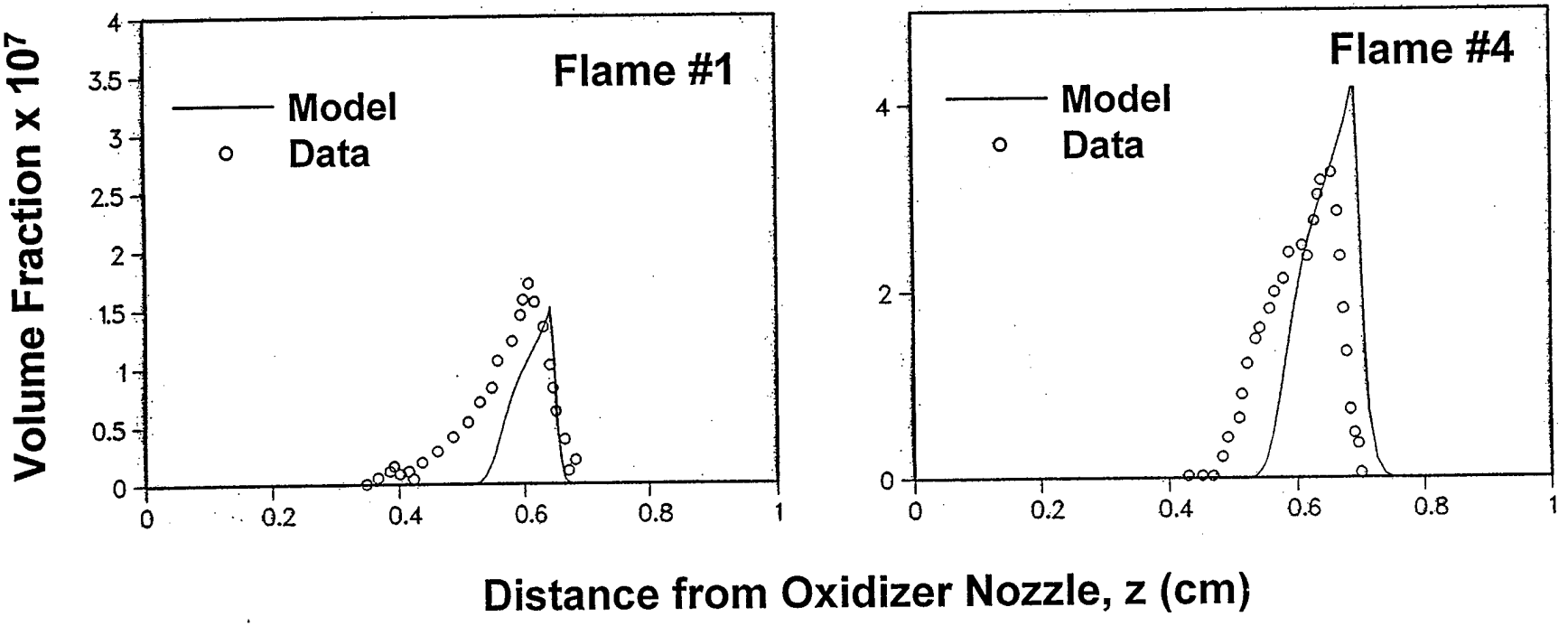

Figure 3

rjh30797.ppt

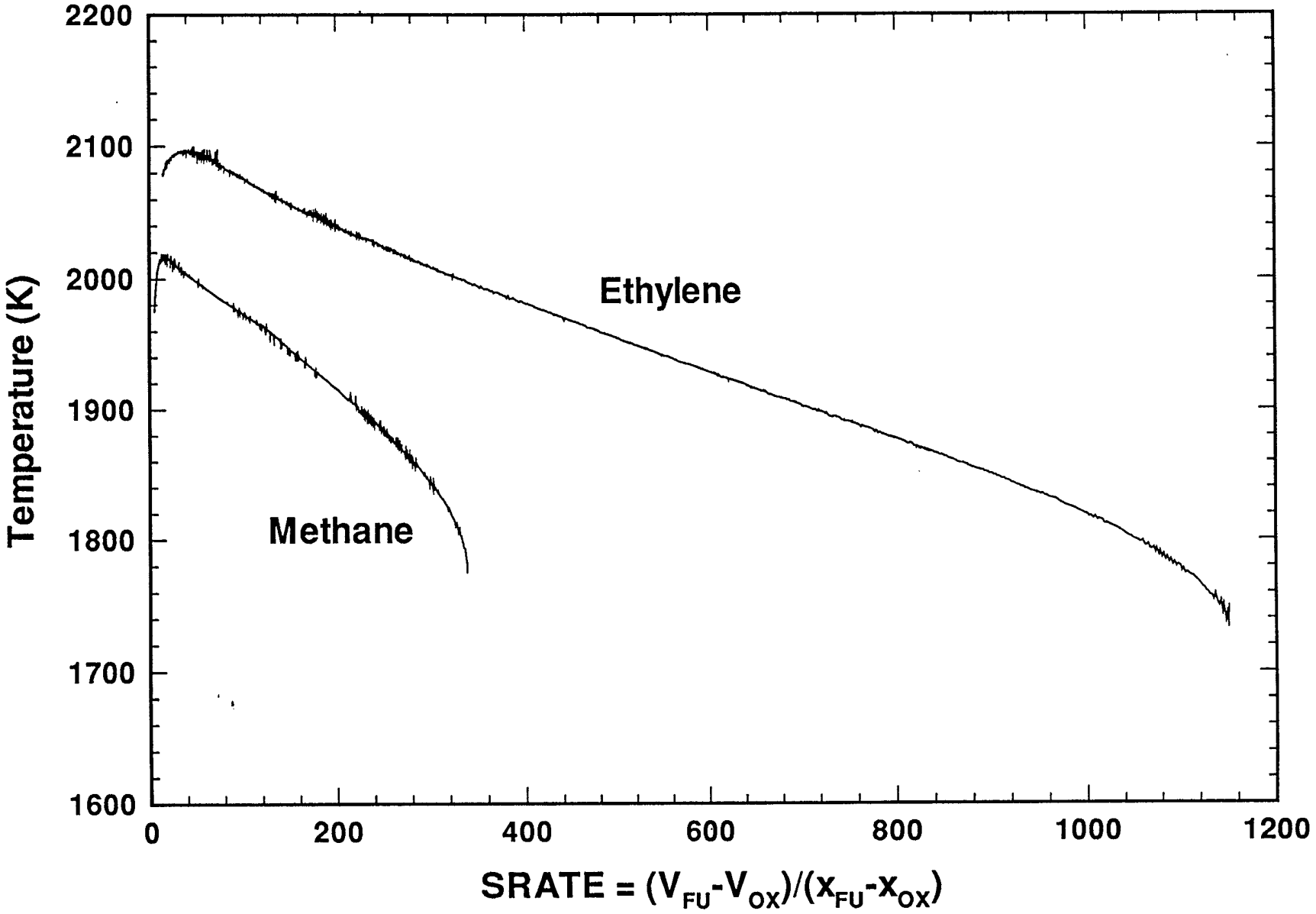
2200
2100
2000
1900
1800
1700
1600
Temperature (K)
Ethylene
Methane
0
200
400
600
800
1000
1200
SRATE = (V_FU-V_OX)/(x_FU-x_OX)

Figure 4

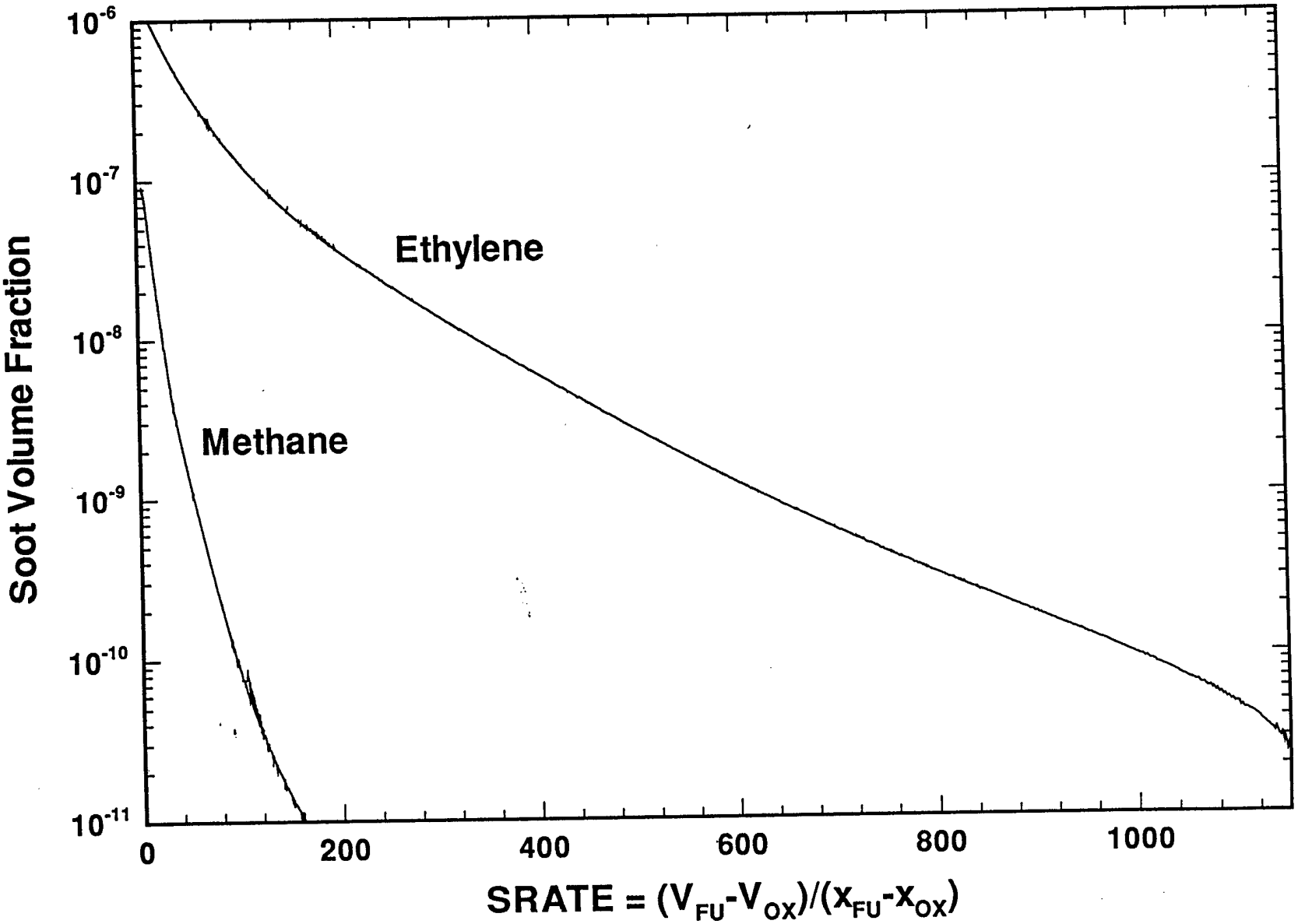
Soot Volume Fraction
10^-6
10^-7
10^-8
10^-9
10^-10
10^-11
Ethylene
Methane
0
200
400
600
800
1000
SRATE = (V_FU-V_OX)/(x_FU-x_OX)

Figure 5

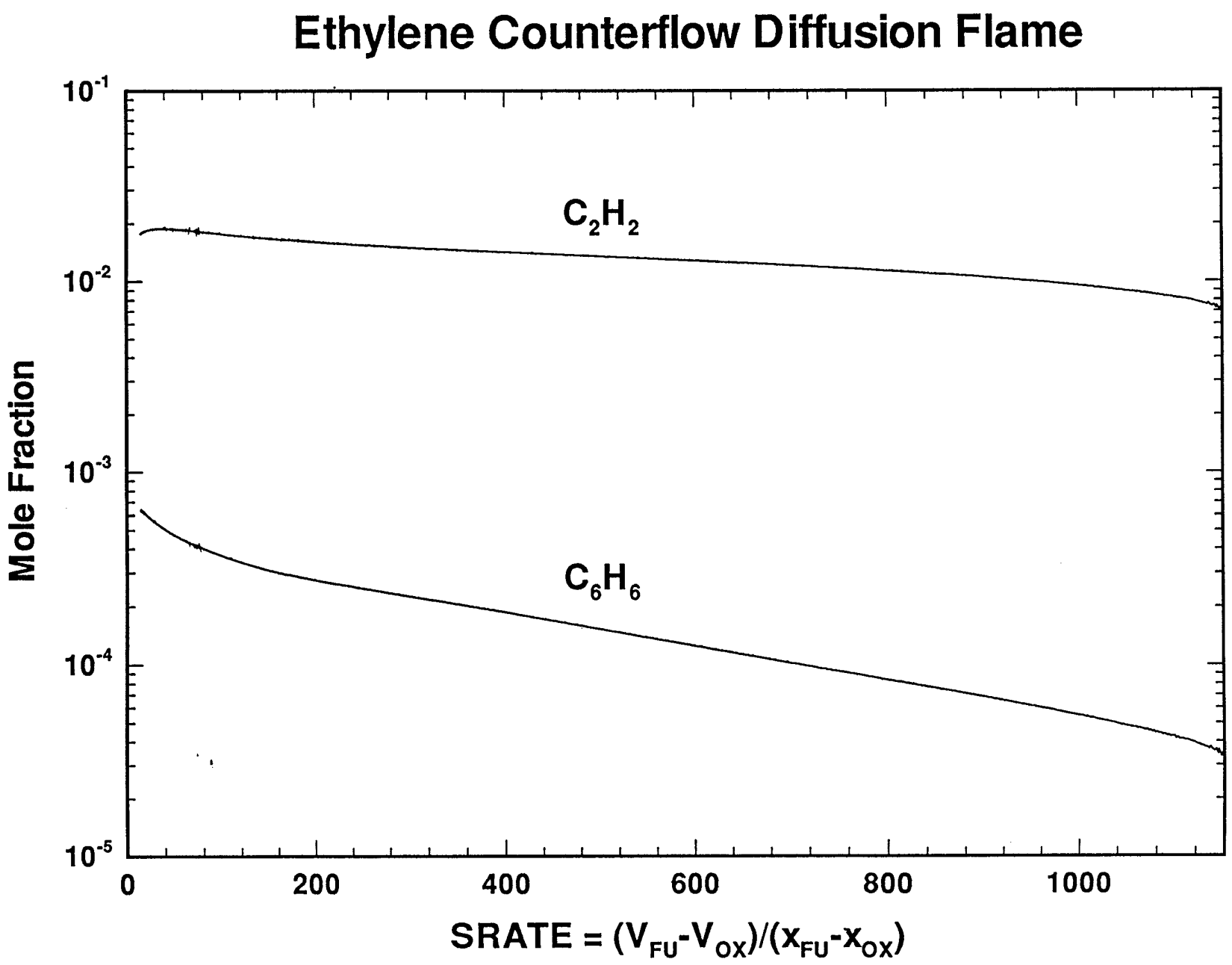
Ethylene Counterflow Diffusion Flame
Mole Fraction
10-1
10-2
10-3
10-4
10-5
C2H2
C6H6
0
200
400
600
800
1000
SRATE = (VFU-VOX)/(xFU-xOX)

Figure 6

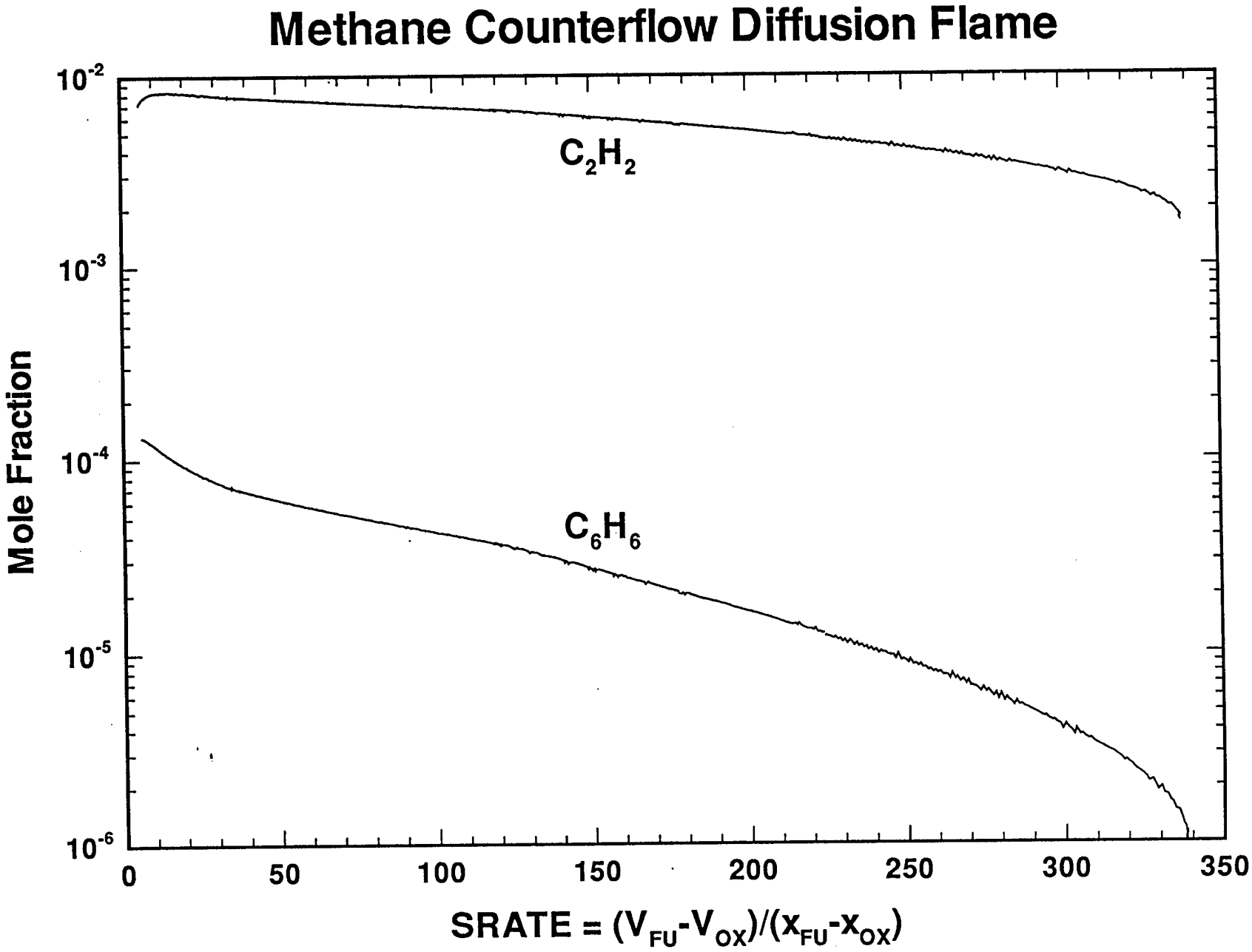
Methane Counterflow Diffusion Flame
Mole Fraction
10^{-2}
10^{-3}
10^{-4}
10^{-5}
10^{-6}
C_2H_2
C_6H_6
0
50
100
150
200
250
300
350
SRATE = $(V_{FU}-V_{OX})/(x_{FU}-x_{OX})$

Figure 7

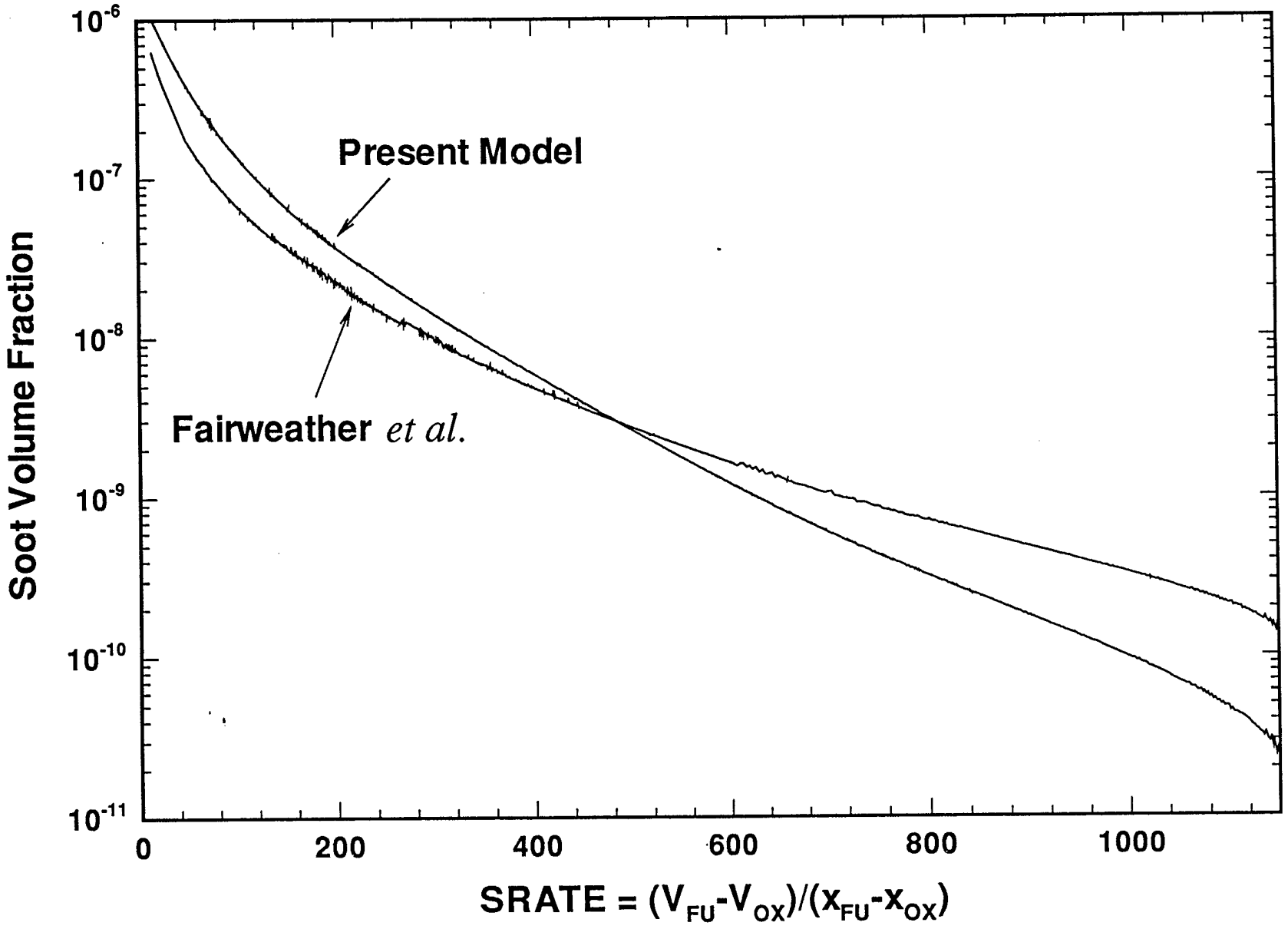
Soot Volume Fraction
10-6
10-7
10-8
10-9
10-10
10-11
Present Model
Fairweather et al.
0
200
400
600
800
1000
SRATE = (VFU-VOX)/(xFU-xOX)

Figure 8

Appendix B
Computational and Experimental Study of Soot Formation in a Coflow, Laminar Diffusion Flame

COMPUTATIONAL AND EXPERIMENTAL STUDY OF SOOT FORMATION IN A COFLOW, LAMINAR DIFFUSION FLAME

M. D. Smooke, C. S. McEnally, L. D. Pfefferle
Yale Center for Combustion Studies
Yale University, New Haven, CT 06520
and
R. J. Hall and M. B. Colket
United Technologies Research Center
E. Hartford, CT 06108

Abstract

A detailed soot growth model in which the dynamical equations for particle production have been coupled to the flow and gaseous species conservation equations has been developed for an axisymmetric, laminar, coflow diffusion flame. Results from the model have been compared to experimental data for a confined methane-air flame. The two-dimensional system couples detailed transport and finite rate chemistry in the gas phase with the aerosol dynamical equations in the sectional representation. The formulation includes detailed treatment of the transport, inception, surface growth, oxidation, and coalescence of soot particulates. Effects of thermal radiation and particle scrubbing of gas phase growth and oxidation species are also included. Predictions and measurements of temperature, soot volume fractions and selected species are compared over a range of heights and as a function of radius. Flame heights are slightly overpredicted and local temperatures and volume fractions are underpredicted. We believe the inability to reproduce accurately bulk flame parameters directly inhibits the ability to predict soot volume fractions and these differences are likely a result of uncertainties in the experimental inlet conditions. Predictions of the distributions of particle sizes indicate the existence of (relatively) low molecular weight species along the centerline of the burner and trace amounts of the particles which escape from the flame, unoxidized. Oxidation of particulates is dominated by reactions with hydroxyl radicals which attain levels approximately ten times higher than calculated equilibrium levels. Gas cooling effects due to radiative loss are shown to have a very significant effect on predicted soot concentrations.

COMPUTATIONAL AND EXPERIMENTAL STUDY OF SOOT FORMATION IN A COFLOW, LAMINAR DIFFUSION FLAME

1. Introduction

In the last few years, we have witnessed a shift in combustion research. The push for higher combustion efficiency in propulsion applications that dominated much of research in the past few decades is gradually being replaced by a drive towards *cleaner* combustion. This is a direct result of environmental consciousness and it has been translated into stricter air quality legislation. Although it originated as a reaction to regulatory pressure, research in the area of pollutant formation and control will become economically indispensable to the export of combustion-related technologies and products worldwide. In particular, as emissions legislation becomes more restrictive, a detailed understanding of soot formation and unburned hydrocarbons in flames will be critical for the design of pollutant abatement strategies and for the preservation of the competitiveness of combustion related industries.

Modeling soot formation in practical combustion systems is an extremely challenging problem. Reacting flow problems for simple fuels such as methane can require the solution of more than 50 chemical species in addition to the temperature *and* the fluid dynamic variables. The inclusion of soot inception, growth and oxidation processes in these models greatly increases the level of complexity of the problem. In fact, due to the number of dependent unknowns and the resolution with which reaction fronts need to be resolved, *gas phase* combustion calculations with detailed chemistry have only recently moved from one- to two- and some three-dimensional systems. The increased effort with which multidimensional combustion phenomena have been studied numerically is attributable in part to advances in the development of computational algorithms, and in part to higher speed/larger memory workstations. This combination has enabled the combustion scientist to investigate chemically reacting systems that were computationally infeasible only a few years ago. Nevertheless, the investigation of soot formation with detailed chemistry in a generic multidimensional configuration is still beyond our current computational ability. The laminar diffusion flame, however, provides a natural environment in which one can investigate the interaction of soot formation with detailed gas-phase chemistry in a multidimensional system.

Most studies using detailed chemical kinetics and coupled models of soot production and oxidation have focused on one-dimensional geometries. A few recent studies [Kaplan *et al.*, 1996, Kennedy *et al.*, 1996] have focused on jet diffusion flames, using simplified, monodisperse, soot formation models with skeletal kinetic mechanisms. In this paper we modify the sectional soot formation model developed in Colket and Hall (1994) and Hall *et al.* (1997) for incorporation into a laminar, axisymmetric, diffusion flame in which a cylin-

drical fuel stream is surrounded by a coflowing oxidizer jet. Computationally, we employ a velocity-vorticity model (Ern *et al.*, 1995) in which the governing conservation equations are solved with detailed transport and finite rate chemistry submodels to predict the temperature, species mass fractions and velocity fields as functions of the two independent coordinates. Appropriate sectional equations are included for describing the different soot particle size classes with a convective, diffusive and chemical production balance. These equations, along with surface growth, oxidation and radiation (from both gas and particulate species) are fully integrated with the governing equations. A discrete solution is obtained on a two-dimensional grid by employing Newton's method with adaptive mesh refinement. In many models diffusion in the axial direction is neglected: here, we consider the fully elliptic problem. Experimentally, we utilize thermocouple particle densitometry and mass spectrometry to obtain profiles of the soot volume fraction and the species concentrations at various heights in the flame (McEnally and Pfefferle, 1997). We apply the computational model and experimental methods to a lightly sooting methane-air diffusion flame. In the next section, we formulate the problem. In Section 3, we describe the experimental approach. The computational method is discussed in Section 4 and results of the study are contained in Section 5.

2. Problem Formulation

While the ultimate goal in combustion modeling is the solution of three-dimensional turbulent reacting flows with finite rate chemistry, there are still important less complex systems that can be analyzed in detail with current computational resources. The axisymmetric, laminar, diffusion flame is one such configuration (Smooke *et al.*, 1990, 1992, 1996; Xu *et al.*, 1993; Ern *et al.*, 1995) This is the flame type of most practical combustion devices and it is important in understanding interactions of heat and mass transfer with chemical reactions in gas turbines and commercial burners. The ability to predict the coupled effects of complex transport phenomena with detailed chemical kinetics in these systems is critical in the modeling of turbulent reacting flows, in improving engine efficiency and in understanding the processes by which pollutants are formed.

2.1 Soot Modeling

Soot kinetics are modeled as coalescing, solid carbon spheroids undergoing surface growth in the free molecule limit. The particle mass range of interest is divided into sections (Gelbard and Seinfeld, 1980), and a dynamical equation is written for each section including coalescence, surface growth, and oxidation. Sectional analysis makes it possible to obtain the particle size distribution without a-priori assumptions about the form of the distribution. For the first bin, an inception source term is included. The incorporation of these dynamical equations into a transport/conservation equation for each section includes both thermophoresis and an effective bin diffusion rate. In the gas species conservation

equations, provision is made for complex chemistry; additional source terms are included to account for scrubbing or generation of gaseous species arising from the particle growth and oxidation processes. The gas and soot are additionally coupled through non-adiabatic radiative loss from both the gas and the soot in the optically-thin approximation. For one atmosphere calculations, the sectional coefficients for transport, coalescence and surface processes are calculated in the free molecule limit (Gelbard and Seinfeld, 1980), with surface growth and oxidation proportional to particle surface area. In the free molecule limit, the particle mass and medium dependencies of the sectional coefficients are factored in such a way that they only have to be evaluated once. Oxidation of soot by O_2 and OH is treated as described in (Hall *et al.*, 1997). The inception model employed here is based on an estimate of the formation rate of two- and three-ringed aromatic species, and is a function of local acetylene, benzene, phenyl and molecular hydrogen concentrations. Assuming steady-state values of intermediates, and also that $H_2 >> C_2H_2$, the rate of production of the polyaromatic species can be estimated to be (Hall *et al.*, 1997)

$$\frac{d[\dot{C_{10}H_7}]}{dt} = 10^{11.88} e^{(-4378/T)} \frac{[C_2H_2]^2}{[H_2]} [\dot{C_6H_5}] \text{ cc/mole/sec}, \tag{2.1}$$

and

$$\frac{d[C_{14}H_{10}]}{dt} = 10^{12.50} e^{(-6390/T)} \frac{[C_2H_2]}{[H_2]} [C_6H_6][\dot{C_6H_5}] \text{ cc/mole/sec}, \tag{2.2}$$

where the gas phase concentrations and temperatures are evaluated at local conditions. With the further assumptions that inception is limited by the formation of polyaromatics and oxidation/decomposition of such species can be neglected, the inception rate, S_i, in grams/cc/sec, was initially assigned to

$$S_i = 127 \times \frac{d[\dot{C_{10}H_7}]}{dt} + 178 \times \frac{d[C_{14}H_{10}]}{dt}, \tag{2.3}$$

where the constants (molecular weights) are provided to convert from molar to mass units. The second term in equation 2.3 plays a negligible role in methane-air diffusion flames but has been included here for generality. The contributions from both inception processes are incorporated in the first sectional bin, whose lower mass boundary is set equal to the mass of the smallest inception species (See Section 5). In the sectional representation (Gelbard and Seinfeld, 1980), the sectional mass boundaries vary linearly on a logarithmic scale.

The surface growth rate is nominally that of Harris and Weiner (1983), who report a rate proportional to acetylene concentration; their rate is normalized in this application to 1650K, with a 31.8 kcal activation energy as suggested by Hura and Glassman (1988).

It has been found (Smooke *et al.*, 1997) that enhancing the Harris and Weiner rate by a factor of two results in predictions of soot levels in opposed jet ethylene flames in good agreement with measurements of Wang *et al.* (1997). The enhancement by a factor of two brings the Harris and Weiner rate, determined from studies on premixed ethylene flames, into better agreement with results obtained in diffusion flames (Axelbaum *et al.*, 1988, Kennedy *et al.*, 1990, Sunderland and Faeth, 1996).

The surface growth/inception models used in this paper agree well with available ethylene opposed jet data. Nevertheless, it is not suggested that they represent a universal solution to the problem of soot formation because comparisons with soot data in other fuels have not been carried out. The possibility of aging of the surface growth rate has not been accounted for here, nor are the results with finite coalescence appropriate for aggregate formation. These effects should be included in future modeling efforts. Fundamental questions relating to inception, temperature dependence of surface growth and precise dependence of surface growth on gas phase species concentrations remain. Whether soot growth rates derived from premixed and opposed jet studies are self-consistent is still an open issue as well.

A primary parameter of interest in this paper is the soot volume fraction, for which convergence is generally obtained with a smaller number of sections than is the case for particle size and number density (Hall *et al.*, 1997). The number of sections required for convergence must be examined in each case, although evidence points to the relative magnitudes of surface growth and inception as the important parameter. When the contribution of inception to total volume fraction is significant, although not necessarily dominating, the number of sections required can be very small (Hall *et al.*, 1997), with larger numbers necessary when the contribution of surface growth to volume fraction becomes very much larger than that from inception.

2.2 Governing Equations

If we combine the gas-phase diffusion flame model which employs a velocity-vorticity formulation (Ern *et al.*, 1995) with the sectional approach presented in Hall *et al.* (1997), the coupled set of governing partial differential equations can be written in the form

Radial Velocity

$$\frac{\partial^2 v_r}{\partial r^2} + \frac{\partial^2 v_r}{\partial z^2} = \frac{\partial \omega}{\partial z} - \frac{\partial}{\partial r}\left(\frac{v_z}{\rho}\frac{\partial \rho}{\partial z}\right) - \frac{\partial}{\partial r}\left(\frac{v_r}{r}\right) - \frac{\partial}{\partial r}\left(\frac{v_r}{\rho}\frac{\partial \rho}{\partial r}\right), \tag{2.4}$$

Axial Velocity

$$\frac{\partial^2 v_z}{\partial r^2} + \frac{\partial^2 v_z}{\partial z^2} = -\frac{\partial \omega}{\partial z} - \frac{\partial}{\partial z}\left(\frac{v_z}{\rho}\frac{\partial \rho}{\partial z}\right) - \frac{\partial}{\partial z}\left(\frac{v_r}{r}\right) - \frac{\partial}{\partial z}\left(\frac{v_r}{\rho}\frac{\partial \rho}{\partial r}\right), \tag{2.5}$$

Vorticity Transport

$$r^2\left[\frac{\partial}{\partial z}\left(\frac{\omega}{r}\frac{\partial \psi}{\partial r}\right) - \frac{\partial}{\partial r}\left(\frac{\omega}{r}\frac{\partial \psi}{\partial z}\right)\right] - \frac{\partial}{\partial r}\left[r^3\frac{\partial}{\partial r}\left(\mu\frac{\omega}{r}\right)\right]$$
$$-\frac{\partial}{\partial z}\left[r^3\frac{\partial}{\partial z}\left(\mu\frac{\omega}{r}\right)\right] = r\left[-rg\frac{\partial \rho}{\partial r} - r\nabla\left(\frac{v_r^2 + v_z^2}{2}\right)\cdot \mathrm{iso}(\rho)\right], \tag{2.6}$$

Species

$$\rho v_r\frac{\partial Y_k}{\partial r} + \rho v_z\frac{\partial Y_k}{\partial z} + \frac{1}{r}\frac{\partial}{\partial r}\left(r\rho Y_k V_{kr}\right) + \frac{\partial}{\partial z}\left(\rho Y_k V_{kz}\right) -$$
$$W_k(\dot{w}_k + \dot{w}_k^s) = 0, \qquad k = 1, 2, \ldots, K, \tag{2.7}$$

Sections

$$\rho v_r\frac{\partial Y_k}{\partial r} + \rho v_z\frac{\partial Y_k}{\partial z} + \frac{1}{r}\frac{\partial}{\partial r}\left(r\rho Y_k(V_{kr}^s + V_{Tr})\right) + \frac{\partial}{\partial z}\left(\rho Y_k(V_{kz}^s + V_{Tz})\right)$$
$$-\dot{q}_k = 0, \qquad k = K+1, K+2, \ldots, K+M, \tag{2.8}$$

Energy

$$c_p\left(\rho v_r\frac{\partial T}{\partial r} + \rho v_z\frac{\partial T}{\partial z}\right) - \frac{1}{r}\frac{\partial}{\partial r}\left(r\lambda\frac{\partial T}{\partial r}\right) - \frac{\partial}{\partial z}\left(\lambda\frac{\partial T}{\partial z}\right) +$$
$$\sum_{k=1}^{K}\rho c_{p_k} Y_k\left(\frac{\partial T}{\partial r}V_{kr} + \frac{\partial T}{\partial z}V_{kz}\right) + \sum_{k=1}^{K} h_k W_k(\dot{w}_k + \dot{w}_k^s) - \nabla\cdot q_r = 0, \tag{2.9}$$

Equation of State

$$\rho = \frac{p\overline{W}}{RT}. \tag{2.10}$$

The system is closed with appropriate boundary conditions on each side of the computational domain. For a confined coflowing flame we have

Axis of Symmetry ($r = 0$):

$$v_r = \frac{\partial v_z}{\partial r} = \frac{\partial \omega}{\partial r} = \frac{\partial Y_k}{\partial r} = \frac{\partial T}{\partial r} = 0, \quad k = 1, 2, \ldots, K + M, \tag{2.11}$$

Exit ($z \to \infty$):

$$v_r = \frac{\partial v_z}{\partial z} = \frac{\partial \omega_r}{\partial z} = \frac{\partial Y_k}{\partial z} = \frac{\partial T}{\partial z} = 0, \quad k = 1, 2, \ldots, K + M, \tag{2.12}$$

Inlet ($z = 0$):
$r < R_I$

$$\begin{aligned} v_r &= 0, \\ v_z &= v_F, \\ \omega &= \frac{\partial v_r}{\partial z} - \frac{\partial v_z}{\partial r}, \\ Y_k &= Y_{k_F}, \quad k = 1, 2, \ldots, K + M, \\ T &= T_F, \end{aligned} \tag{2.13}$$

$R_I < r < R_O$

$$\begin{aligned} v_r &= 0, \\ v_z &= v_{OX}, \\ \omega &= \frac{\partial v_r}{\partial z} - \frac{\partial v_z}{\partial r}, \\ Y_k &= Y_{k_{OX}}, \quad k = 1, 2, \ldots, K + M, \\ T &= T_{OX}, \end{aligned} \tag{2.14}$$

Wall ($r = R_O$):

$$\begin{aligned} v_r = v_z &= 0, \\ \omega &= \frac{\partial v_z}{\partial r}, \\ \frac{\partial Y_k}{\partial r} &= 0, \quad k = 1, 2, \ldots, K + M, \\ T &= T_{wall}. \end{aligned} \tag{2.15}$$

The subscripts I and O refer to the inner jet and the outer jet, respectively, and v_F, v_{OX}, $Y_{k_F}, Y_{k_{OX}}, T_F, T_{OX}$ and T_{wall} are specified quantities.

In addition to the variables already defined, K represents the total number of gas phase species and M, the number of soot (size) sections; T, denotes the temperature; Y_k, the mass fraction of the k^{th} gas-phase species ($k \leq K$) or the $(k-K)^{th}$ soot size class ($k > K$); p, the pressure; v_r and v_z, the velocities of the fluid mixture in the radial and axial directions, respectively; ρ, the mass density; W_k, the molecular weight of the k^{th} species; $\overline{W}$, the mean molecular weight of the mixture; R, the universal gas constant; λ, the thermal conductivity of the mixture; c_p, the constant pressure heat capacity of the mixture; c_{pk}, the constant pressure heat capacity of the k^{th} species; $\dot{w}_k$, the molar rate of production of the k^{th} species per unit volume; $\dot{w}_k^s$, the molar rate of production of the k^{th} species per unit volume due to scrubbing/replenishment by the soot growth/oxidation processes; $\dot{q}_k$, the rate of change of section k due to inception, surface growth, oxidation and coalescence; h_k, the specific enthalpy of the k^{th} species; g, the gravitational constant; μ the viscosity of the mixture; V_{k_r} and V_{k_z}, the diffusion velocities of the k^{th} species in the radial and axial directions, respectively; $V_{Tr}, V_{Tz}, V_{kr}^s, V_{kz}^s$, sectional thermophoretic and diffusion velocities of the k^{th} soot size class and $\nabla \cdot q_r$ the divergence of the net radiative flux for gas bands and soot in the optically-thin limit.

We write the diffusion velocities in the r and z directions in the form

$$V_{k_r} = -(1/X_k) D_k \frac{\partial X_k}{\partial r}, \quad k = 1, 2, \ldots, K, \tag{2.16}$$

$$V_{k_z} = -(1/X_k) D_k \frac{\partial X_k}{\partial z}, \quad k = 1, 2, \ldots, K, \tag{2.17}$$

where X_k is the mole fraction of the k^{th} species and D_k is related to the binary diffusion coefficients through the relation (see, e.g., Curtiss and Hirschfelder, 1949)

$$D_k = \frac{(1 - Y_k)}{\sum_{j \neq k}^{K} X_j / \mathcal{D}_{jk}}. \tag{2.18}$$

The sectional thermophoretic velocities in the free molecule regime are given by (Hall *et al.*, 1997)

$$V_{Tr} = -0.55 \frac{\mu}{\rho} \frac{1}{T} \frac{\partial T}{\partial r}, \tag{2.19}$$

$$V_{Tz} = -0.55 \frac{\mu}{\rho} \frac{1}{T} \frac{\partial T}{\partial z}. \tag{2.20}$$

The sectional diffusion velocities are written as in (2.16-2.17) with a mass weighted mean diffusion coefficient for each bin (Hall *et al.*, 1997). The binary diffusion coefficients, the viscosity, the thermal conductivity of the mixture, the chemical production rates and the thermodynamic quantities were evaluated using vectorized and highly optimized transport and chemistry libraries (Giovangigli and Darabiha, 1987).

Anticipating that radiative losses could have a significant influence on soot levels compared to a nonradiative system, we have included an optically-thin radiation model in

our calculations (Hall, 1993, 1994). We assume that for methane-air mixtures the only significant radiating species are H_2O, CO and CO_2. By utilizing an optically-thin limit in which self-absorption of radiation is neglected, the divergence of the net radiative flux can be written

$$\nabla \cdot q_R = C f_v T^5 + 4\pi \sum_{ik} \alpha_{ik} \rho_k I_{b_{ik}}, \tag{2.21}$$

where f_v is the soot volume fraction and $I_{b_{ik}}$ is the Planck function evaluated at the gas band centers of the contributing vibration-rotation or pure rotational bands whose integrated intensities are given by α_{ik}.

3. Experimental Methods

3.1 Burner and Reactants

Atmospheric pressure, overventilated, axisymmetric, coflowing, nonpremixed laminar flames were generated with a burner in which the fuel flows from an uncooled 12 mm diameter vertical brass tube and the oxidizer flows from the annular region between this tube and a 102 mm diameter concentric tube (see Figure 1). Details of the burner construction and operation are given elsewhere (McEnally and Pfefferle, 1997). The oxidizer was air (710 cm^3/min), while the fuel was a mixture containing methane (240 cm^3/min) and argon (2.4 cm^3/min). The added argon aided species measurements as discussed below. All flowrates were governed by electronic mass flow controllers and are estimated to be accurate to within 5%.

3.2 Temperature and Soot Volume Fraction Measurements

Temperatures were measured with uncoated 75 μm wire-diameter type R thermocouples. By measuring profiles in coflowing flames with various size thermocouples, we have determined that while conduction errors of up to 100K occur at some flame locations with 125μm wires, they are negligible with 75 μm wires (McEnally *et al.*, 1997). The measured junction temperatures were converted to gas temperatures with a heat balance (radiation energy loss = convection energy gain) and the following parameters: Nusselt number = 2.26, junction diameter = 240 μm (measured with a microscope), temperature-dependent thermal conductivity data for air (Holman, 1986), and temperature-dependent type S thermocouple emissivities (Bradley, 1961). We estimate that the absolute error in the gas temperatures is less than 50K in soot-free flame regions. In soot-containing flame regions, particles rapidly deposit onto the junction, rendering the junction diameter and emissivity values listed above incorrect. Therefore the junction was cleaned before every measurement by retracting it into the oxidizing layer outside the flame, and the temperature was recorded quickly (0.75 seconds) after the junction was reinserted into the flame.

Soot volume fractions were measured with a new technique, thermocouple particle

densitometry (TPD), that was suggested by Eisner and Rosner (1985) and recently implemented by McEnally *et al.* (1997). A clean thermocouple was introduced into the flame and its junction temperature was recorded periodically for 200 seconds; the soot volume fraction was then determined by optimizing the agreement between the measured history and one calculated with the thermophoretic mass transfer formulation of Eisner and Rosner (1985). In the work cited above we demonstrated that TPD measurements agreed with soot volume fractions measured by the conventional technique of laser extinction in counterflow and coflowing nonpremixed flames. We developed TPD and employed it here because the combination of low soot volume fractions (<1 ppm) and short pathlengths (<5 mm) make laser extinction measurements difficult in methane coflowing flames (Garo *et al.*, 1986), (Shaddix *et al.*, 1994). With TPD, soot volume fractions can be easily measured down to at least 0.02 ppm by allowing sufficient time to pass for a measurable change in the junction temperature to occur. The technique also allows spatially-resolved measurements without tomographic reconstruction. The results have an absolute accuracy of $\pm$ 50% and a relative accuracy of $\pm$ 10%.

Recent experiments have shown that nonpremixed flames contain two kinds of soot particles: an early type that appears translucent when viewed under an electron microscope, and a later type that appears dark (Mergaridis and Dobbins, 1989). Similarly, two types of particles have been identified in premixed flames, where the early particles were shown to be transparent to visible light (d'Alessio *et al.*, 1992). Results from our laboratory suggest that soot volume fractions measured by TPD include both particle types, while laser extinction and laser-induced incandescence respond to only the dark particles (McEnally and Pfefferle, 1996), (Köylü *et al.*, 1996).

3.3 Species Measurements

Species concentrations were measured by extracting gases from the flames with a narrow-tip quartz microprobe, and analyzing them with on-line mass spectrometry. The sampling procedure and its performance are discussed in greater detail in McEnally and Pfefferle (1997) where it was concluded that the microprobe spatial resolution was roughly one millimeter, reactions in the microprobe tip have only a minor affect on the measured concentrations, and condensation/adsorption losses to the sample manifold walls were insignificant for biphenyl ($C_{12}H_{10}$; 154 AMU) and all lighter species. Following Puri (1992), we have equipped the probe with an oscillating sapphire fiber that extends through its orifice and grinds down any soot deposits that accumulate there. This prevents complete clogging of the orifice, enabling us to make measurements in particle-containing flame regions.

Most species were quantified with a custom-built photoionization/time-of-flight mass spectrometer (PTMS) that can simultaneously measure all C_3 and larger hydrocarbons (except propane and butane) with part-per-million detection limits (Bermudez and Pf-

efferle, 1995). This instrument generates ions via single-photon photoionization with a low-intensity vacuum-ultraviolet (118.2 nm) laser beam. The calibration factor relating ion signals to flame-gas concentrations was determined for benzene by flowing benzene/air mixtures of known-composition past a needle valve in the sample manifold. The same calibration factor was used for all other species for several reasons: independent calibrations would have been difficult since the detected species include room-temperature gases, liquids, and solids; several masses contain multiple isomers whose ratios could not be determined; and pure samples of several detected species could not be easily obtained. We estimate that the absolute concentrations of benzene are accurate to 30% while those of other species are accurate to within a factor of three. The primary quantity of interest here, the relative concentration of a given species with and without additives, is independent of the choice of calibration factors and accurate to 30%.

A commercial electron-impact/quadrupole mass spectrometer (EQMS; Leybold Inficon Transpector C100M) was used to measure methane, acetylene, and argon. The EQMS ionizes target gases with a fixed-energy 70 eV electron gun, which produces extensive ion fragmentation. Methane was measured with its CH_3^+ fragment-ion to avoid interferences from the O^+ fragment-ions of water and carbon dioxide, argon with its Ar^{++} ion to avoid interferences from $C_3H_4^+$ ions, and acetylene with its parent ion. The methane and acetylene concentrations were directly calibrated and are accurate to within 30%. However, ethylene fragment ions may account for up to 30% of the acetylene signal; ethylene and its $C_2H_3^+$ fragment-ion were completely obscured by nitrogen at all flame locations, so only an upper bound of 2000 ppm could be determined for its mole fraction.

The flowrate into the microprobe varied with flame position due to changes in the gas temperature and partial clogging of the orifice. To account for this, all PTMS and EQMS mass spectra were normalized with the EQMS argon signal by assuming that the argon concentration was uniform throughout the flame. As mentioned above, argon was added to the fuel so that its concentration was 1% in both reactant streams. At a height close to the burner surface, where soot clogging was insignificant, the radial temperature profile could be recovered from the raw argon signals, indicating that the constant-argon assumption is valid.

4. Numerical Method

Our goal is to obtain a discrete solution of the two-dimensional, elliptic, governing conservation equations for the temperature, gas-phase and soot mass fractions, velocities and vorticity on a two-dimensional mesh the initial nodes of which are formed by the intersection of the lines of the mesh $\mathcal{M}_r$

$$\mathcal{M}_r = \{0 = r_0 < r_1 < \ldots < r_i \ldots < r_{M_r} = R_O\}, \tag{4.1}$$

and the mesh $\mathcal{M}_z$

$$\mathcal{M}_z = \{0 = z_0 < z_1 < \ldots < z_j \ldots < z_{M_z} = Z\}. \tag{4.2}$$

Computationally, we combine a steady-state and a time-dependent solution method. A time-dependent approach is used to help obtain a converged numerical solution on an initial coarse grid. Grid points are then inserted adaptively and Newton's method is used to complete the problem. Specifically, the spatial operators in the governing partial differential equations are approximated by finite difference expressions. Diffusion terms are approximated by centered differences and convective terms by upwind approximations. With the difference equations written in residual form, we seek the solution U^* of the system of nonlinear equations

$$F(U) = 0. \tag{4.3}$$

For an initial solution estimate U^0 which is sufficiently close to U^*, the system of nonlinear equations in (4.3) can be solved by Newton's method. This leads to the iteration

$$J(U^n)(U^{n+1} - U^n) = -\lambda^n F(U^n), \quad n = 0, 1, 2, \ldots. \tag{4.4}$$

where $J(U^n) = \partial F(U^n)/\partial U$ is the Jacobian matrix and λ^n $(0 < \lambda \leq 1)$ is a damping parameter.

We point out that with the spatial discretizations used in forming (4.3), the Jacobian matrix in (4.4) can be written in block-nine-diagonal form. We form several columns of the Jacobian simultaneously using vector function evaluations and the Jacobian's given sparsity structure. The Newton equations are solved by a preconditioned BiCGSTAB iteration. The Newton iteration continues until the size of $\|U^{n+1} - U^n\|_2$ is reduced appropriately. Grid points of the two-dimensional mesh are determined by equidistributing positive weight functions over mesh intervals in both the r and z directions. During the pseudo-transient portion of the calculation, the size of the time steps is chosen by monitoring the local truncation error of the time discretization process. Due to the cost of forming the Jacobian matrices with detailed transport and finite rate chemical kinetics, a modified Newton method is implemented along with several theoretical estimates that determine when a new Jacobian should be reformed. These theoretical results help increase the overall efficiency of the algorithm (see Smooke *et al.*, 1990, 1996 for more details).

5. Results and Discussion

In this section we apply the model, solution procedure, and experimental methods discussed in Sections 2, 3 and 4 to a confined, axisymmetric, coflow, methane-air diffusion flame with the goal of helping to interpret flame structure and soot formation phenomena. Initial modeling results were compared with the experimental values for bulk flame parameters; i.e., flame height, peak flame temperatures, etc. Initially, flame height was overpredicted by the model by 15% and temperatures were underpredicted by about 100-150K. This lack of agreement was considered unacceptable. Upon analysis of both the

model and the experiment, it became apparent that conduction/radiation from the base of the flame to the burner exit tube in the experiment caused noticeable preheating of both inlet fuel and air streams. Calculations demonstrated that the flame height and local temperatures were significantly affected by these assumed inlet temperatures. Increasing the inlet temperatures from 300 to 420K (mass flow held constant) provided better agreement to the flame height and local temperatures (see later discussion). This approach, while not perfect, offers a tractable computational solution to a challenging problem. This increment is consistent with attempts to measure the temperature at the burner exit plane. The computational results demonstrate the importance of accurate specification of initial conditions, specifically temperature (and resultant effects on local velocities), on the numerical solutions.

Time-stepping from nearly converged solutions, led to the build up of large soot particles at the base of the flame in the wake of the burner lip. Several numerical experiments demonstrated that the source of this build-up was thermophoresis. Small soot particles generated inside the flame front at the lip were driven inside this small wake with large temperature gradients. Neither surface growth nor inception enhanced the soot levels in these regions. Coalescence over long times led to the formation of large particles which were not flushed away by the flow in this wake region, yet were continually fed as time elapsed by small particles near the flame front. In heavier sooting, co-flow flames, such build-up with time has been observed experimentally as evidenced by the occasional requirement to shut down and clean particulates from the exit tube (Santoro, 1996). This build-up is not observed experimentally for the lightly sooting methane flames. This process has been suppressed in the model by setting the thermophoretic velocity to zero below 750K. This does not cause any noticeable change of predicted soot levels in the remainder of the flow field.

The chemical kinetic mechanism used in this work was derived from GRIMech 2.11 with its recommended thermodynamics (Bowman *et al.*, 1995). All reactions related to NO formation and other odd nitrogen species were stripped from the set. In addition, a series of reactions related to the formation and oxidation of benzene, and related species, were included (see Table 1 of Hall *et al.*, 1997). The dominate ring forming reaction was propargyl recombination. This is consistent with material balance analyses of benzene formation mechanisms based on the experimental species concentrations. The burner fuel tube had an inner radius of R_I=0.5556 cm with a wall thickness of 0.0794 cm. The radius of the coflow was $R_O = 4.7625$ cm. Conditions at the fuel and oxidizer jet inlets were such that

$$v_F = 5.52\text{cm/sec}, \quad v_{OX} = 12.54\text{cm/sec}, \tag{5.1}$$

$$T_F = 420\text{K}, \quad T_{OX} = 420\text{K}. \tag{5.2}$$

All calculations were performed on an IBM RS/6000 Model 590 computer. In the com-

putations to be presented 12 soot size classes were included in the model. Starting from a converged solution for a methane-air flame without the sectional equations, we typically obtained converged solutions for the complete gas-soot problem in several hours of computer time.

Temperature Predictions

Examination of the curves in Figure 2 demonstrates that the model predicts the general shape and structure of the flame (location of peak flame temperatures, etc.) reasonably well. Temperature is perhaps the most important of the flame parameters as temperature has a direct influence on virtually all the other flame properties (e.g., flame height and width, species concentrations, soot, etc.) A more careful comparison of the profiles in Fig. 2 shows that the model underpredicts the experimental measurements along the centerline by about 100K at all heights within the flame. In addition, while the location and value of the peak temperature are reasonably well described up to about a height of z = 2 cm, temperatures are overpredicted at the outside edge (i.e., predicted temperatures do not fall off as rapidly as the data with increasing radius). Finally, the experimental flame closes to the centerline (at $z \approx 40$ mm) more rapidly than does the computed flame. The computed low centerline temperatures and the slightly delayed contraction of the flame tip, presumably are very much related to the inability to match accurately the flame height. These deficiencies in the model are attributable, at least partly, to the uncertainties in the inlet boundary conditions. As argued below, these limitations of the computed temperature field have a direct implication on the prediction of gas species and particulates. One possible explanation of the low temperatures along the centerline is the lack of inclusion in the model of absorption by methane of energy radiated from the flame front.

Prediction of Species

Figure 3 shows comparison of the methane profiles as a function of radius at several heights above the burner. Again the general features of the radial profiles, for several heights in the flame are reproduced well by the model. Typically, methane is overpredicted by a factor of two along the centerline. This result is consistent with the low temperatures from the computed flame along the centerline. Alternatively, the model overpredicts the fall-off with increasing radius, most noticeably at the lowest height, z = 1.0 cm. This accentuated fall-off is undoubtedly a direct result of the higher predicted temperatures in the wings of the flame, and hence more rapid chemistry. The factor of three overprediction at z = 2.5 cm on the centerline, is a consequence of the (experimental) rapid decrease in methane concentration in this region of the flame, i.e., the flame tip, and the inability of matching the flame height exactly.

Similar comments can be made in regard to the acetylene and benzene profiles. In these cases, however, centerline values are underpredicted, presumably because methane

decomposition is suppressed at the low predicted temperatures along the centerline, as discussed above. Not surprisingly, the relatively small underprediction of acetylene (factor of two) along the centerline, leads to a larger deficit in the computed benzene profiles (a factor of three) on the centerline. Since these species are key to the growth and inception of particulates, the combination of their low values as well as the low temperature predictions along the centerline must lead commensurately to low predictions of soot in these regions. Of importance, however, is that the concentrations of these species, as well as temperatures, are better described in the flame front region most critical to inception and growth. Until a satisfactory solution is found to predict more accurately centerline temperatures, quantitative predictions of formation of the translucent droplets/particles along the centerline, such as observed by Megaridis and Dobbins (1989) will likely not be achieved.

Soot Particulates

Figure 6 depicts the computed and experimental values of soot volume fraction (cm^3 soot/cm^3 gas) as a function of radius at z = 1.75, 2.0. 2.25, 2.5, 2.75, and 3.0 cm. As for the species profiles, the computations describe the general features of the soot field. Peak soot volume fractions are underpredicted by a factor of about three, however the shape and trend of the shift of the volume fraction profile is reproduced well. The experimental peak values collapse to the centerline more rapidly, as discussed above, because of the difference in the computed flame height. Centerline values are significantly underpredicted (order of magnitude) because of the combination of predicted low temperatures (100K), low acetylene (factor of two) and low benzene (factor of three). It is reasonable to assume that should these bulk flame properties be more accurately modeled, our ability to attain quantitative predictions of the soot field would be enhanced dramatically.

Predicted soot volume fractions are strongly dependent on predicted acetylene profiles, which generally are dependent upon the kinetics supplied by GRIMech, but also are depressed when scrubbing is included in the calculations. Without the added chemical mechanisms and soot formation steps, predicted levels of acetylene are very close to the experimental values, depending on the flame location. Measured peak acetylene concentrations are about 12,000 ppm. The measured peak soot volume fractions are 4.7×10^{-7} which is approximately equivalent to 4000 ppm acetylene. Hence, suppression of the acetylene peak by the soot formation is expected and is observed in these calculations – even in these lightly sooting flames. The reduced acetylene levels, in turn, suppress the levels of soot predictions, since both the inception and the growth processes are strongly dependent on the acetylene concentration. Predicted acetylene concentrations more consistent with experimental results would result in more favorable agreement between predicted and measured soot volume fraction in Figure 6. Soot volume fraction predictions based on this growth model have some residual sensitivity to the number of size classes at the value of 12 employed, which was the largest number permissible given the number of species and

grid nodes relative to available computer memory. While size class convergence will have to be addressed ultimately, factors such as inlet/boundary conditions and flame chemistry may have a much greater influence on the accuracy of the solution and its ability to reproduce bulk flame parameters (specifically, temperature). As will be seen, calculations with another soot growth model show much more rapid convergence with the number of size classes.

2D Solutions

In Figures 7-11 we illustrate contour plots of the same variables plotted in Figures 2-6. The two-dimensional, color contour of computed temperatures in Fig. 7 clearly shows the peak temperature regions in the flame front. The highest temperatures within the flame are not at the flame peak, but in the outer annulus regions. Peak height can be inferred from these profiles by locating the point at which the temperature peaks on the centerline, for example. The contour plot of methane shows a very dramatic loss of methane very low in the flame. This extremely rapid decay is principally due to rapid diffusion of molecular nitrogen to the centerline, rather than the reaction of methane. (In fact, it is exactly this rapid diffusional process that has led to confusion in the literature when attempts have been made to separate dilution from temperature effects and their relative importance to soot formation.). Predicted peak acetylene and benzene profiles occur on the centerline about a centimeter below the flame tip near $z = 2.8$ cm. Benzene seems to decay more rapidly above this location than does acetylene. The rapid decay in the acetylene appears more closely aligned with the flame tip. Alternatively, the earlier decay in the benzene is linked to the soot inception process, which attains its peak rates in this region of the flame.

Soot Growth and Inception

Figures 12-14 contain contour plots of the net soot production, soot inception and soot oxidation, respectively. Comparison of the net soot production (Figure 12) with inception (Figure 13) shows that the growth region is surface- rather than inception-dominated. Higher in the flame net growth gives way to oxidation as the particles burn out (Figure 14). The surface growth contours are a convolution of the temperature and acetylene contours (Figures 7 and 9), strongly reflecting the annular shape of the temperature profile, while inception is an image of the benzene contour of Figure 10.

Soot Oxidation

The rates of oxidation of the particulates by OH and by O_2 are shown in Figure 14. Rate data are plotted on the same scale in the two figures to readily assess the relative importance of the two oxidants. Maximum oxidation rates by O_2 clearly are about a factor of 5 to 10 below those by OH. Oxidation by O_2 occurs in two separate regions of the flow. Near the base of the flame, O_2 diffuses underneath the flame and contributes to

soot oxidation on the fuel-rich side of the flame until the O_2 concentration is exhausted. O_2 also contributes to soot oxidation in the post flame region, but only competes with oxidation by OH high in the flame. The hydroxyl radical is clearly the dominant oxidizing species in this flame. Peak oxidation rates occur in the conventional wing tips of the flame and high oxidation rates continue to the centerline. These results (i.e., the strong dominance of OH as the principal oxidizing species) are wholly consistent with those of Garo, *et al.* (1990) who analyzed the dynamics of a methane-air coflow diffusion air and more recently of Kennedy, *et al.* (1996) in their detailed modeling of an ethylene coflow diffusion flame. Together, the present and prior results cast doubts on the validity of models which neglect the role of oxidation by OH in coflow flames (for example, Kaplan, *et al.* (1996) and Sivanthanu and Gore (1994)). The cause of the high importance of OH as the principal oxidizing species is its high superequilibrium level in the flame front. (See discussion below.)

In this study, the soot field has been modeled using a constant 0.13 collision frequency for reaction after Neoh, *et al.* (1981). In the Kennedy, *et al.* (1996) study, this reaction efficiency was varied linearly from 0.05 low in the flame to 0.2 in the tip flame region, to assist in matching soot profiles. In addition, Garo, *et al.* interpreted their data to be consistent with a varying collision frequency with height in the flame. While it is apparent that such methods could assist matching the experimental and modeling profiles of soot, we have not yet adopted this approach.

Superequilibrium OH

Smooké, et al. (1992) have computed superequilibrium levels of hydroxyl in methane air coflow flames. Santoro and coworkers have measured OH concentrations and temperatures in ethylene flames and found these radical concentrations to be effected by the level of soot in the flame. Higher soot levels decreased OH concentrations due to scrubbing. Such effects were not noticeable in this study, presumably due to the much lower concentrations of soot. The OH measured by Puri, Santoro and Smyth (1994) were described to be at superequilibrium levels. Logically, these superequilibrium levels are the source of the artificial requirement to augment the reaction efficiency of OH and soot. To examine levels of superequilibrium, calculated OH (referred to here as "flame OH" have been compared to the equilibrium levels of OH based on 1) the local temperature (constant temperature calculation), 2) the full equilibrium (constant enthalpy calculation), and 3) a partial equilibrium assumption based on

$$O_2 + H_2 \leftrightarrow 2OH$$

and the local flame temperature. The ratio of this flame OH to the equilibrium levels are plotted in Figure 15 as a function of the radius at $z = 4.01$ cm. The maximum soot oxidation rate occurs at this height at a radius of about 0.31 cm. At this radius, the OH attains concentrations a factor about 10 above the equilibrium value, thus validating

further the existence of large OH superequilibrium concentrations as an important contributor to the destruction/burnout of soot. Chemical systems which cannot support such high superequilibrium levels may be more prone to soot emissions. The partial equilibrium assumption (assuming knowledge of the H2, O2 concentrations and temperature) provides a much better estimate of hydroxyl, at least through the flame front region where soot is being oxidized.

Partcle Size

Figure 16 shows the evolution of soot particle size distribution in space as a result of surface growth and coalescence. The sectional mass boundaries have been placed linearly on a logarithmic scale. Peak soot mass concentration occurs in size class nine, whose mass-weighted mean diameter is about 48 nm, which should be considered an estimate. A larger number of sections than that employed here would be required to obtain an accurate average particle size. This average size is clearly larger than typical determinations of 20-30 nm in laboratory flames and suggests some refinements in our soot model are still required. The fact that the suspended mass in the highest class remains relatively small shows that the upper boundary of the particle size domain has been set high enough to avoid unphysical accumulation of particles in the highest size class. The smallest size classes are observed to disappear rapidly in the post flame zone, while a portion of the largest particles survive to the end of the computational domain.

Particle size distribution within the flame can also be visualized from Figures 17 and 18 in which the mass fractions of each of the 12 soot mass classes (mc) are plotted as a function of radial distance for heights of 1 and 3 centimeters. Low in the flame, the sixth soot class contains the peak mass fraction and at 3 cm (just before the onset of rapid soot oidation by OH inside the flame front), the maximum occurs in the ninth class. At this higher position, substantial soot is found also near the centerline of the flame. However, the average particle for this "centerline" soot is much smaller than that just inside the flame front, a result qualitatively consistent with the results by Megaridis and Dobbins (1989). Since benzene concentrations (Figure 10) and hence inception rates (see Figure 13) are peaking in this region of the flow, the particles depicted on the centerline are likely formed along or near to the centerline rather than transported via thermophoresis from the flame front to this centerline region.

Radiation Effects

While it might be expected that thermal radiation effects would be small in a lightly sooting flame like that investigated here, simulations in which the radiative loss term, Eq. 2.21, is set equal to zero show that radiation effects are significant. Without radiation, predicted peak temperatures are 122K higher, a change large enough to affect predicted soot levels and species concentrations. Predicted peak volume fractions increase by a factor of three, with peak acetylene and benezene levels increasing by 45% and 22%,

respectively. The significance of thermal radiation in this lightly sooting flame arises from residence times that are relatively long compared to those for counterflow diffusion flames, in which radiation effects are significant only for extremely low strain rates (Garcia, et al., 1996). With the relatively low values of soot concentration and the fact that the soot does not occupy the peak temperature regions, the thermal radiation here is actually dominated by water vapor and carbon dioxide, with the 4.3 micron band of CO_2 the dominant contributor. The physical dimensions of this flame are sufficiently small that self-absorption or optical thickness corrections should be minimal.

Variations of Inlet Gas Temperatures

Early modeling efforts with the inlet gas temperatures at 298K resulted in a flame height about 15% higher than the experimental value. In addition, predicted peak flame temperatures were about 125K below the experimental value. Since soot volume fractions are a strong function of temperatures, these low predicted temperatures substantially limited our ability to predict accurately the soot concentrations. Local temperatures in the unburned gases just above the burner lip were measured to be much higher than 298K, presumably due to radiation preheating and conduction. Accurate treatment of this problem would require knowledge not only of temperatures, but also of local velocities at each location in the burner inlet. To 1) analyze this problem in a simplified manner, 2) provide information relative to a sensitivity study, and 3) elevate the peak flame temperatures to values closer to the experimental levels, calculations were performed for elevated temperatures in the entire fuel flow, the entire air flow, or both streams. For each case, the mass flows per unit area were held constant and hence velocities increased with higher temperatures.

Table 1 compares the peak soot volume fractions and the peak flame temperatures obtained for several solutions at inlet temperatures ranging from 298 to 500K. An examination of these numbers demonstrates that an increase in the air temperature has a much more dramatic effect on both the peak flame temperature and volume fraction than comparable changes in the fuel temperature. Presumably, this effect is due to the higher mass weighted enthalpy content of air under stoichiometric conditions. The higher flame temperatures which arise from the elevated inlet air temperatures lead to a proportionally greater increase in the soot generation.

Comparisons to Fairweather, et al. model

Finally, the model was rerun with the inception and surface growth model of Fairweather *et al.* (1992). Soot volume fraction, net soot production, inception, and oxidation are illustrated in Figures 19-22. In this model, which has been applied to ethylene- and acetylene-fuelled coflow flames (Kennedy, 1996; Sivathanu and Gore, 1994), both inception and surface growth are proportional to acetylene concentration. Its inception and surface growth rates are used here in the polydisperse, sectional representation rather than the

monodisperse representation of the original model. Additionally, oxidation by OH, not included in Fairweather, et al. (1992), has been accounted for in this implementation.

TABLE 1

Effect of Fuel and Oxidizer Inlet Temperatures on
Peak Soot Volume Fraction and Peak Flame Temperature

T_f/T_{ox}	f_v	T_{max}
298/298	3.30×10^{-8}	1942 K
298/420	8.71×10^{-8}	1976 K
298/500	1.43×10^{-7}	2000K
420/298	4.67×10^{-8}	1948 K
500/298	5.87×10^{-8}	1954 K
420/420	1.14×10^{-7}	1984 K
500/500	$x.xx \times 10^{-7}$	xx K

The predicted soot concentrations (Figure 19) are seen to be slightly larger than those predicted with the base model. Given the previously discussed uncertainties associated with the chemical mechanism and burner boundary conditions, however, no judgements about the merits of this model vis-a-vis the base model are warranted. Inception is more significant in the Fairweather, et al. (1992) model (compare Figures 21 and 13), and this seems to give calculations using it much less sensitivity to the number of soot sections employed. Predicted soot volume fractions using five and twelve sections were not significantly different. The spatial distribution of inception in the two models is very different, as Figures 13 and 21 show. The Fairweather, et al. (1992) model has an inception profile that is strongly annular, reflecting, like the surface growth, the convolution of temperature and acetylene profiles. Oxidation in this latter model is also dominated by OH, as Figure 22 illustrates.

Summary of Differences Betweeen Model and Experiment

Differences between our predictions and the experimental data include: overprediction of flame height, underprediction of peak temperatures, too slow decay of methane along the centerline and a slow decay of temperature in the wings of the flame. In addition, the model significantly underpredicts the peak soot volume fractions in the flame and tends to overpredict particle size. Much of the differences can be directly linked to the inadequate prediction of the temperature field and the flame height. Contrasting these results are the very good agreement of the temperature field and flame height obtained in

the modeling of a methane coflow flame in a study of NO formation Smooke, et al. (1997). Principal differences between this previous study and that of the present investigation includes dilution of the fuel, higher flow rates, and a lifted flame. We believe the most likely of these parameters affecting uncertainties in the present study is the inability of our code to properly model the attachment (i.e., close proximity) of the flame to the burner lip and all of its attendant effects. Other possible contributors to this error include uncertainties in the kinetics. For example, using this kinetic mechanism (hydrocarbon portion of GRIMech 2.11) the extinction limit in a counterflow methane-air diffusion flame is significantly overpredicted (380 cm^{-1} experiments vs. predictions of 620 cm^{-1}). We note also that there are still fundamental uncertainties in soot growth modeling such as the rates of inception, surface growth, and coalescence of very small particles. For example, a 50% increase in the surface growth rate constant results in a predicted soot volume fraction in much better agreement with data. Until the temperature field is more accurately described, it is difficult to offer quantitative arguements about the accuracy (or lack thereof) of our soot model. Nevertheless, the qualitative results and conclusions should still be valid.

6. Conclusions

The axisymmetric laminar diffusion flame provides a natural environment in which one can investigate the interaction of soot formation with detailed gas-phase chemistry in a multidimensional system. In this paper we have compared experimental measurements of the temperature, soot volume fraction and selected species from an axisymmetric, laminar, methane-air diffusion flame with computational results obtained by generalizing the sectional model presented in Hall et al. (1997) to a coflow model. This work represents the first time that a detailed chemistry/complex transport flame model has been coupled to a polydisperse soot growth analysis in which the scrubbing of gaseous species and both gas and particle radiation are included. The detailed chemistry includes species up through benzene and includes a steady-state model for the formation of polyaromatic hydrocarbons to simulate soot inception. Soot volume fractions calculated from this model using either our growth inception formulation or that by Fairweather et al. (1992) underpredicted the experimental values by about a factor of three. These low values, we believe, are directly attributable to the inability to reproduce accurately bulk flame properties. Specifically, low temperatures lead to underpredictions of critical growth species such as acetylene and benzene. Principal differences between the model and the experiments, we believe, are attributable to the inaccuracies in the predicted temperature field which, in turn, may be partially due to inadequate modeling of flame attachment at the burner lip.

Acknowledgments

This work has been supported in part by the Air Force Office of Scientific Research

under contract F49620-94-C-0059 and the United States Department of Energy, Office of Basic Energy Sciences. The encouragement of Julian Tishkoff and discussions with R. J. Santoro (Penn State University), R. A. Dobbins (Brown University) and M. A. Tanoff (Yale University) are gratefully acknowledged. The assistance of R. R. Dobbins (Yale University) was essential in the preparation of the figures.

References

Axelbaum, R.L., Flower, W.L., and Law, C.K., "Dilution and Temperature Effects of Inert Addition on Soot Formation in Counterflow Diffusion Flames," *Combust. Sci. Tech.*, **61**, p. 51 (1988).

Bermudez, G., and Pfefferle, L.D., "Laser Ionization Time-of-Flight Mass Spectrometry Combined with Residual Gas Analysis for the Investigation of Moderate Temperature Benzene Oxidation," *Combust. Flame*, **100**, p. 41 (1995).

Bowman, C.T., Hanson, R.K., Davidson, D.F., Gardiner, Jr., W.C. Lissianski, V., Smith, G.P., Golden, D.M., Frenklach, M., Wang, H., and Goldenberg, M., *GRI-Mech version 2.11*, http://www.gri.org (1995).

Bradley, D., and Entwistle, A.G., "Determination of the Emissivity, for Total Radiation, of Small Diameter Platinum-10% Rhodium Wires in the Temperature Range 600–1450°C," *British Journal of Applied Physics*, **12**, p. 708 (1961).

Colket, M.B., and Hall, R.J., "Successes and Uncertainties in Modeling Soot Formation in Laminar, Premixed Flames," in *Soot Formation in Combustion, Mechanisms and Models*, H. Bockhorn, Ed., Springer Series in Chemical Physics **59**, Springer-Verlag, p. 442 (1994).

Colket, M.B., and Hall, R.J., "Mechanisms Controlling Soot Formation in Diffusion Flames," Annual Report for AFOSR Contract F49620-94-C-0059, August, 1995; Hall, R.J., to be published 1996.

Curtiss, C.F., and Hirschfelder, J.O., "Transport Properties of Multicomponent Gas Mixtures," *J. Chem. Phys.*, **17**, p. 550 (1949).

D'Alessio, A., D'Anna, A., D'Orsi, A., Minutolo, P., Barbella, R., and Ciajolo, A., "Precursor Formation and Soot Inception in Premixed Ethylene Flames," *Twenty-Fourth Symposium (International) on Combustion*, The Combustion Institute, Pittsburgh, 1992, p. 973.

Eisner, A.D., and Rosner, D.E., "Experimental Studies of Soot Particle Thermophoresis in Nonisothermal Combustion Gases Using Thermocouple Response Techniques," *Combust. Flame*, **61**, p. 153 (1985).

Ern, A., Douglas, C.C., and Smooke, M.D., "Detailed Chemistry Modeling of Laminar Diffusion Flames on Parallel Computers," *Int. J. of Supercomputer Appl.*, **9**, p. 167 (1995).

Fairweather, M., Jones, W.P., and Lindstedt, R.P., "Predictions of Radiative Transfer from a Turbulent Reacting Jet in a Cross-Wind," *Combust. Flame*, **89**, p. 45 (1992).

Garcia, C., Tanoff, M. A., Smooke, M. D., and Hall, R. J., "Application of a Non-Optically Thin Radiation Model to the Study of Low-Strain Laminar Counterflow Flames," Eastern States Meeting of the Combustion Institute, Hilton Head, December, 1996.

Garo, A., Lahaye, J., and Prado, G., "Mechanisms of Formation and Destruction of Soot Particles in a Laminar Methane-Air Diffusion Flame," *Twenty-First Symposium (International) on Combustion*, The Combustion Institute, Pittsburgh, 1986, p. 1023.

Garo, A., Prado, G., and Lahaye, J., "Chemical Aspects of Soot Particles Oxidation in a Laminar Methane-Air Diffusion Flame," *Combust. Flame*, **79**, p. 226 (1990).

Gelbard, F., and Seinfeld, J.H., "Simulation of Multicomponent Aerosol Dynamics," *J. Coll. Int. Sci.*, **78**, p. 485 (1980).

Giovangigli, V. and Darabiha, N., "Vector Computers and Complex Chemistry Combustion," in *Proceedings of the Conference on Mathematical Modeling in Combustion*, Lyon, France, NATO ASI Series (1987).

Hall, R.J., "The Radiative Source Term for Plane-Parallel Layers of Reacting Combustion Gases," *J. Quant. Spec. Rad. Tran.*, **49**, p. 517 (1993).

Hall, R.J., "Radiative Dissipation in Planar Gas-Soot Mixtures," *J. Quant. Spec. Rad. Tran.*, **51**, p. 635 (1994).

Hall, R.J., Smooke, M.D., and Colket, M.B., "Predictions of Soot Dynamics in Opposed Jet Diffusion Flames," in *Physical and Chemical Aspects of Combustion: A Tribute to Irvin Glassman*, ed. by R.F. Sawyer and F.L. Dryer, Combustion Science and Technology Book Series, Gordon and Breach, (1997).

Harris, S.J., and Weiner, A.M., "Surface Growth of Soot Particles in Premixed Ethylene/Air Flames," *Combust. Sci. Tech.*, **31**, p. 155 (1983).

Harris, S.J., Weiner, A.M., and Blint, R.J., "Formation of Small Aromatic Molecules in a Sooting Ethylene Flame," *Combust. Flame*, **72**, p. 91 (1988).

Holman, J.P. Heat Transfer. McGraw-Hill Book Company, New York, 1986, p. 643.

Hura, H.S. and Glassman, I., "Soot Formation in Diffusion Flames of Fuel/Oxygen Mixtures," *Twenty-Second Symposium (International) on Combustion*, The Combustion Institute, Pittsburgh, 1988, p. 371.

Kaplan, C.R., Shaddix, C.R., and Smyth, K.C., "Computations of Enhanced Soot Production in Time-Varying CH_4/Air Diffusion Flames," *Combust. Flame*, **106**, p. 392 (1996).

Kennedy, I.M., Rapp, D.R., Santoro, R.J., and Yam, C., "Modeling and Measurements of Soot and Species in a Laminar Diffusion Flame," *Combust. Flame*, **107**, p. 386 (1996).

Kennedy, I.M., Kollmann, W., and Chen, J.Y., "Model for Soot Formation in a Laminar Diffusion Flame," *Combust. Flame*, **81**, p. 73 (1990).

Köylü, Ü.Ö., McEnally, C.S., Rosner, D.E., and Pfefferle, L.D., "Simultaneous Measurements of Soot Volume Fraction and Particle Size/Microstructure in Flames Using a Thermophoretic Sampling Technique," *Combust. Flame*, to be published in 1997.

Leung, K.M., Lindstedt, R.P. and Jones, W.P., "A Simplified Reaction Mechanism for Soot Formation in Nonpremixed Flames," *Combust. Flame*, **87**, p. 289 (1991).

Lindstedt, R.P., "Simplified Soot Nucleation and Surface Growth Steps for Non-premixed Flames," in *Soot Formation in Combustion, Mechanisms and Models*, H. Bockhorn, Ed., Springer Series in Chemical Physics **59**, Springer-Verlag, p. 417 (1994).

McEnally, C.S., and Pfefferle, L.D., "Aromatic and Linear Hydrocarbon Concentration Measurements in a Non-Premixed Flame," *Combust. Sci. Tech.*, **116–117**, p. 183 (1996).

McEnally, C.S., Köylü, Ü.Ö., Pfefferle, L.D., and Rosner, D.E., "Soot Volume Fraction and Temperature Measurements in Laminar Non-Premixed Flames Using Thermocouples," *Combust. Flame*, to be published in 1997.

Megaridis, C.M., and Dobbins, R.A., "Comparison of Soot Growth and Oxidation in Smoking and Non-Smoking Ethylene Diffusion Flames," *Combust. Sci. Tech*, **66**, p. 1 (1989).

Neoh, K.G., Howard, J.B., and Sarofim, A.F., in *Particulate Carbon: Formation During Combustion*, D.C. Seigla and G.W. Smith, Eds., Plenum, New York, p. 261 (1981).

Puri, R. *The Interaction of Soot Particles and Carbon Monoxide in Laminar Diffusion Flames.* Ph.D. thesis, The Pennsylvania State University, 1992.

Puri, R., Santoro, R. J., and Smyth, K. C., *The Oxidation of Soot and Carbon Monoxide in Hydrocarbon Diffusion Flames*, *Combust. Flame*, **97**, p. 125 (1994).

Santoro, R.J., personal communication (1996).

Shaddix, C.R., Harrington, J.E., and Smyth, K.C., "Quantitative Measurements of Enhanced Soot Production in a Flickering Methane/Air Diffusion Flame," *Combust. Flame*, **99**, p. 723 (1994).

Sivathanu, Y.R., and Gore, J.P., "Coupled Radiation and Soot Kinetics Calculations in Laminar Acetylene/Air Diffusion Flames," *Combust. Flame*, **97**, p. 161 (1994).

Smooke, M.D., Mitchell, R.E. and Keyes, D.E., "Numerical Solution of Axisymmetric Laminar Diffusion Flames," *Combust. Sci. Tech.*, **67**, p. 85 (1989).

Smooke, M. D., Lin, P., Lam, J. K., and Long, M. B., "Computational and Experimental Study of a Laminar Axisymmetric Methane-Air Diffusion Flame," *Twenty-Third Symposium (International) on Combustion*, The Combustion Institute, Pittsburgh, 1990, p. 575.

Smooke, M.D., Xu, Y., Zurn, R.M., Lin, P., Frank, J.H. and Long, M.B., "Computational and Experimental Study of OH and CH Radicals in Axisymmetric Laminar Diffusion Flames," *Twenty-Fourth Symposium (International) on Combustion*, The Combustion Institute, Pittsburgh, 1992, p. 813.

Smooke, M.D., Ern, A., Tanoff, M.A., Valdati, B.A., Mohammed, R.K., Marran, D.F. and Long, M.B., "Computational and Experimental Study of NO in an Axisymmetric Laminar Diffusion Flame," *Twenty-Sixth Symposium (International) on Combustion*, The Combustion Institute, Pittsburgh, 1996, p. 2161.

Smooke, M.D., Hall, R.J. and Colket, M.B., "Application of Continuation Methods to Soot Formation in Counterflow Diffusion Flames," submitted to *Comb. Theory and Modelling* (1997).

Sunderland, P.B., and Faeth, G.M., "Soot Formation in Hydrocarbon/Air Laminar Jet Diffusion Flames," *Combust. Flame*, **105**, p. 132 (1996).

Vandsburger, U., Kennedy, I.M., and Glassman, I., "Sooting Counter-Flow Diffusion Flames with Varying Velocity Gradients," *Twentieth Symposium (International) on Combustion*, The Combustion Institute, Pittsburgh, 1984, p. 1105.

Vandsburger, U., Kennedy, I., and Glassman, I., "Sooting Counterflow Diffusion Flames with Varying Oxygen Index," *Combust. Sci. Tech.*, **39**, p. 263 (1984).

Wang, H., Du, D.X., Sung, C.J., and Law, C.K., "Experiments and Numerical Simulation on Soot Formation in Opposed-Jet Ethylene Diffusion Flames," *Twenty-Sixth Symposium (International) on Combustion*, The Combustion Institute, Pittsburgh, 1996, p. 2359.

Xu, Y., Smooke, M.D., Lin, P. and Long, M.B., "Primitive Variable Modeling of Multidimensional Laminar Flames," *Combust. Sci. Tech.*, **90**, p. 289 (1993).

Figure Captions

Figure 1 Schematic of the burner configuration.

Figure 2 Profiles of the computed and measured temperature profiles at various heights in the flame.

Figure 3 Profiles of the computed and measured methane profiles at various heights in the flame.

Figure 4 Profiles of the computed and measured acetylene profiles at various heights in the flame.

Figure 5 Profiles of the computed and measured benzene profiles at various heights in the flame.

Figure 6 Profiles of the computed and measured soot volume fraction profiles at various heights in the flame.

Figure 7 Temperature isotherms of the computational model as a function of the radial and axial coordinates.

Figure 8 Methane isopleths of the computational model as a function of the radial and axial coordinates.

Figure 9 Acetylene isopleths of the computational model as a function of the radial and axial coordinates.

Figure 10 Benzene isopleths of the computational model as a function of the radial and axial coordinates.

Figure 11 Soot volume fraction isopleths of the computational model as a function of the radial and axial coordinates.

Figure 12 Net soot production isopleths of the computational model as a function of the radial and axial coordinates.

Figure 13 Comparison of soot inception due to acetylene and benzene as a function of the radial and axial coordinates; rate of equation 2.1 versus that of equation 2.2.

Figure 14 Comparison of soot oxidation due to oxygen and OH as a function of the radial and axial coordinates.

Figure 15 Profiles of the ratio of the OH mole fraction to the equilibrium levels as a function of the radial coordinate at $z = 4.01$ cm.

Figure 16 Illustration of the evolution of soot particle size distribution in space as a result of surface growth and coalescence. The sectional mass boundaries have been placed linearly on a logarithmic scale. Peak soot mass concentration occurs in size class nine, whose mass-weighted mean diameter is about 48 nm.

Figure 17 Contributions of the Soot Mass Classes to the Total Soot Volume Fraction at z=1 cm.

Figure 18 Contributions of the Soot Mass Classes to the Total Soot Volume Fraction at z=3 cm.

Figure 19 Soot volume fraction isopleths of the Fairweather *et al.* (1992) model as a function of the radial and axial coordinates.

Figure 20 Net soot production isopleths of the Fairweather *et al.* (1992) model as a function of the radial and axial coordinates.

Figure 21 Soot inception isopleths of the Fairweather *et al.* (1992) model as a function of the radial and axial coordinates.

Figure 22 Comparison of soot oxidation due to oxygen and OH as a function of the radial and axial coordinates for the Fairweather *et al.* (1992) model.

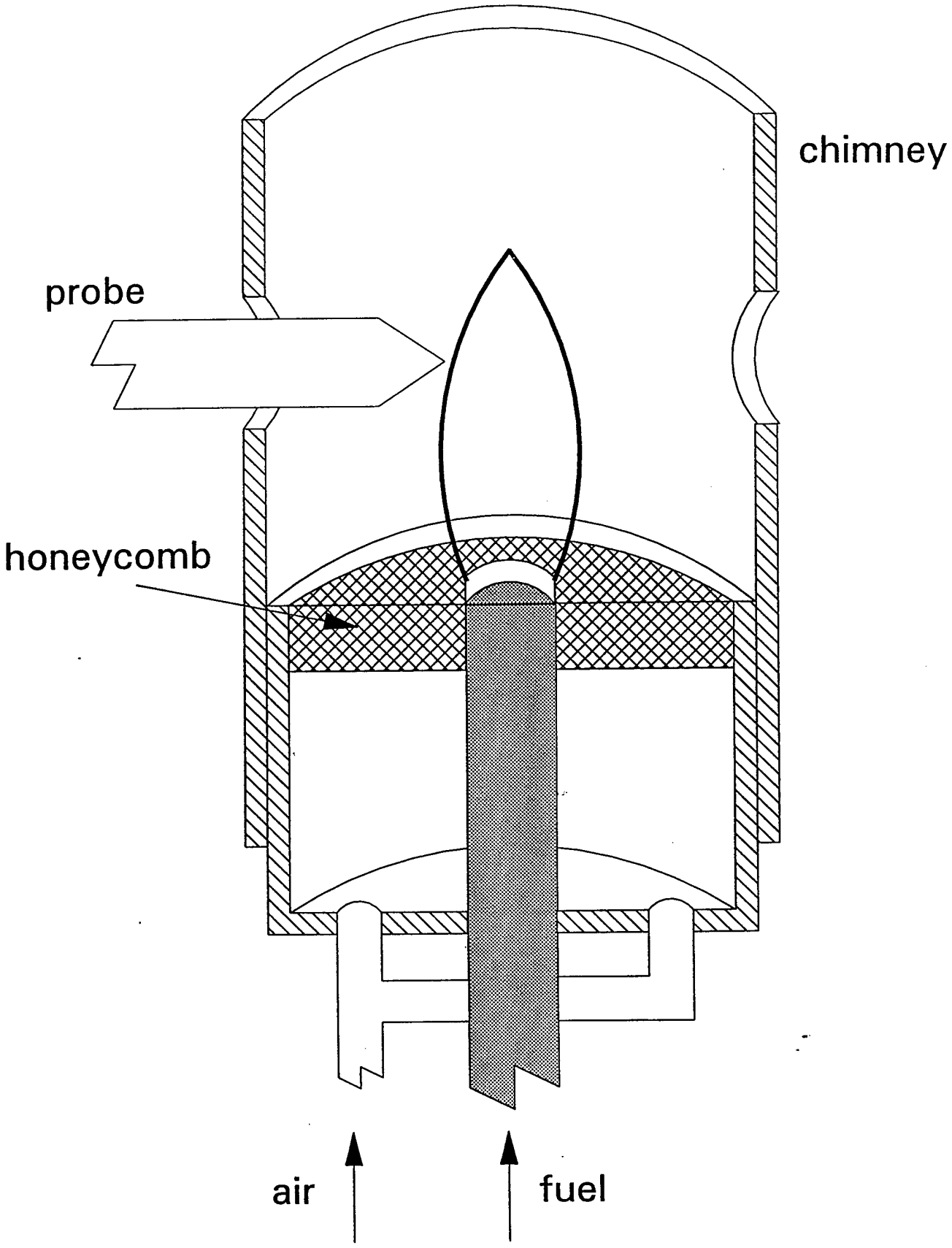

Figure 1

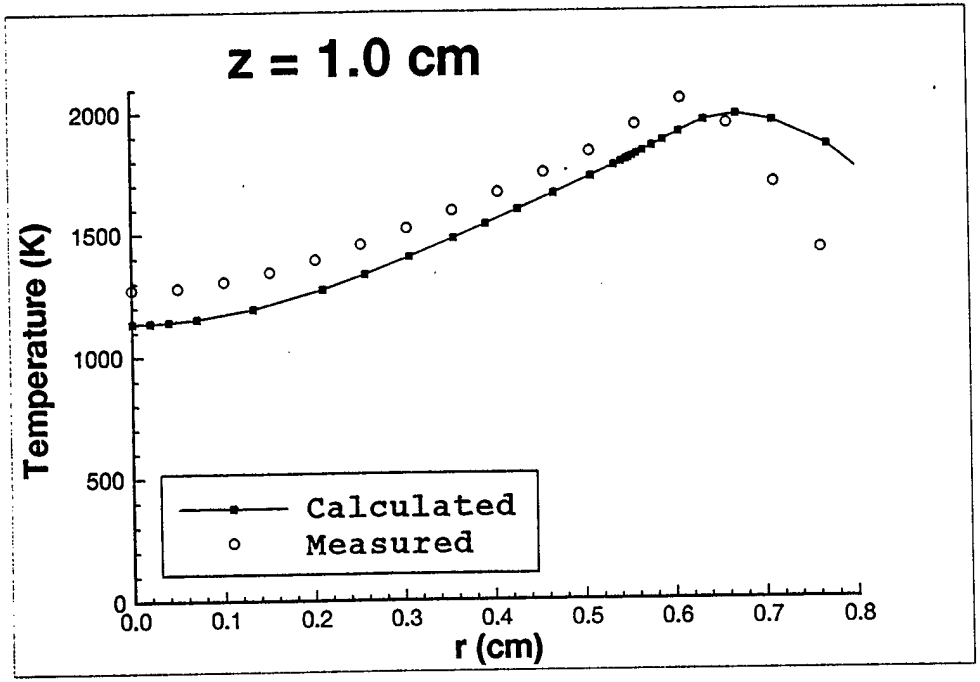
z = 1.0 cm
Temperature (K)
r (cm)
Calculated
Measured

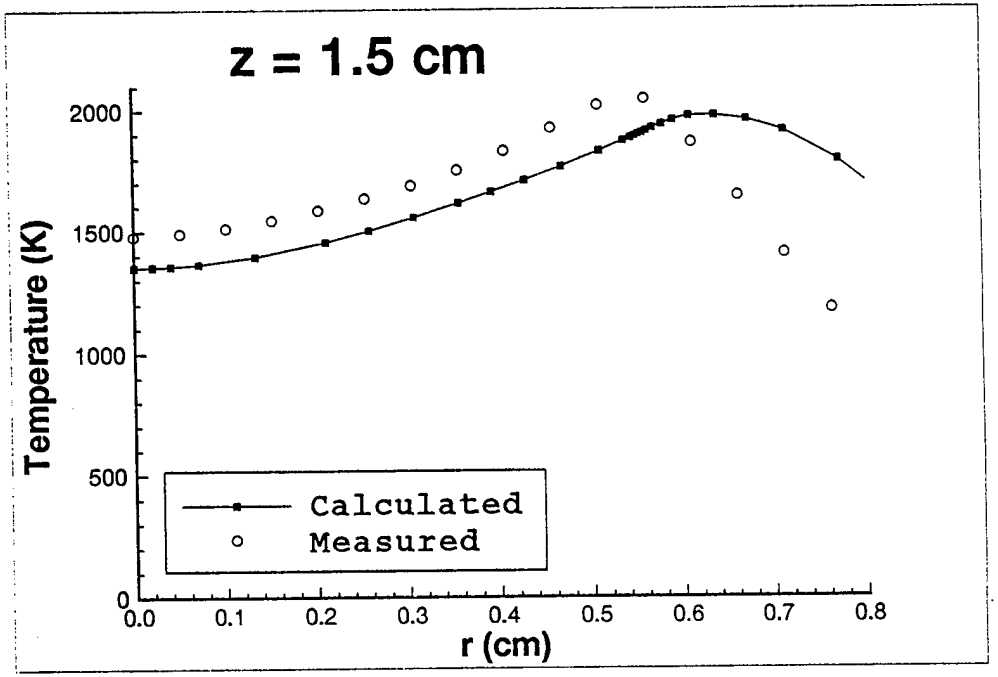
z = 1.5 cm
Temperature (K)
r (cm)
Calculated
Measured

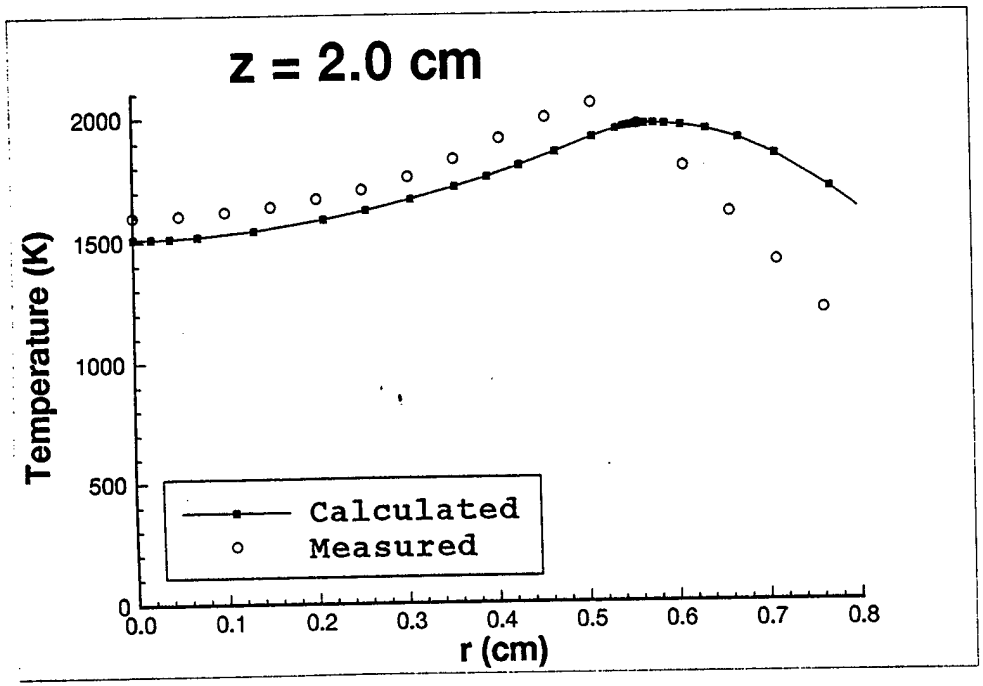
z = 2.0 cm
Temperature (K)
r (cm)
Calculated
Measured

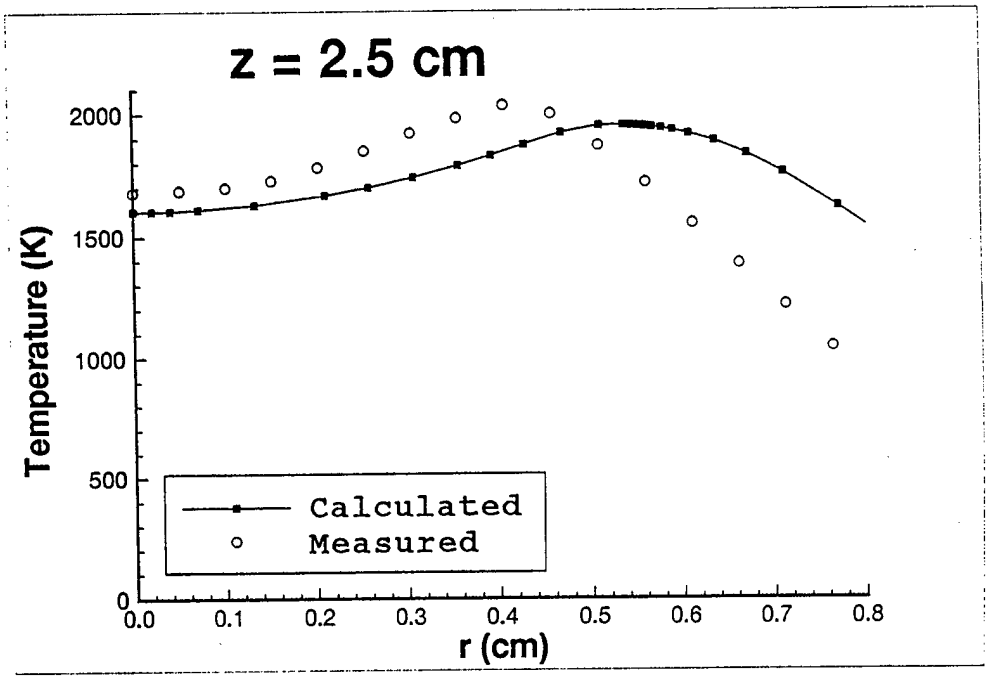
z = 2.5 cm
Temperature (K)
r (cm)
Calculated
Measured

Figure 2

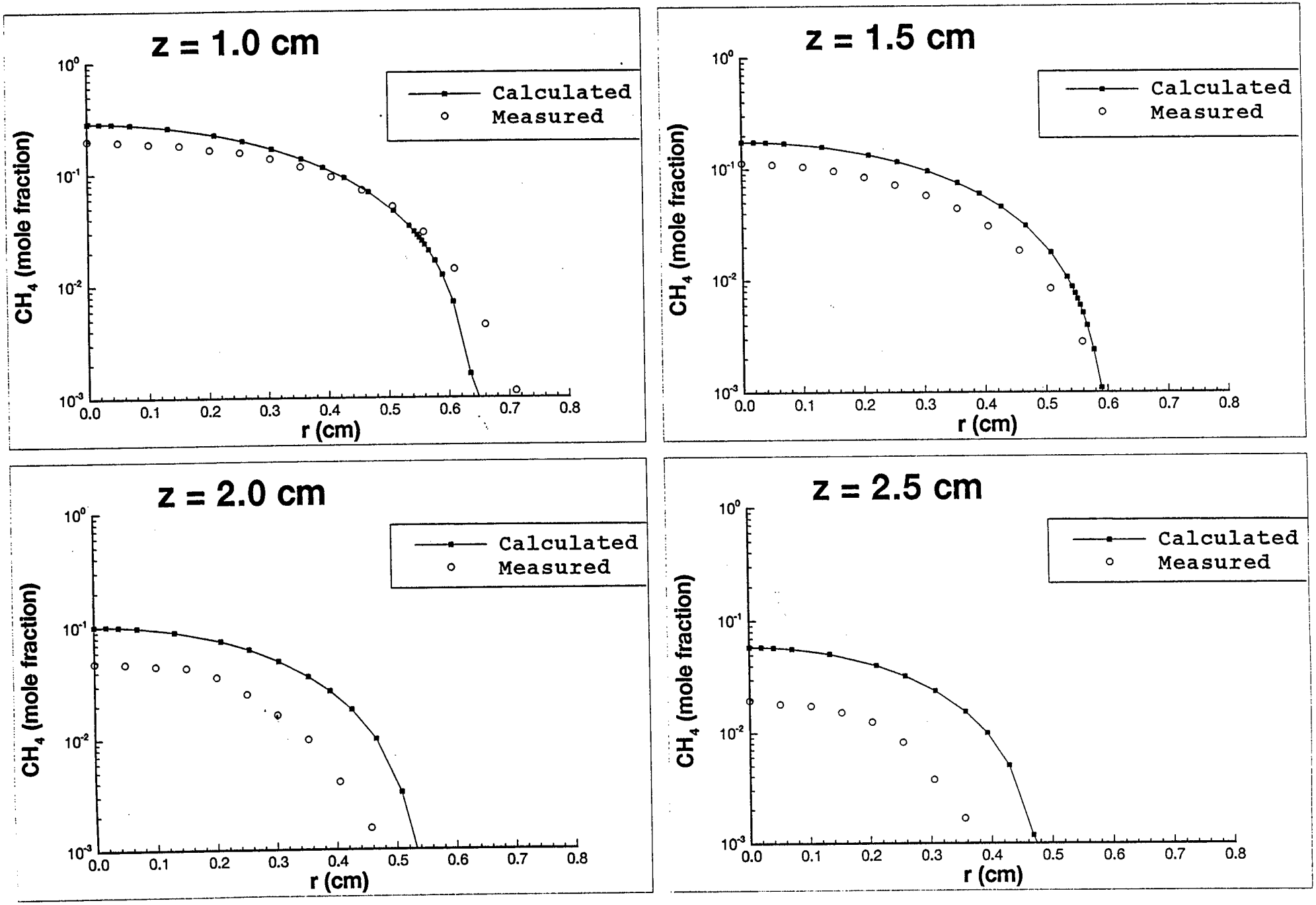
z = 1.0 cm
z = 1.5 cm
z = 2.0 cm
z = 2.5 cm
Calculated
Measured
CH4 (mole fraction)
r (cm)
10^0
10^-1
10^-2
10^-3
0.0
0.1
0.2
0.3
0.4
0.5
0.6
0.7
0.8

Figure 3

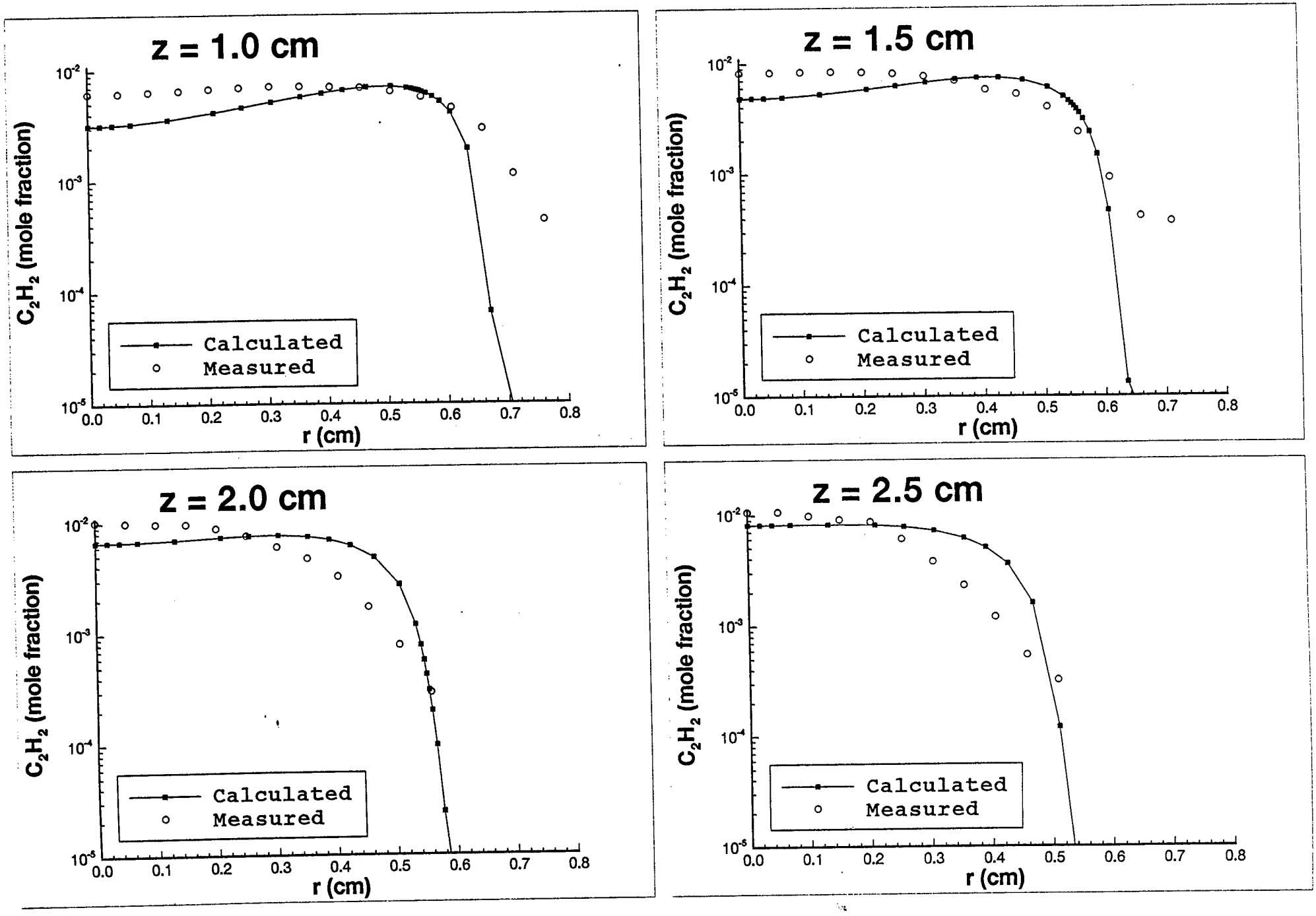
z = 1.0 cm
z = 1.5 cm
z = 2.0 cm
z = 2.5 cm
C_2H_2 (mole fraction)
r (cm)
Calculated
Measured
10^{-2}
10^{-3}
10^{-4}
10^{-5}
0.0
0.1
0.2
0.3
0.4
0.5
0.6
0.7
0.8

Figure 4

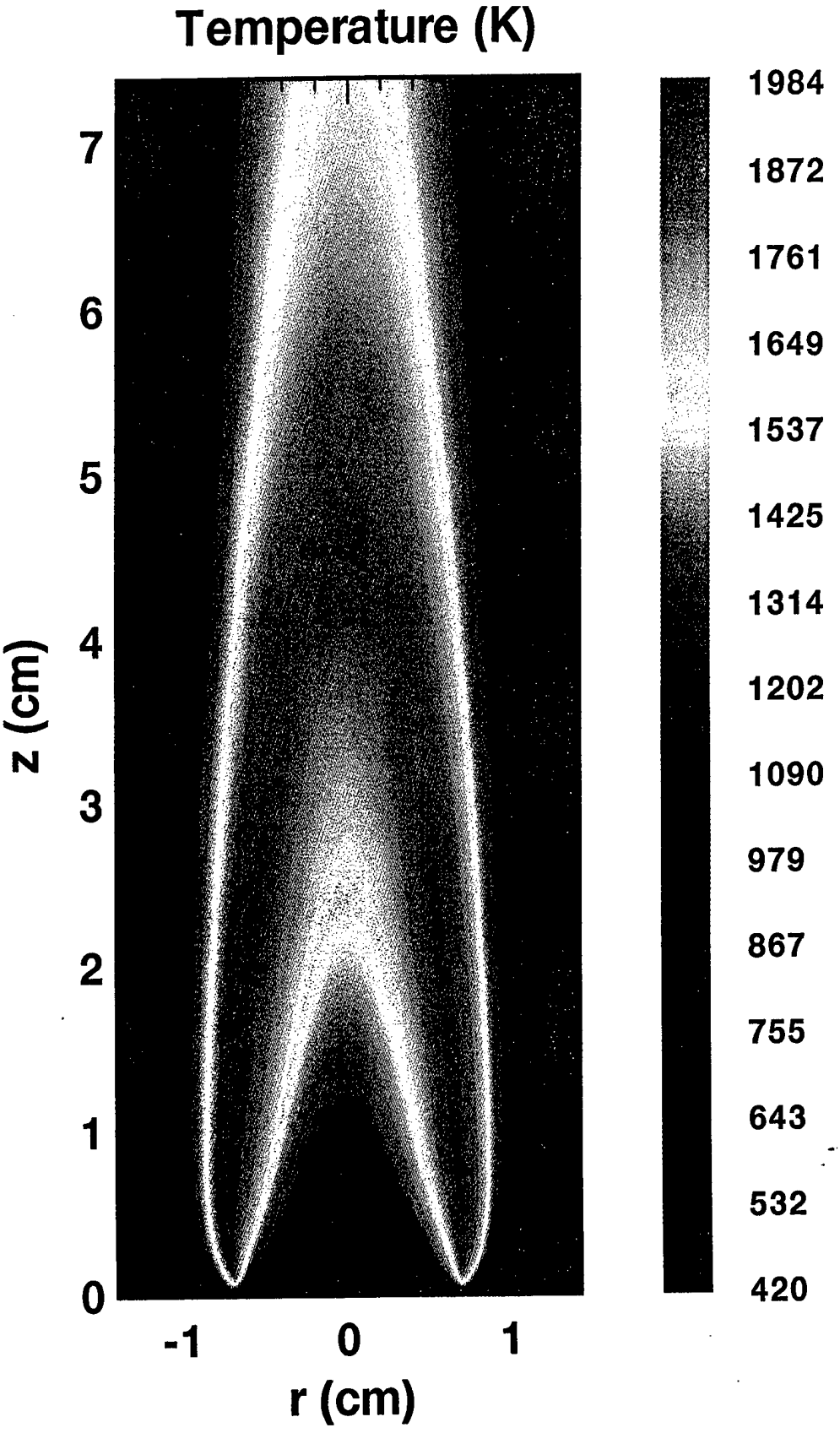
Temperature (K)
1984
1872
1761
1649
1537
1425
1314
1202
1090
979
867
755
643
532
420
z (cm)
0
1
2
3
4
5
6
7
-1
0
1
r (cm)

Figure 7

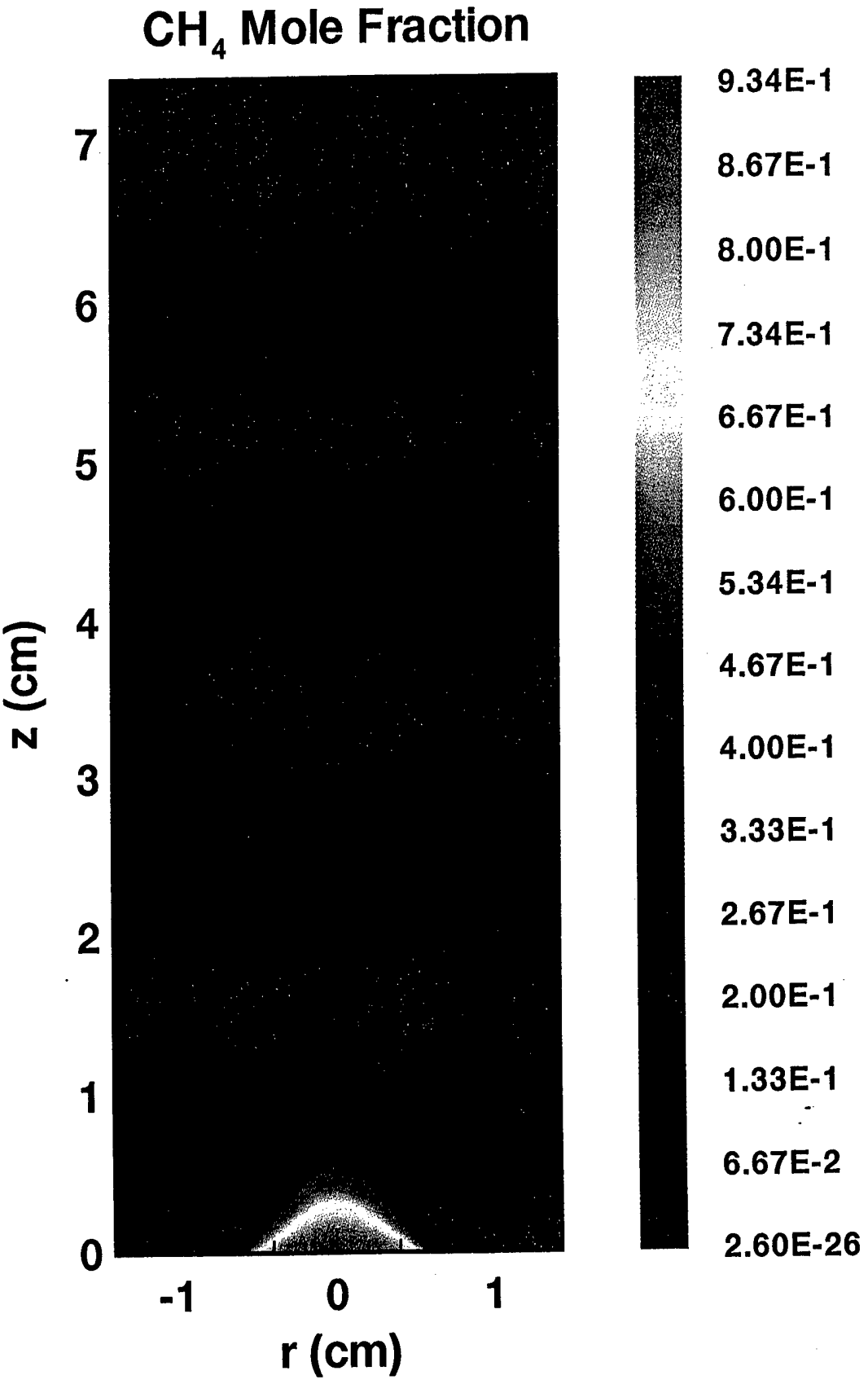
CH4 Mole Fraction
9.34E-1
8.67E-1
8.00E-1
7.34E-1
6.67E-1
6.00E-1
5.34E-1
4.67E-1
4.00E-1
3.33E-1
2.67E-1
2.00E-1
1.33E-1
6.67E-2
2.60E-26
z (cm)
0
1
2
3
4
5
6
7
-1
0
1
r (cm)

Figure 8

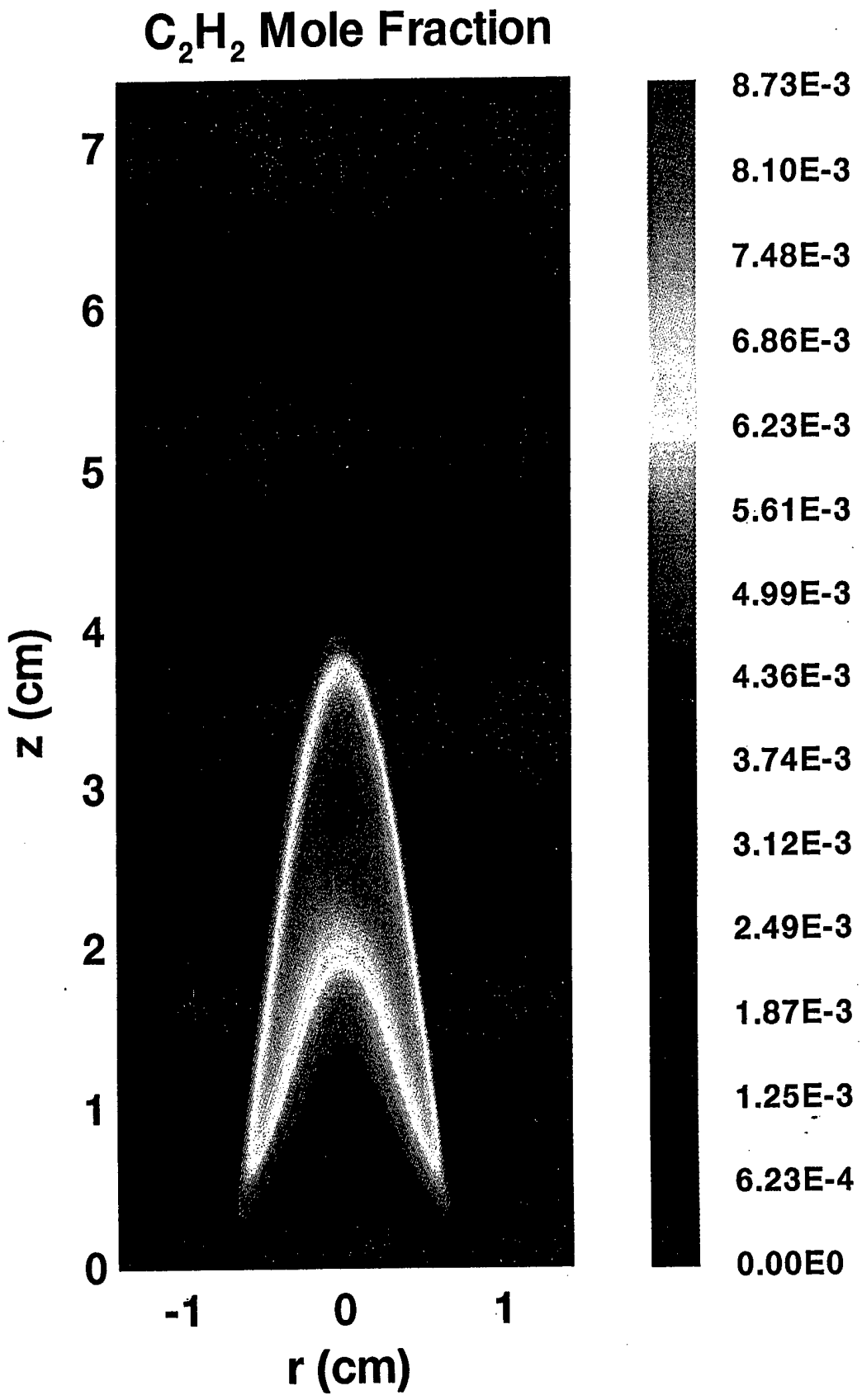
C_2H_2 Mole Fraction
8.73E-3
8.10E-3
7.48E-3
6.86E-3
6.23E-3
5.61E-3
4.99E-3
4.36E-3
3.74E-3
3.12E-3
2.49E-3
1.87E-3
1.25E-3
6.23E-4
0.00E0
z (cm)
0
1
2
3
4
5
6
7
-1
0
1
r (cm)

Figure 9

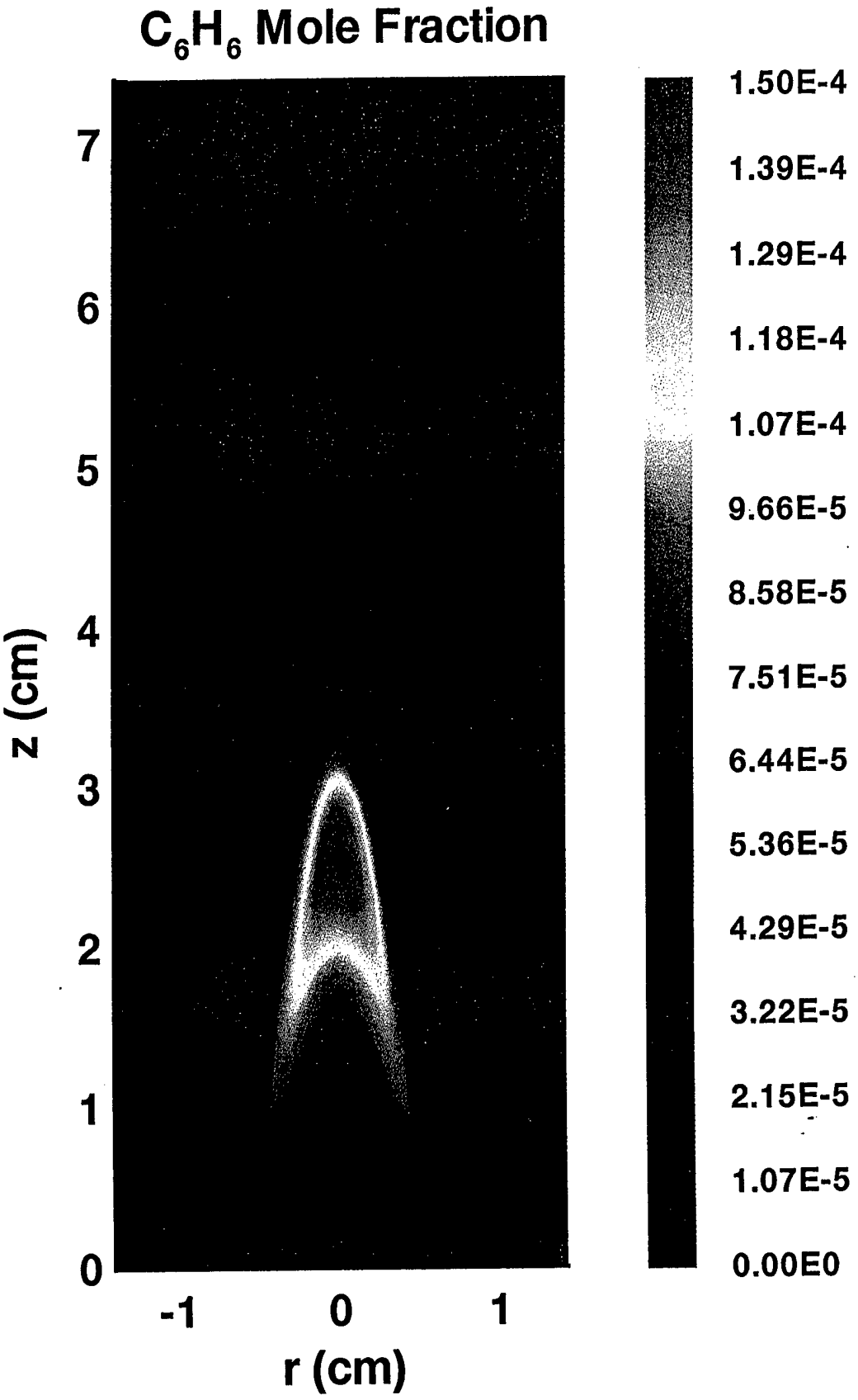
C6H6 Mole Fraction
1.50E-4
1.39E-4
1.29E-4
1.18E-4
1.07E-4
9.66E-5
8.58E-5
7.51E-5
6.44E-5
5.36E-5
4.29E-5
3.22E-5
2.15E-5
1.07E-5
0.00E0
z (cm)
0
1
2
3
4
5
6
7
-1
0
1
r (cm)

Figure 10

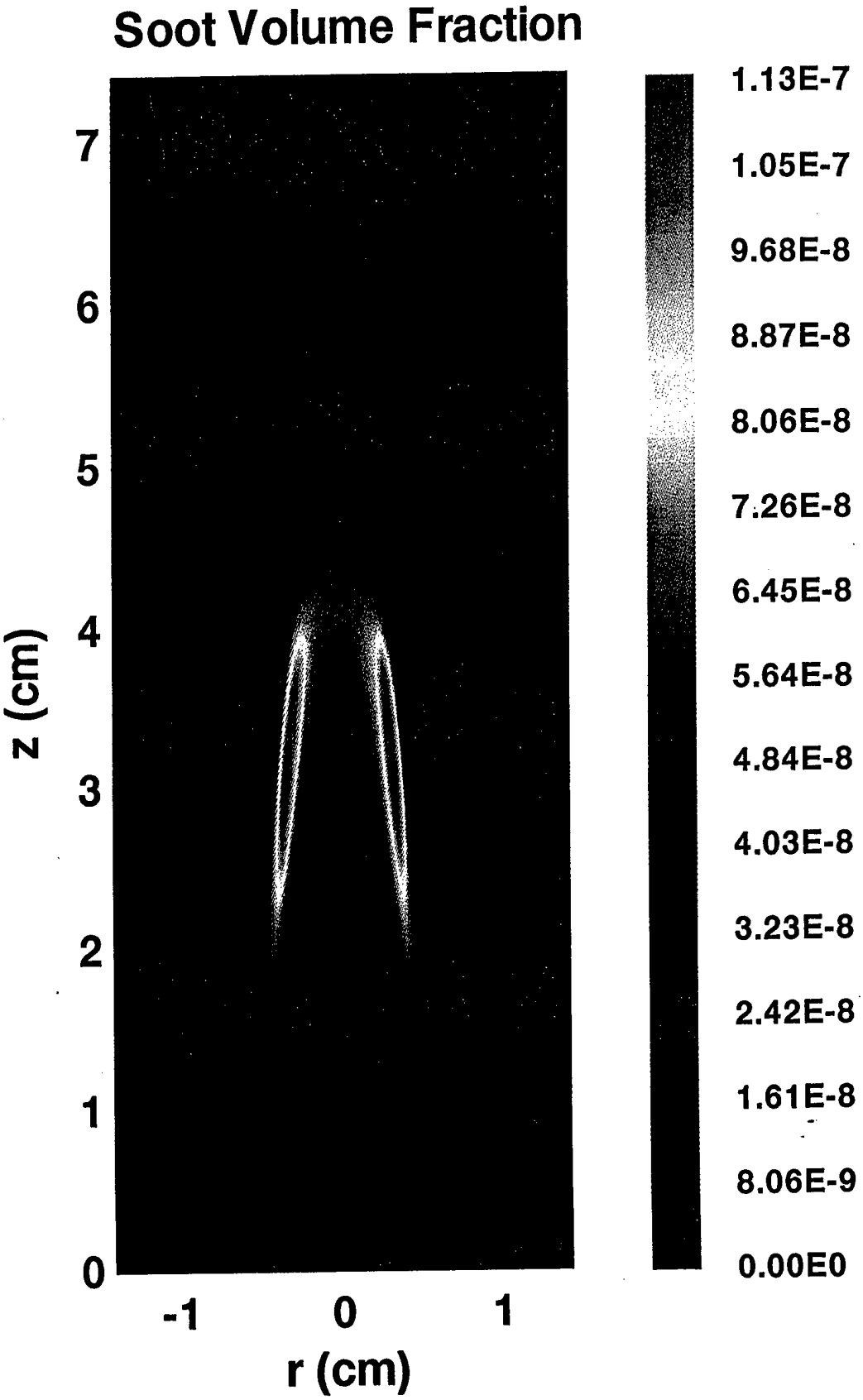
Soot Volume Fraction
1.13E-7
1.05E-7
9.68E-8
8.87E-8
8.06E-8
7.26E-8
6.45E-8
5.64E-8
4.84E-8
4.03E-8
3.23E-8
2.42E-8
1.61E-8
8.06E-9
0.00E0
z (cm)
0
1
2
3
4
5
6
7
-1
0
1
r (cm)

Figure 11

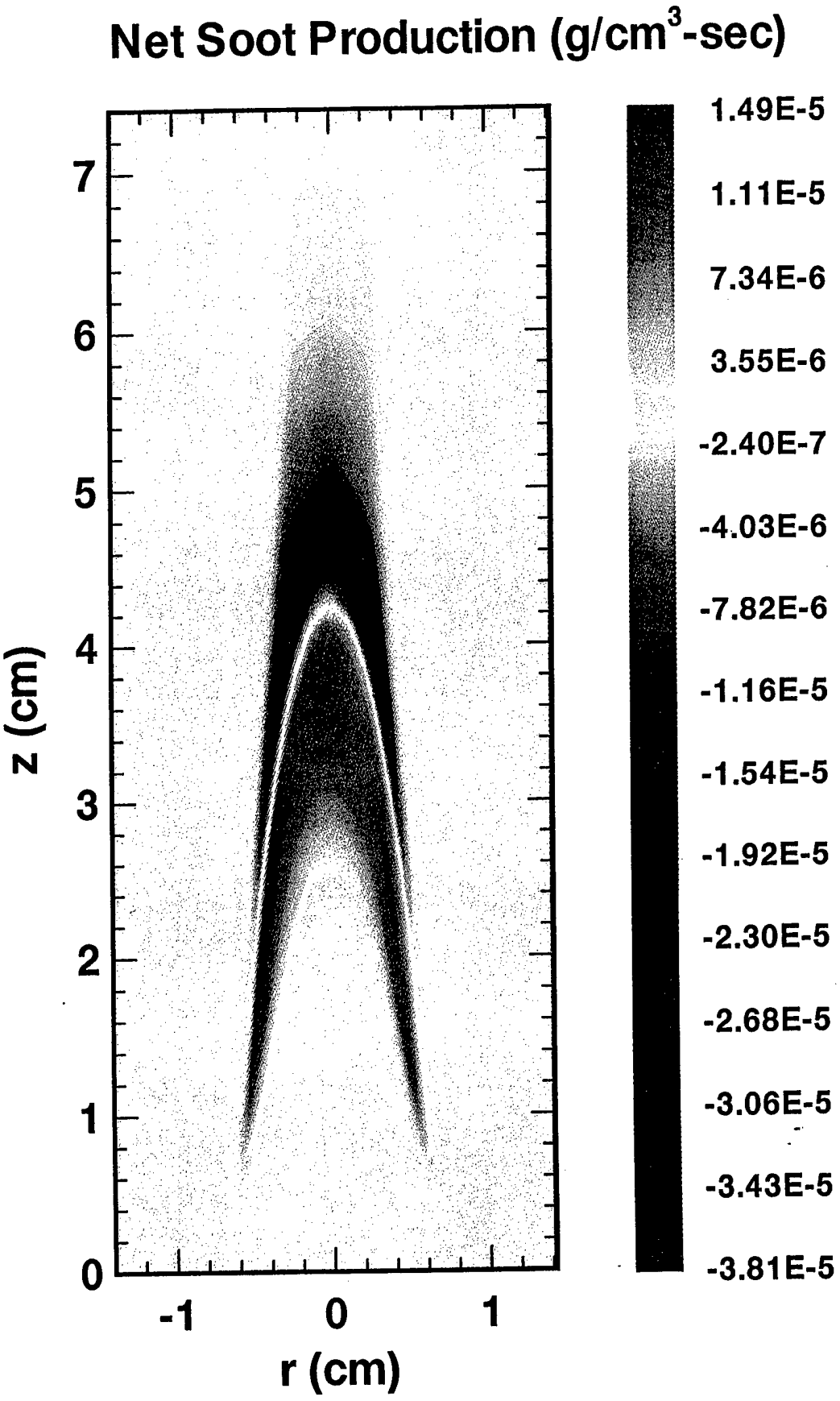
Net Soot Production (g/cm3-sec)
1.49E-5
1.11E-5
7.34E-6
3.55E-6
-2.40E-7
-4.03E-6
-7.82E-6
-1.16E-5
-1.54E-5
-1.92E-5
-2.30E-5
-2.68E-5
-3.06E-5
-3.43E-5
-3.81E-5
z (cm)
0
1
2
3
4
5
6
7
-1
0
1
r (cm)

Figure 12

Comparison of Soot Inception Terms

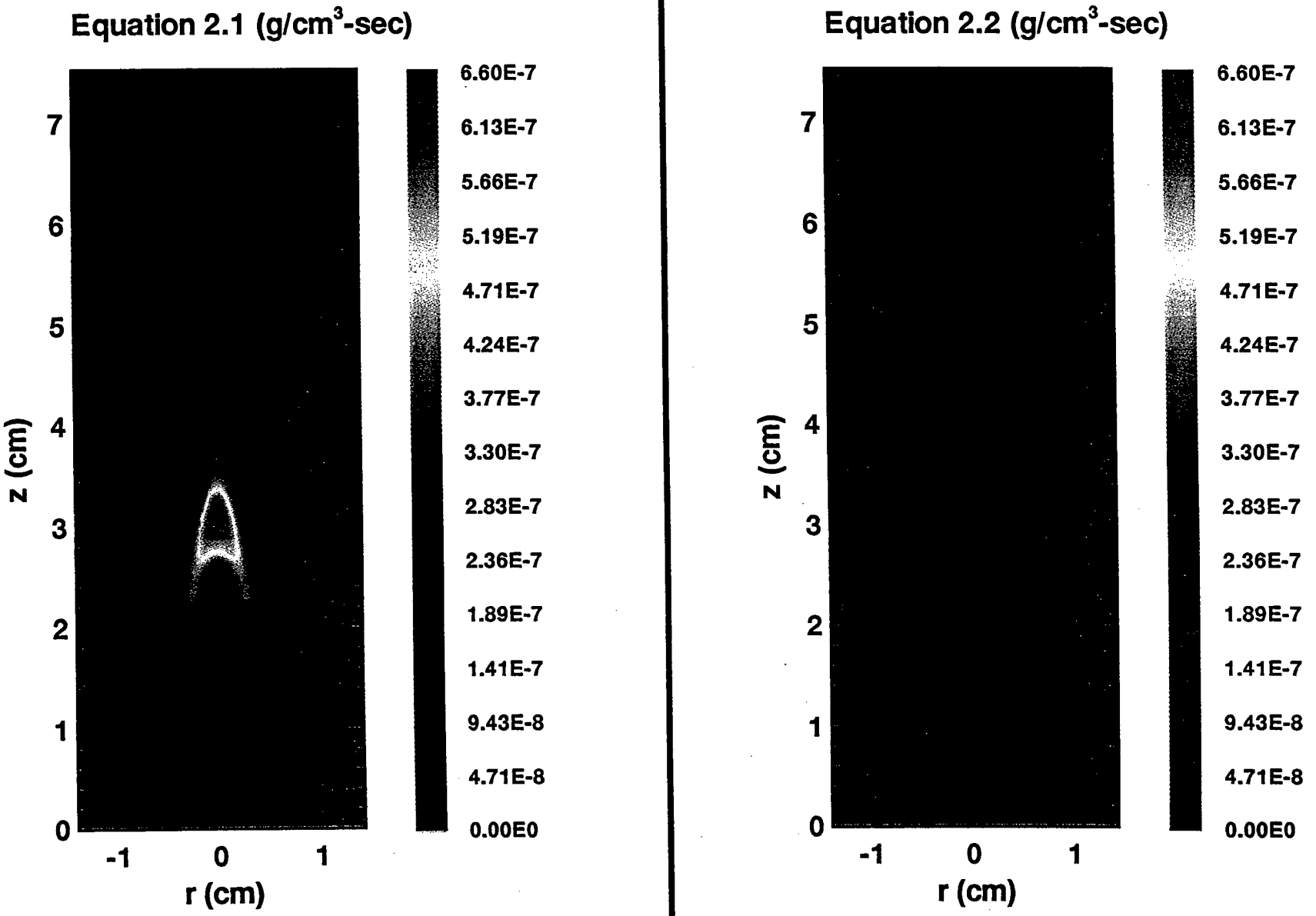

Figure 13

Comparison of Soot Oxidation Due to OH and O_2

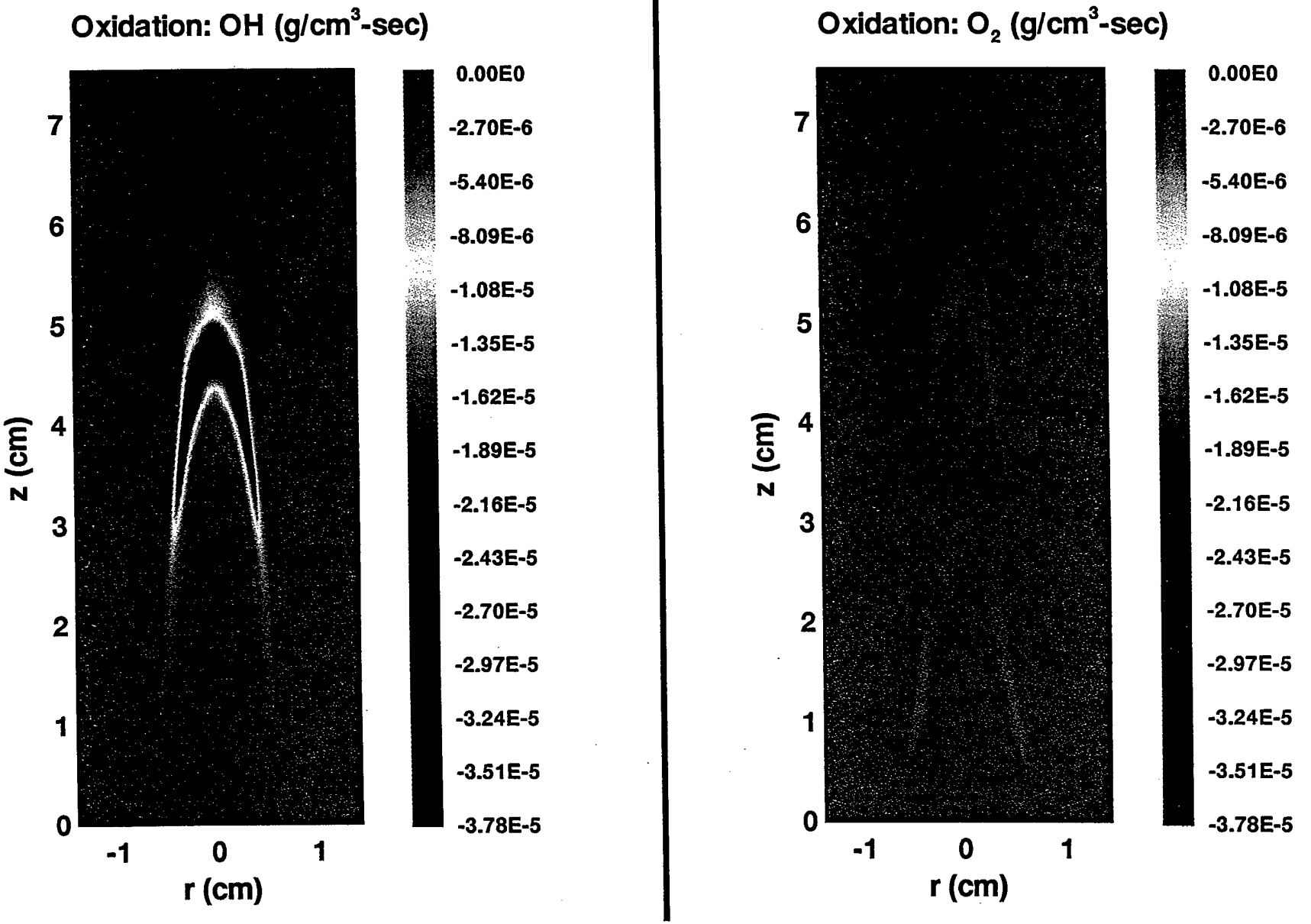

Figure 14

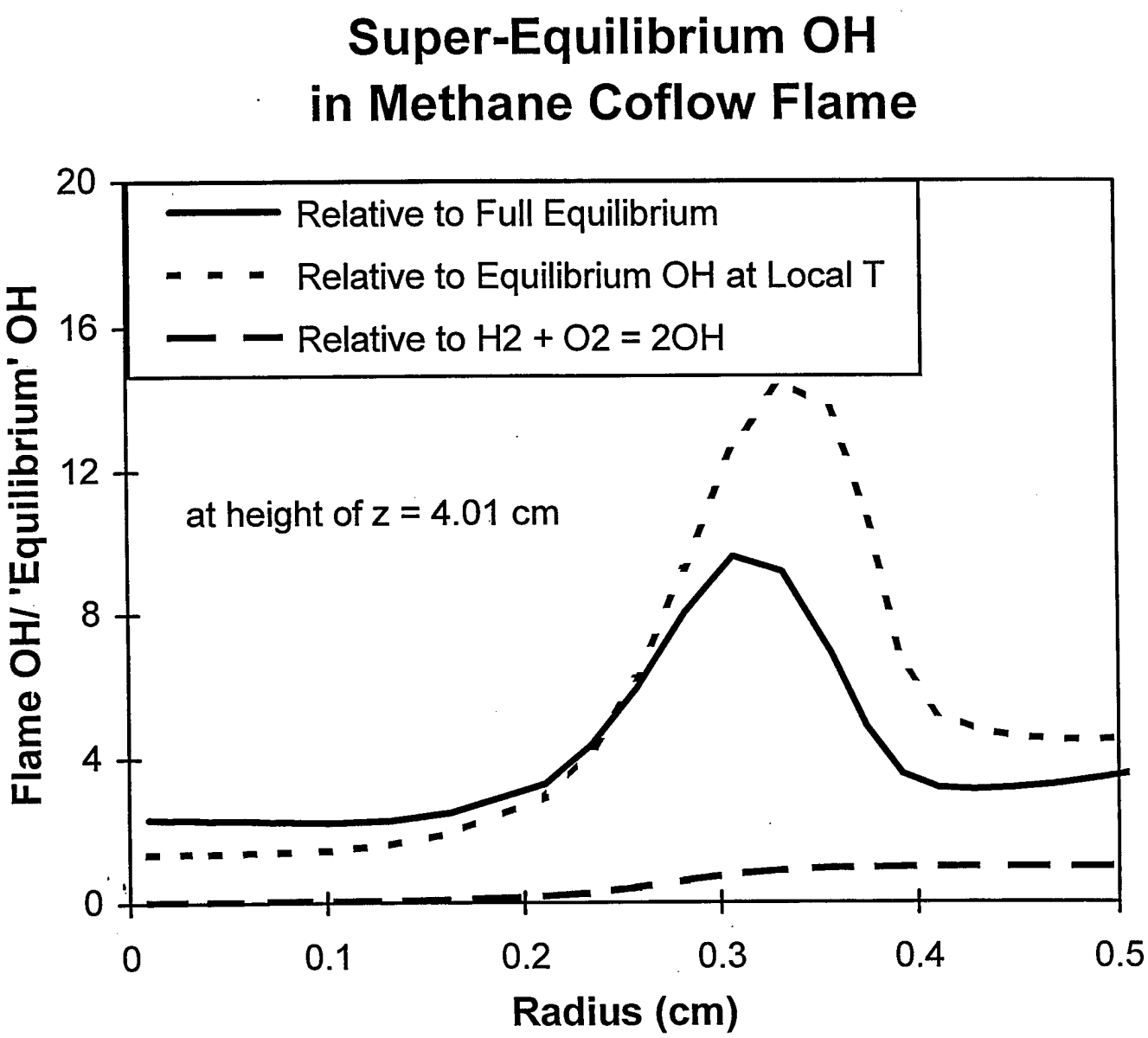
Super-Equilibrium OH
in Methane Coflow Flame
Relative to Full Equilibrium
Relative to Equilibrium OH at Local T
Relative to H2 + O2 = 2OH
at height of z = 4.01 cm
Flame OH/ 'Equilibrium' OH
20
16
12
8
4
0
0
0.1
0.2
0.3
0.4
0.5
Radius (cm)

Figure 15

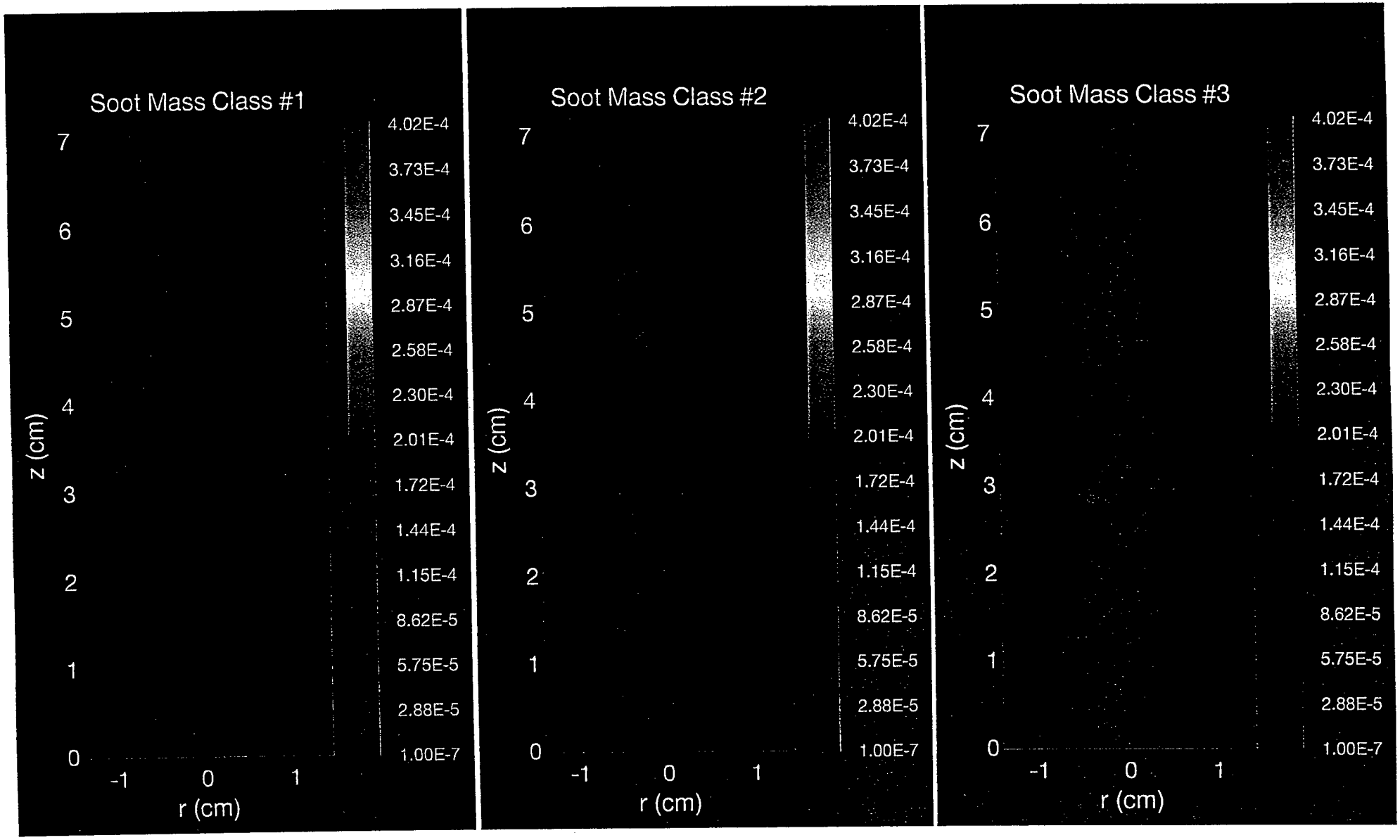
Soot Mass Class #1
Soot Mass Class #2
Soot Mass Class #3
z (cm)
r (cm)
0
1
2
3
4
5
6
7
-1
0
1
4.02E-4
3.73E-4
3.45E-4
3.16E-4
2.87E-4
2.58E-4
2.30E-4
2.01E-4
1.72E-4
1.44E-4
1.15E-4
8.62E-5
5.75E-5
2.88E-5
1.00E-7

Figure 16(a)

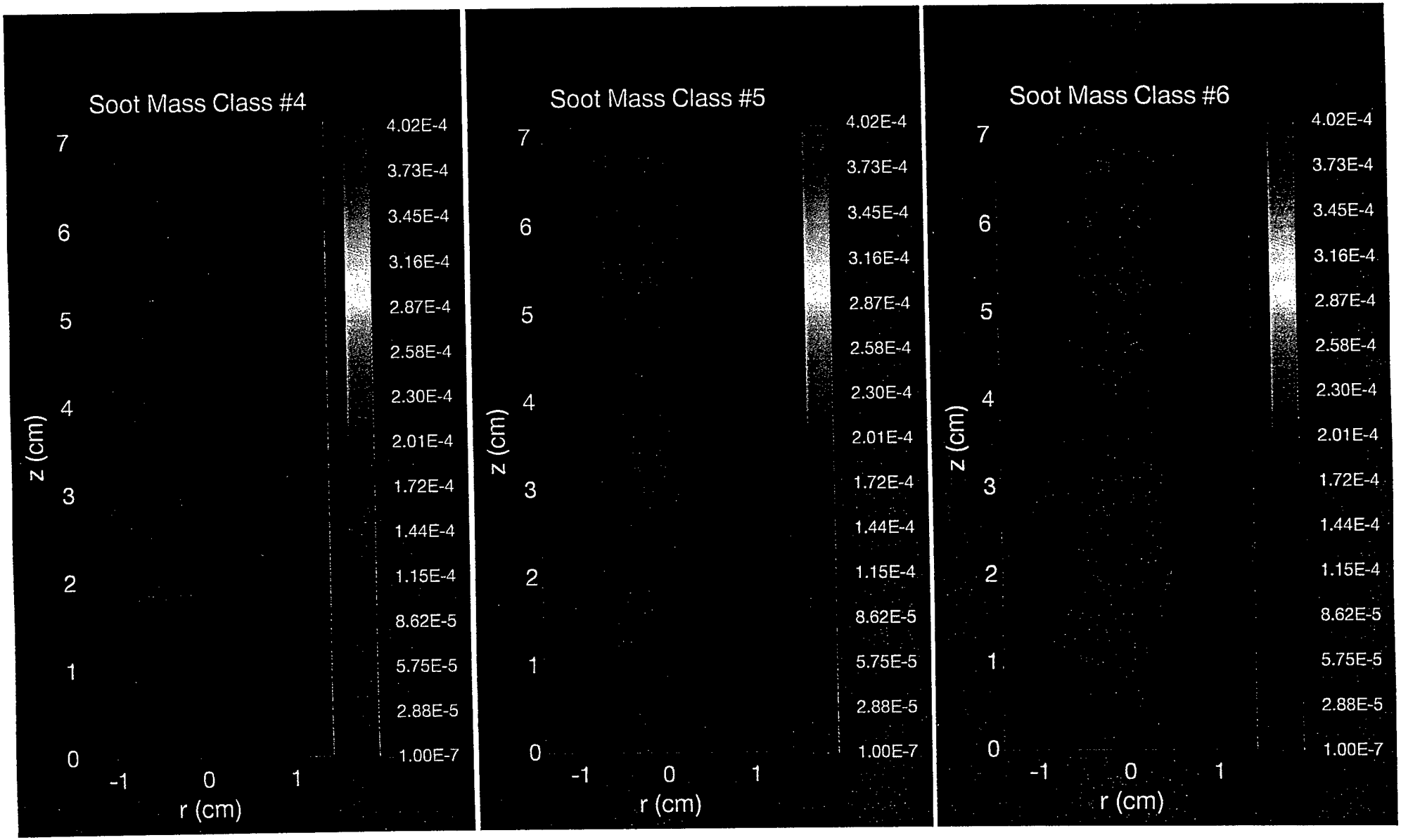
Soot Mass Class #4
Soot Mass Class #5
Soot Mass Class #6
z (cm)
r (cm)
0
1
2
3
4
5
6
7
-1
0
1
4.02E-4
3.73E-4
3.45E-4
3.16E-4
2.87E-4
2.58E-4
2.30E-4
2.01E-4
1.72E-4
1.44E-4
1.15E-4
8.62E-5
5.75E-5
2.88E-5
1.00E-7

Figure 16(b)

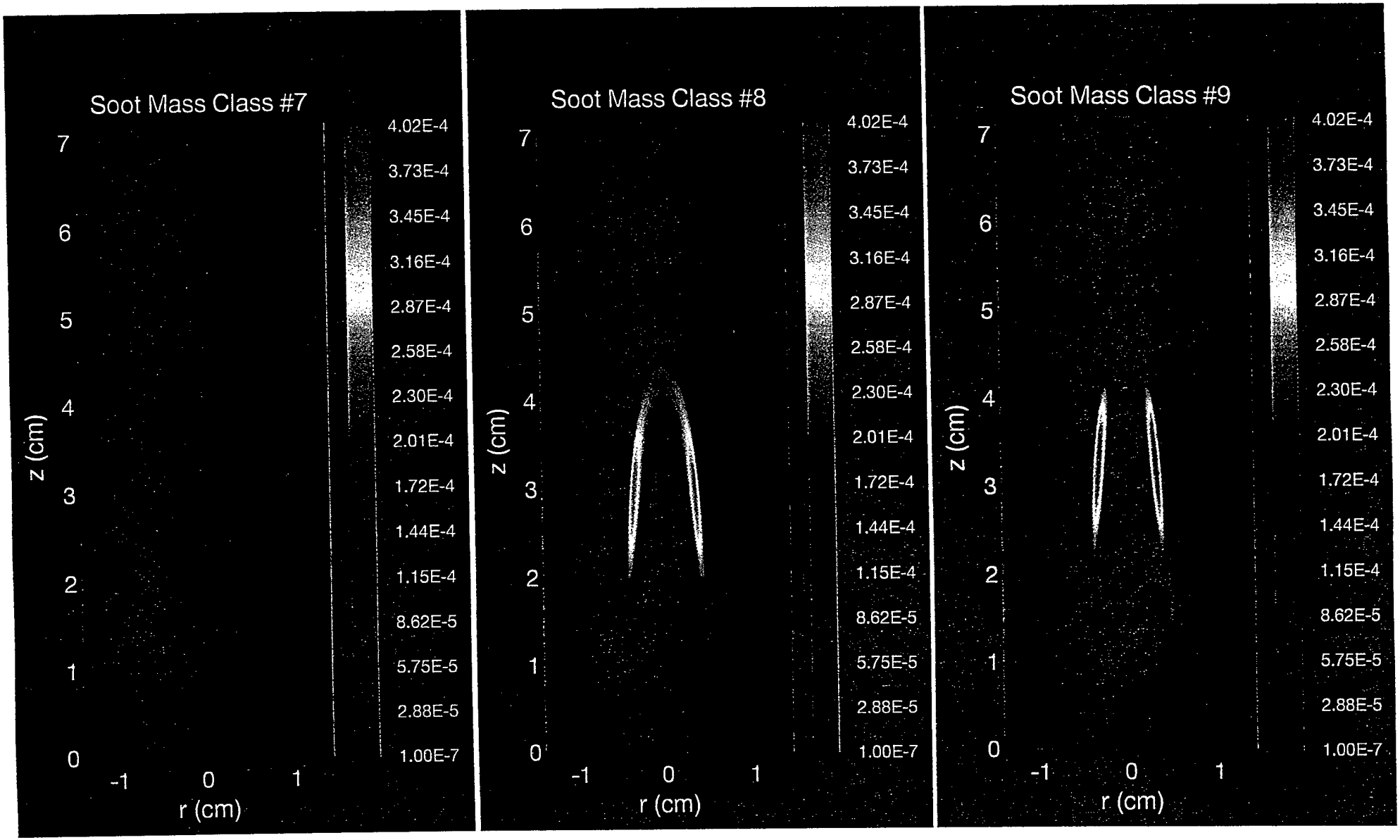
Soot Mass Class #7
Soot Mass Class #8
Soot Mass Class #9
z (cm)
r (cm)
0
1
2
3
4
5
6
7
-1
0
1
4.02E-4
3.73E-4
3.45E-4
3.16E-4
2.87E-4
2.58E-4
2.30E-4
2.01E-4
1.72E-4
1.44E-4
1.15E-4
8.62E-5
5.75E-5
2.88E-5
1.00E-7

Figure 16(c)

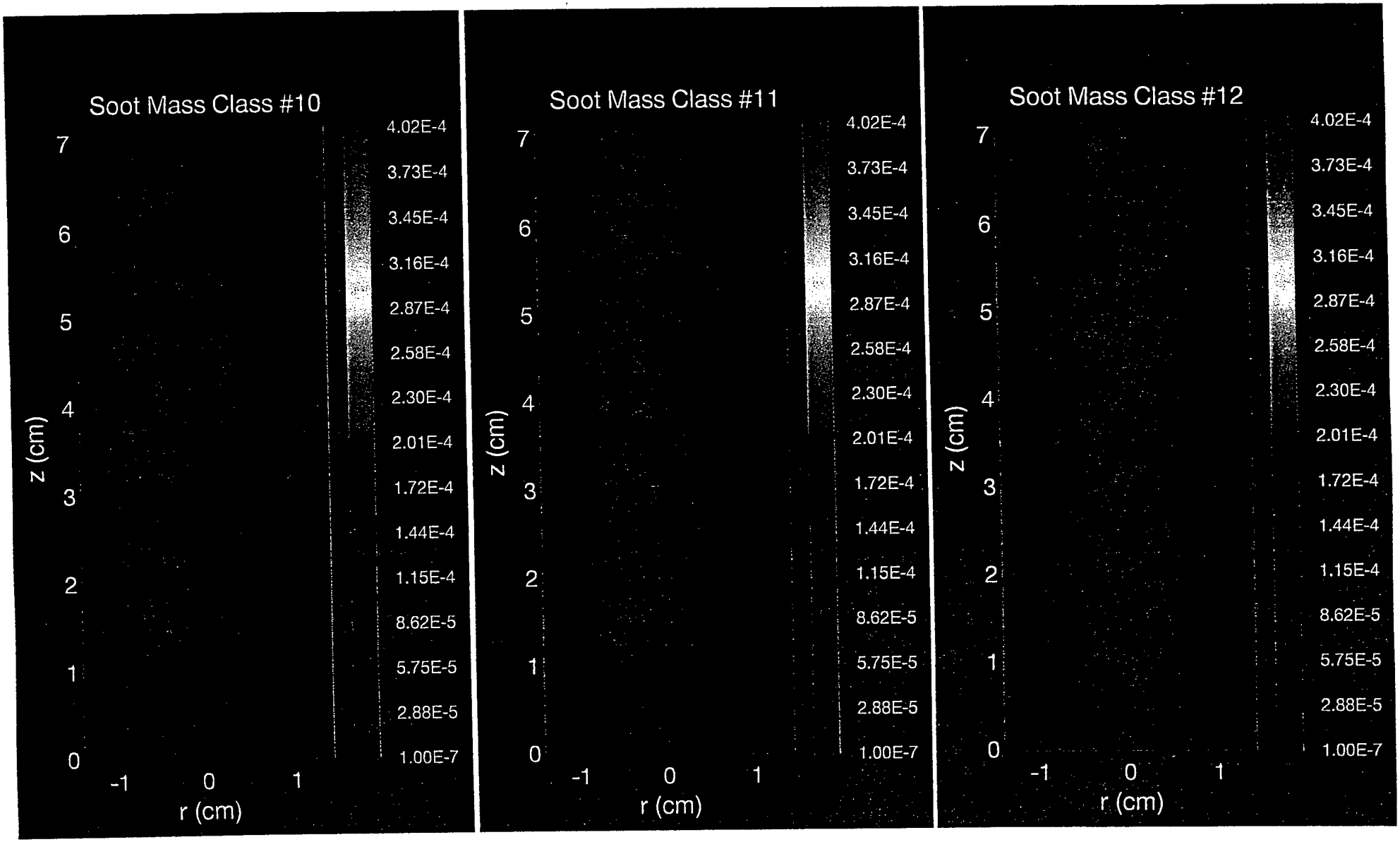
Soot Mass Class #10
Soot Mass Class #11
Soot Mass Class #12
z (cm)
r (cm)
0
1
2
3
4
5
6
7
-1
0
1
4.02E-4
3.73E-4
3.45E-4
3.16E-4
2.87E-4
2.58E-4
2.30E-4
2.01E-4
1.72E-4
1.44E-4
1.15E-4
8.62E-5
5.75E-5
2.88E-5
1.00E-7

Figure 16(d)

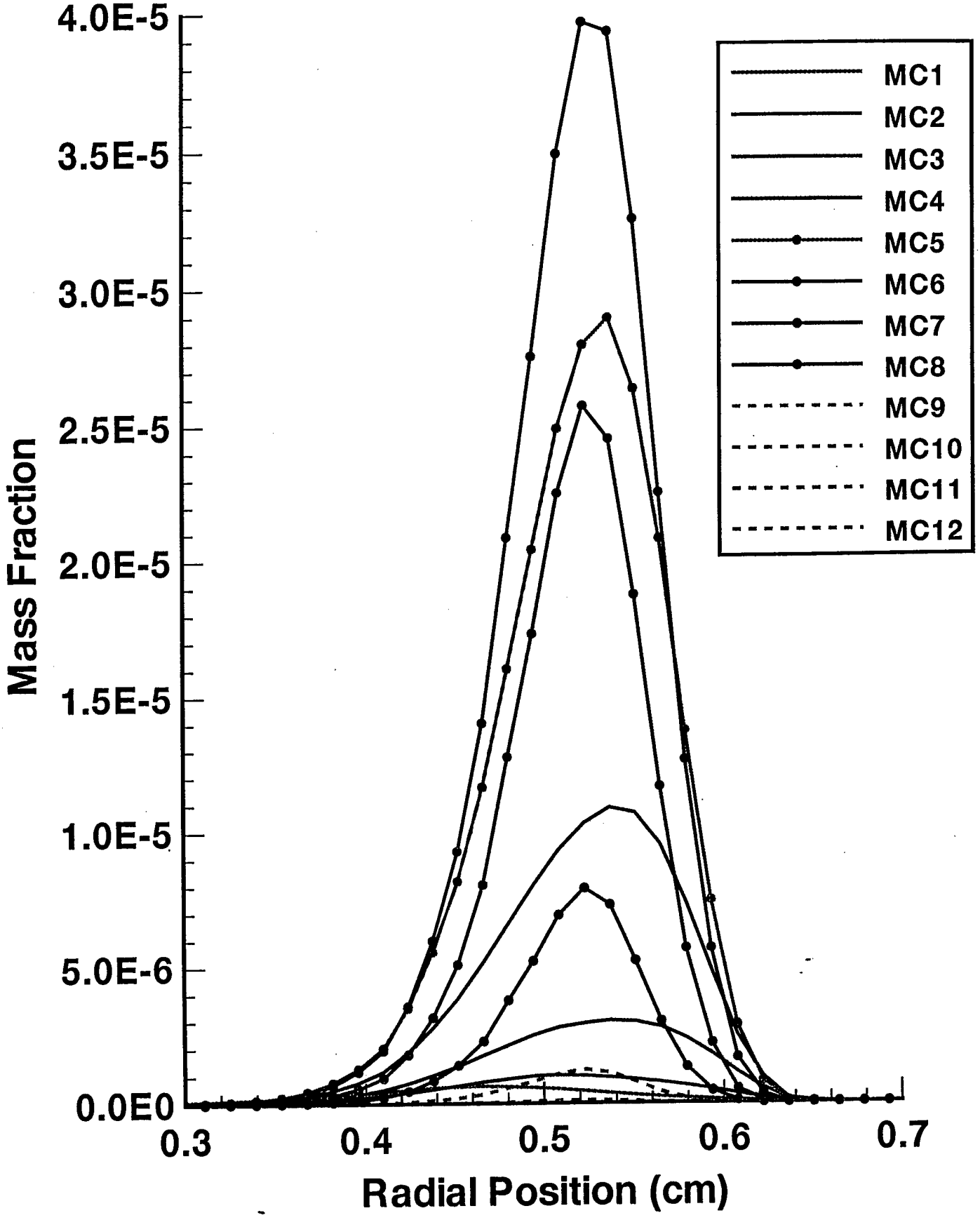
Contributions of the Soot Mass Classes to the Total Soot Volume Fraction (z=1cm)
4.0E-5
3.5E-5
3.0E-5
2.5E-5
2.0E-5
1.5E-5
1.0E-5
5.0E-6
0.0E0
Mass Fraction
0.3
0.4
0.5
0.6
0.7
Radial Position (cm)
MC1
MC2
MC3
MC4
MC5
MC6
MC7
MC8
MC9
MC10
MC11
MC12

Figure 17

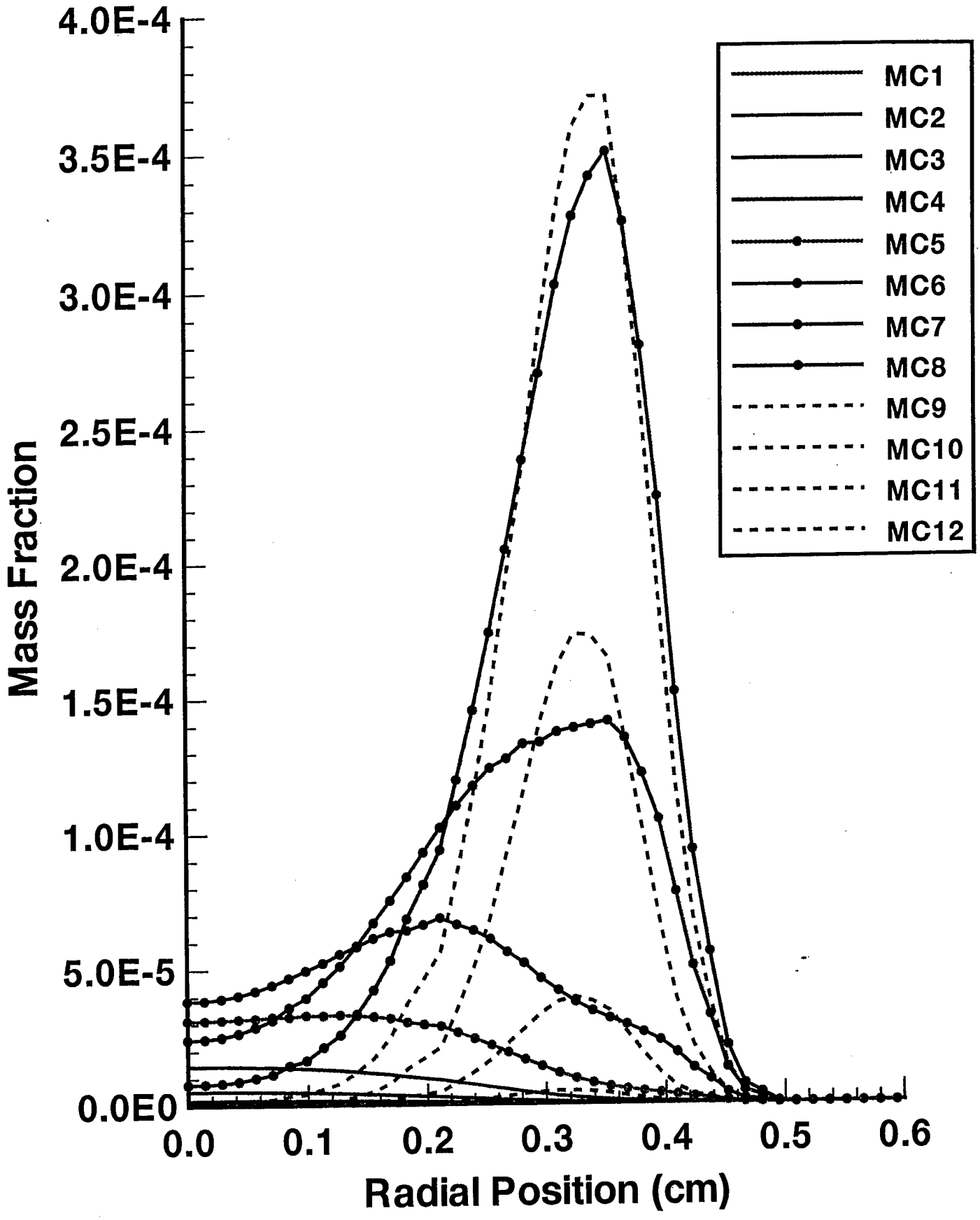
Contributions of the Soot Mass Classes to the Total Soot Volume Fraction (z=3cm)
4.0E-4
3.5E-4
3.0E-4
2.5E-4
2.0E-4
1.5E-4
1.0E-4
5.0E-5
0.0E0
Mass Fraction
0.0
0.1
0.2
0.3
0.4
0.5
0.6
Radial Position (cm)
MC1
MC2
MC3
MC4
MC5
MC6
MC7
MC8
MC9
MC10
MC11
MC12

Figure 18

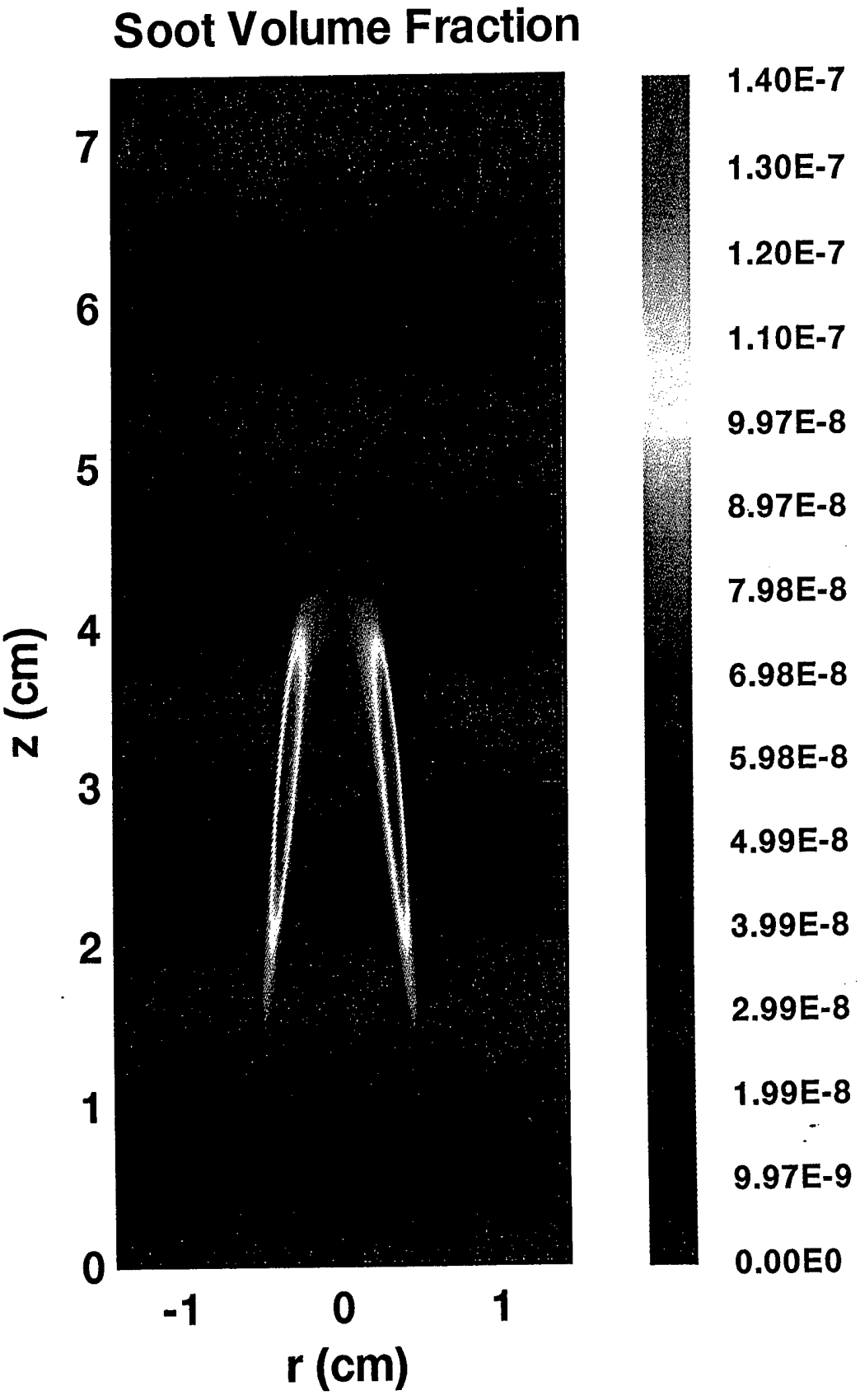
Soot Volume Fraction
1.40E-7
1.30E-7
1.20E-7
1.10E-7
9.97E-8
8.97E-8
7.98E-8
6.98E-8
5.98E-8
4.99E-8
3.99E-8
2.99E-8
1.99E-8
9.97E-9
0.00E0
z (cm)
0
1
2
3
4
5
6
7
-1
0
1
r (cm)

Figure 19

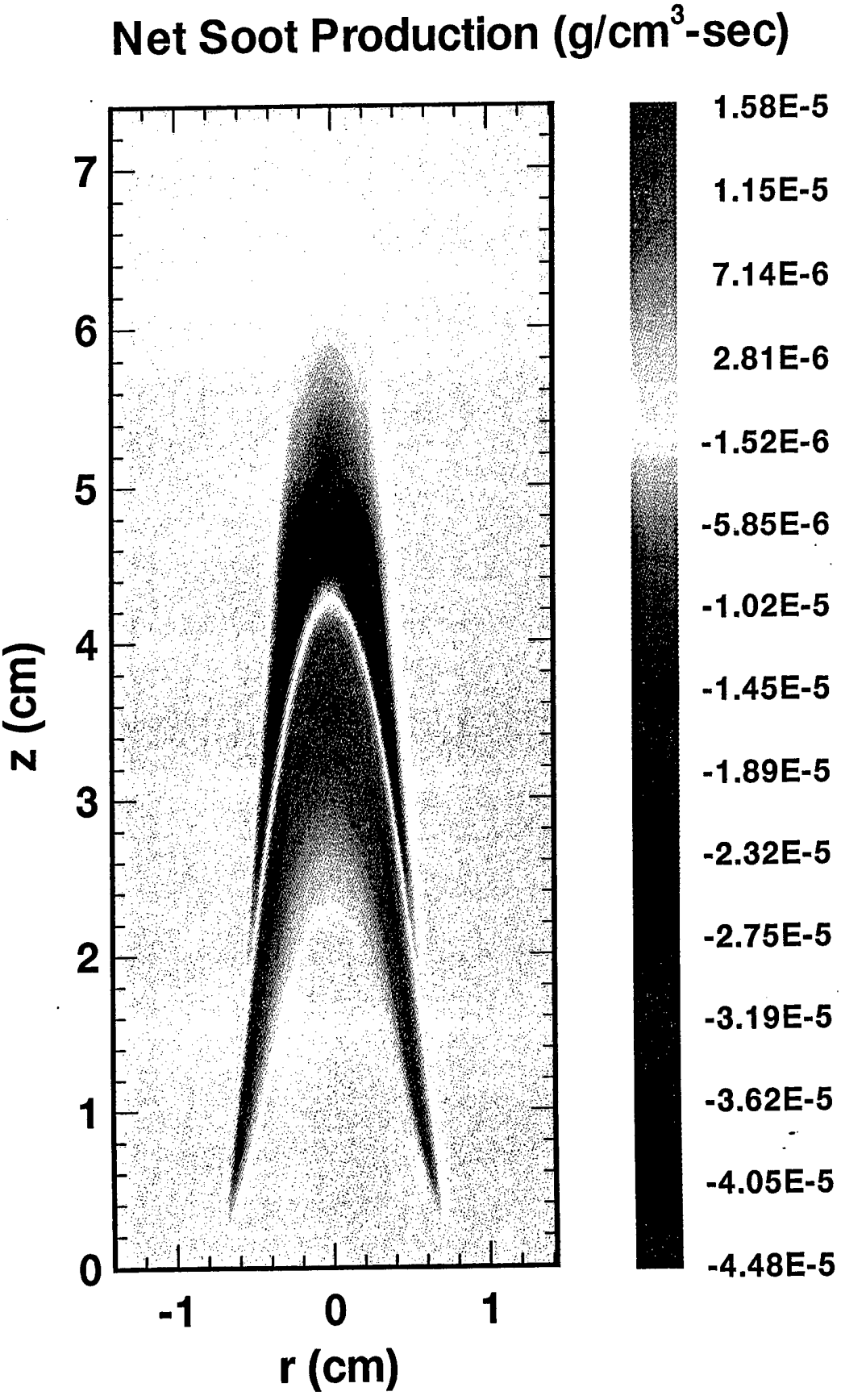
Net Soot Production (g/cm3-sec)
1.58E-5
1.15E-5
7.14E-6
2.81E-6
-1.52E-6
-5.85E-6
-1.02E-5
-1.45E-5
-1.89E-5
-2.32E-5
-2.75E-5
-3.19E-5
-3.62E-5
-4.05E-5
-4.48E-5
z (cm)
0
1
2
3
4
5
6
7
-1
0
1
r (cm)

Figure 20

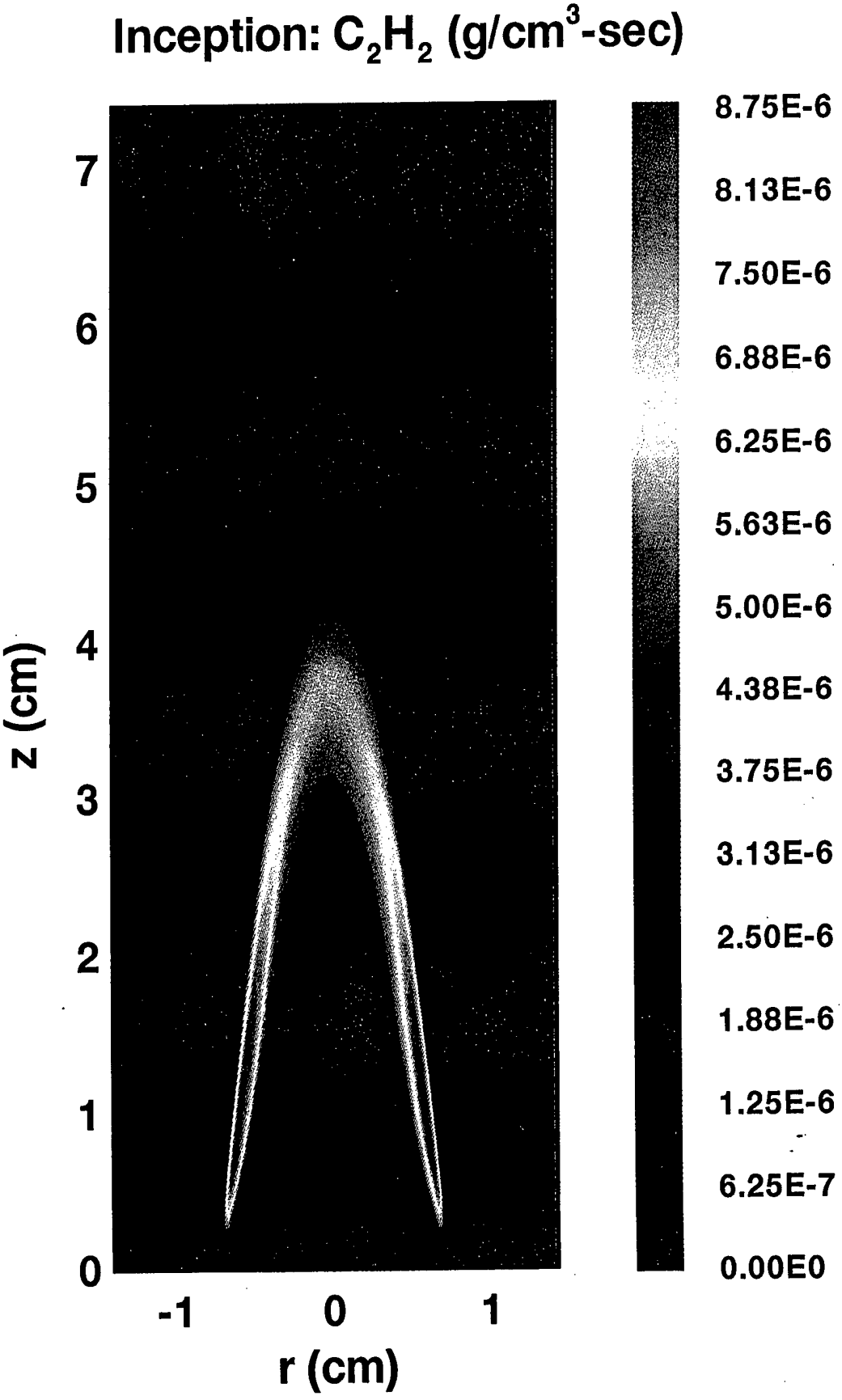
Inception: C_2H_2 (g/cm^3-sec)
8.75E-6
8.13E-6
7.50E-6
6.88E-6
6.25E-6
5.63E-6
5.00E-6
4.38E-6
3.75E-6
3.13E-6
2.50E-6
1.88E-6
1.25E-6
6.25E-7
0.00E0
z (cm)
0
1
2
3
4
5
6
7
-1
0
1
r (cm)

Figure 21

Comparison of Soot Oxidation Due to OH and O_2

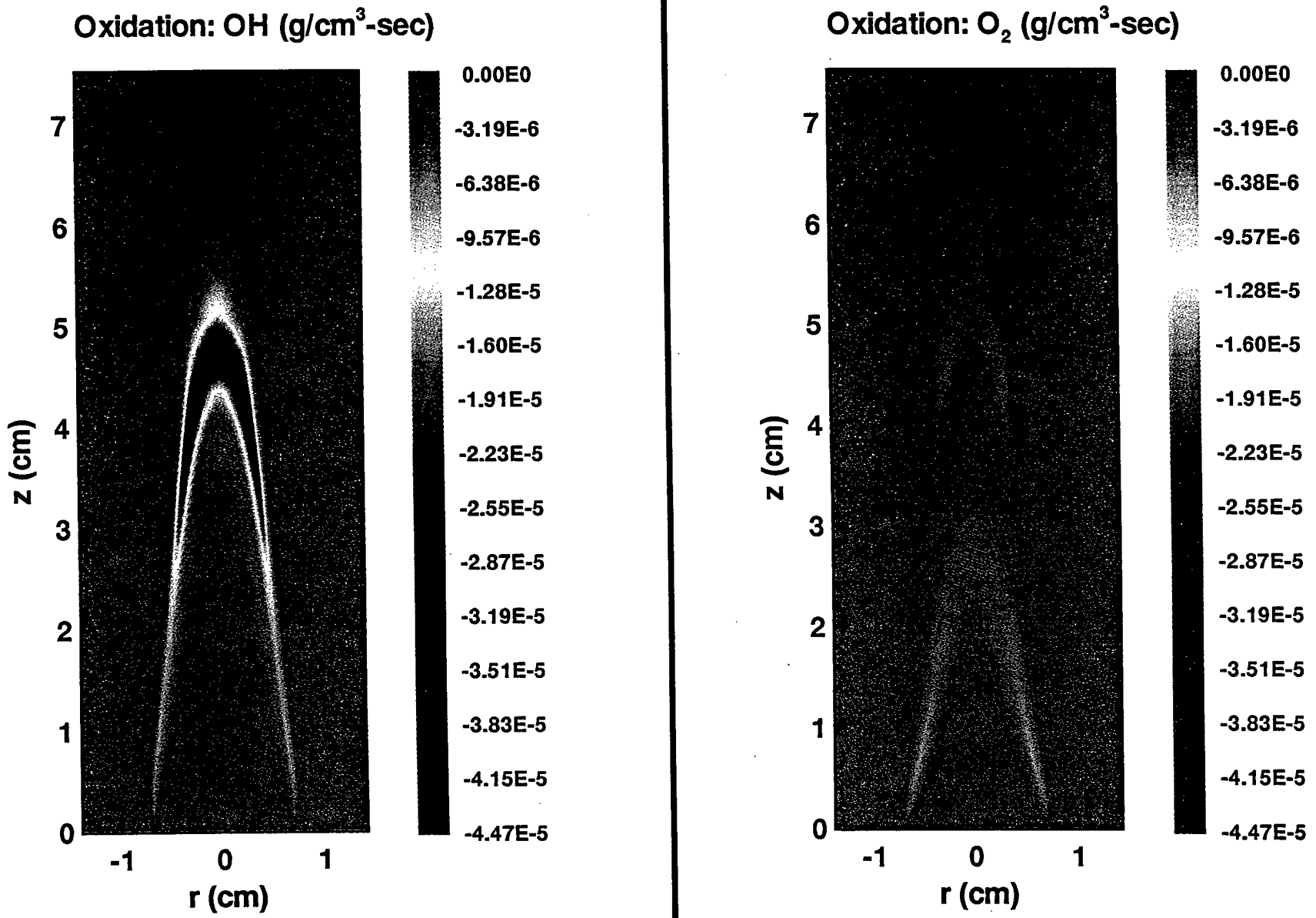

Figure 22

Appendix C
Interpretations of a Computational Study of Soot Formation in a Coflow, Laminar Diffusion Flame

INTERPRETATIONS OF A COMPUTATIONAL STUDY OF SOOT FORMATION IN A COFLOW, LAMINAR DIFFUSION FLAME

by
M. D. Smooke (mitchell.smooke@yale.edu),
Departments of Mechanical and Chemical Engineering
Yale University, New Haven, CT 06520
and
R. J. Hall (hallrj@utrc.utc.com) and M. B. Colket (colketmb@utrc.utc.com)
United Technologies Research Center
E. Hartford, CT 06108

Presentation to the Eastern States Section of the Combustion Institute
Hartford, CT. October 27-29, 1997

Introduction

Coflow axisymmetric flames are often employed as a base flame for describing practical combustion devices as well as for gaining information on interactions between heat and mass transfer as well as detailed chemistry. The ability to predict these coupled effects is critical to the modeling of turbulent reacting flows and to the understanding of the controlling phenomena related to generation of pollutants. Most studies using detailed chemical kinetics and coupled models of soot production and oxidation for examining computational combustion have focused on one dimensional geometries. A few recent studies [e.g., 1,2] have focused on multi-dimensional problems in which monodisperse soot formation models and skeletal chemical kinetic mechanisms were used. This abstract describes the results [3] of a more recent modeling study which includes both detailed chemical kinetics and a sectional analysis of particle dynamics and then presents some interpretations of model predictions for a lightly sooting, coflow methane flame.

Brief Description of Model and Results

In the recent study [3], a detailed model with fully coupled, elliptic, two-dimensional equations including soot production was developed and compared to experimental data from an axisymmetric, laminar, methane/air coflow diffusion flame. The two-dimensional model includes a detailed transport, finite rate (detailed) chemistry gas phase system coupled with aerosol dynamical equations in the sectional representation. Detailed submodels for the inception, growth, oxidation and dynamics of soot particulates as well as effects of radiation were included in the model [4,5]. Predictions and measurements of temperature, soot volume fractions and selected species were compared over a range of heights and as a function of radius. Consistent with the experimental data, peak soot volume fractions were predicted in an annulus region just inside the flame front. If radiation losses were not included, the peak flame temperature increased by more than 100K with an attendant increase by a factor of three in the predicted peak soot volume fractions. Initial modeling results significantly underpredicted the peak temperatures and soot volume fractions and overpredicted the flame height. Increasing gas inlet temperatures, particularly the air temperature, led to better agreement with the experimental data and a constant

inlet temperature of 420K was used for additional analysis. The model predicted the flame to be about 4.8 cm tall (as defined by peak temperature along the centerline). Soot growth rates start to become large in the annulus region of the flame at a height of about 0.9 cm. Peak growth rates are found at about 2.2 cm high and soot undergoes significant decay with rapid oxidation occurring above 3.7 cm. Many interpretations of the model and comparisons to data are presented in [3].

Interpretations

Hydroxyl radicals in the flame front, and most importantly in the soot oxidation region, attain levels which are about 10 times higher than the local equilibrium conditions. A comparison of the predicted [OH] as a function of radius, relative to various methods for estimating the radical concentration, is shown in Fig. 1 at a height of 4 cm. At this height and at a radius of 0.3 cm, peak soot volume fractions are rapidly decaying as soot rapidly oxidizes due to high reaction rates with hydroxyl radicals. These results strongly support the dominant role of hydroxyl radical to the oxidation of soot in coflow flames and demonstrate the importance of super-equilibrium [OH]. The erroneous assumption of equilibrium [OH] can readily lead one to conclude incorrectly that treatment of oxidation by O_2, alone, is sufficient.

The environment in which soot is formed was examined by plotting in Fig. 2 the locii of peak soot surface growth rates (at each height) on curves of temperature as a function of radius. Soot formation (i.e., surface growth rates) maximizes on the rich side of the flame at temperatures of 1720-1760K, a temperature which is in the vicinity of the traditional peak of the well-known, bell-shaped curve for soot formation. The lower end of this temperature range is probably a better characteristic temperature for the peak surface growth rate, as the 1760K value at the centerline, near the top of the flame, is the lowest temperature on the rich side attained at this height in the flame. Additional information about the soot formation region can be extracted from calculations of the local equivalence ratio, based the local gas phase C, H, O elemental concentrations. These local equivalence ratios are plotted in Fig. 3, as a function of radius and for several flame heights. The locii of peak flame temperatures are shown and confirms that peak temperatures occur at or near the rich side of the stoichiometric flame surface. The locations of peak surface growth rates, as well as those of peak soot volume fractions, are also plotted in Fig. 3. Lower in the flame, these regions coincide near equivalence ratios of 1.8, separate and move to less rich regions of the flow with increasing flame height. The coincidence of the peak surface growth rates and the peak soot volume fractions is a significantly different result from that of counterflow flames. In the latter flames, small soot particles formed at high temperatures near the flame front are rapidly pushed [5] by both thermophoresis and convection towards the cooler stagnation plane (about 900K) where coagulation occurs readily and surface growth is slow due to the low local temperatures. Thus, it is likely that there may be distinct issues, particularly with regard to the relative importance of surface growth and coagulation/coalescence between the two flame types. As an example, 'ageing' effects should be more significant for coflow flames in which soot particulates, once formed, remain in a high temperature zone. Although inception, surface growth and coalescence are treated in our model, neither ageing nor agglomeration, however, are yet included in our analysis and, hence, the impact of these processes on model solutions is uncertain.

Also of interest in this analysis is a calculation showing the effects of differential species diffusion. Radial variations of the local H/C molar ratio are plotted in Fig. 4 for several flame

heights. These calculations clearly show the effect of light molecular weight species, i.e., H and H_2 (and presumably some H_2O), that rapidly diffuse through the flame front and out beyond the wings of the flame. A resultant minimum in the H/C ratio generally occurs just inside the peak flame temperature region (shown in the figure) and then it grows again with increasing radius as there is no carbon in the coflow air stream. The impact on the soot formation process is that the local H/C ratios where soot is produced are noticeably lower (by about 10%) from that of the neat fuel.

In these calculations, 12 size classes were employed, with lower and upper mass limits of 127 to $1.5x10^{10}$ amu. This upper mass boundary (not average mass) of the largest size class was picked such that the solution was independent of this boundary. Particle size distributions can be determined at each location within the flame and are not à priori assumed. Peak volume fraction occurs in size class nine, with a mass-weighted mean diameter of 48 nm. This relatively large size is likely larger than the experimental value, perhaps in part due to the lack of ageing effects in our model formulation. The average size of particles is much lower along the centerline, consistent with the recent studies by Dobbins and coworkers [6] in an ethylene diffusion flame. This flame would normally be classified as non-sooting in that the experiment indicates that soot does not escape from the 'wing-tips'. A close examination of the computational solution indicates that nearly all the soot particles are oxidized as the soot field passes through the flame front; however, while medium and smaller particles are oxidized readily due to their larger surface-to-volume ratio, small concentrations of the largest particles appear to escape and travel downstream. Our model likely overestimates this effect, again due to its lack of inclusion of ageing phenomena; yet, even so, the predicted levels are likely undetectable as they are about 40 times lower than the peak volume fraction elsewhere in this lightly sooting flame.

Acknowledgments

This work has been supported in part by the Air Force Office of Scientific Research under contract F49620-94-C-0059. The encouragement of Julian Tishkoff is greatly appreciated.

References

1. Kaplan, C. R., Shaddix, C. R., and Smyth, K. C., Combustion and Flame, **106**, p. 392, (1996).
2. Kennedy, I. M., Rapp, D. R., Santoro, R. J., and Yam, C., Combustion and Flame, **107**, p. 386, (1996).
3. Smooke, M. D., McEnally, C. S., Pfefferle, L. D., Hall, R. J., and Colket, M. B., "Computational and Experimental Study of Soot Formation in a Coflow, Laminar Diffusion Flame," submitted to Combustion and Flame (1997).
4. Colket, M. B. and Hall, R. J.: in Soot Formation in Combustion, Mechanisms and Models, H. Bockhorn, Ed., Springer Series in Chemical Physics 59, Springer-Verlag, (1994).
5. Hall, R. J., Smooke, M. D., and Colket, M. B.: in Physical and Chemical Aspects of Combustion: A Tribute to Irvin Glassman, ed. by R. F. Sawyer and F. L. Dryer, Combustion and Science and Technology Book Series, Gordon and Breach, p. 189, 1997.
6. Dobbins, R. A., Govatzidakis, W. Lu, Schwartzman, A. F., and Fletcher, R. A., Combust. Sci. Tech. **121**, p. 103 (1996).

Figure 1. Super-Equilibrium OH in Methane Coflow Flame

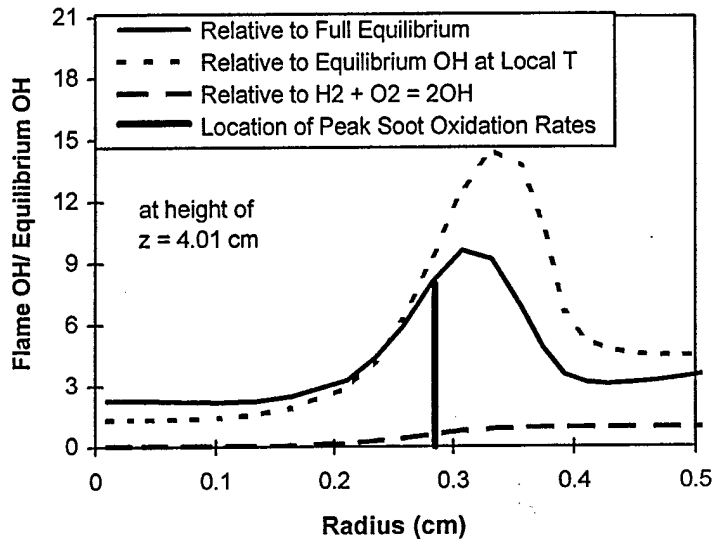

Figure 2. Radial Temperature Profiles and Peak Soot Growth

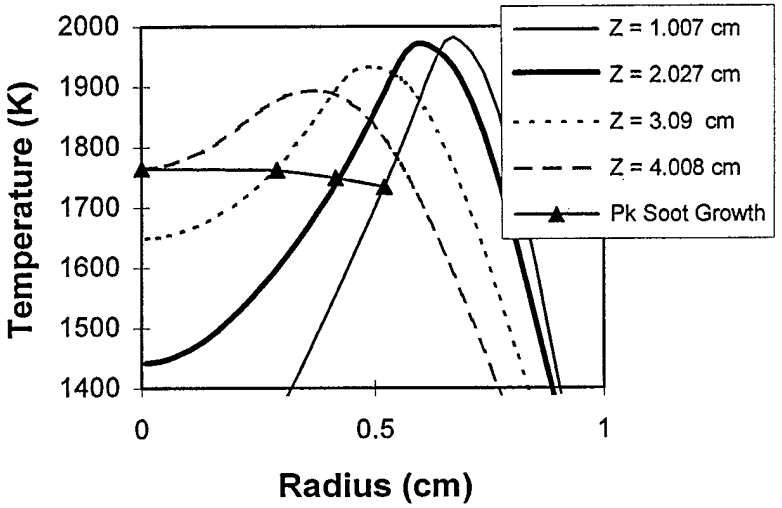

Figure 3. Variations of Local Phi in Coflow Flame

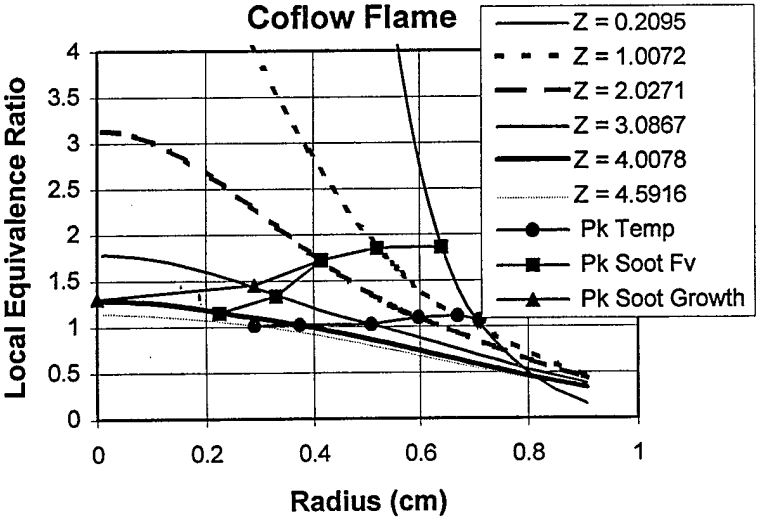

Figure 4. Variation of H/C Ratio in Coflow Flame

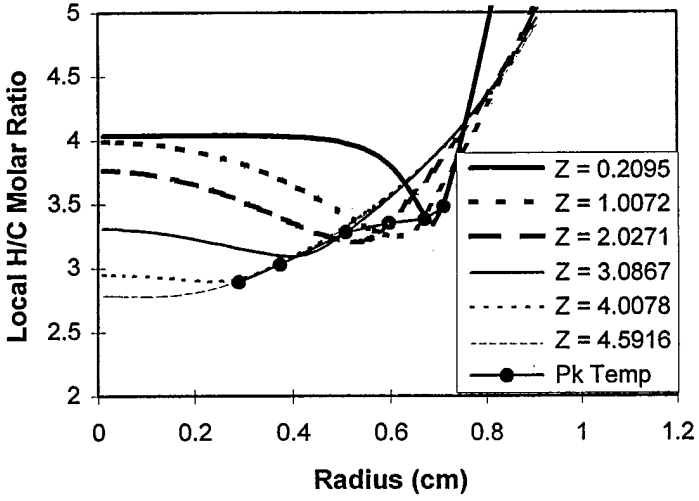

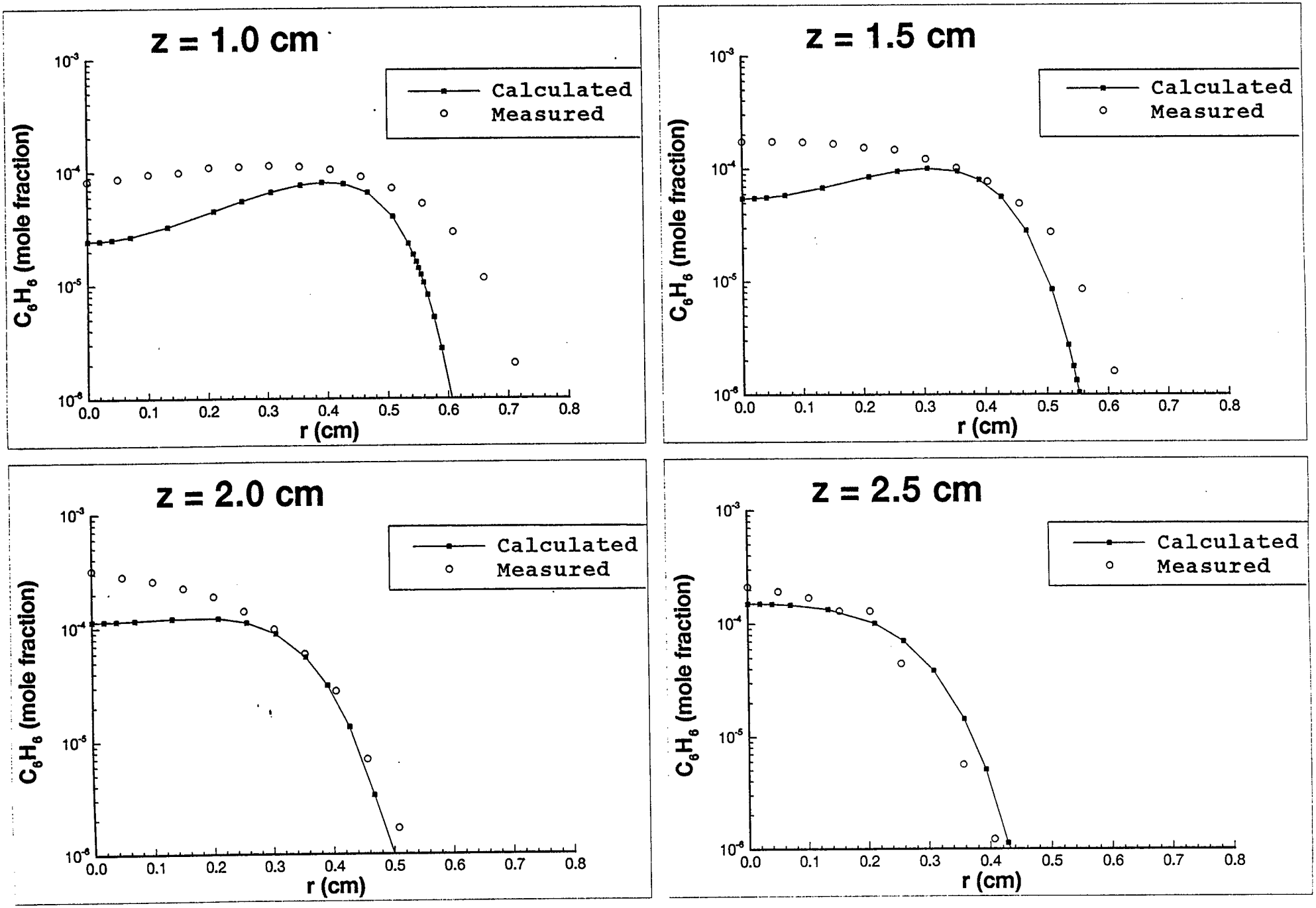
z = 1.0 cm
z = 1.5 cm
z = 2.0 cm
z = 2.5 cm
Calculated
Measured
C6H6 (mole fraction)
r (cm)
10-3
10-4
10-5
10-6
0.0
0.1
0.2
0.3
0.4
0.5
0.6
0.7
0.8

Figure 5

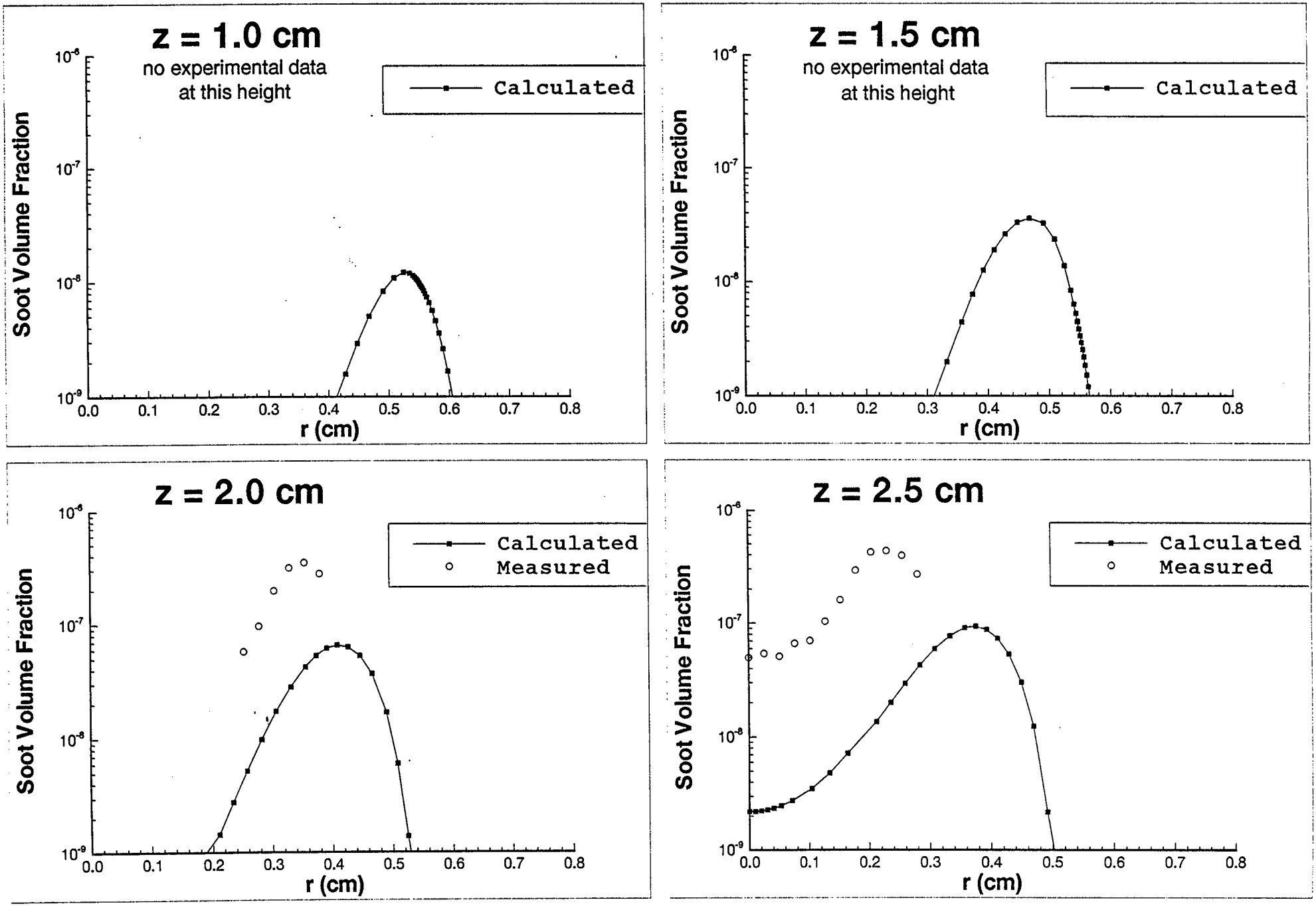
z = 1.0 cm
no experimental data
at this height
Calculated
Soot Volume Fraction
r (cm)
z = 1.5 cm
no experimental data
at this height
Calculated
Soot Volume Fraction
r (cm)
z = 2.0 cm
Calculated
Measured
Soot Volume Fraction
r (cm)
z = 2.5 cm
Calculated
Measured
Soot Volume Fraction
r (cm)

Figure 6